Utilizing Ultrafast Spectroscopy to Characterize Energy and Electron Transfer in Ru^{II} Based Molecular Assemblies Designed for Solar Fuel Devices

Stephanie Elaine Bettis

A dissertation submitted to the faculty of the University of North Carolina at Chapel Hill in partial fulfillment of the requirements for the degree of Doctor of Philosophy in the Department of Chemistry

Chapel Hill
2013

Approved by:

John Papanikolas

Cynthia Schauer

Marcey Waters

Andrew Moran

Michel Gagné

ABSTRACT

Stephanie Elaine Bettis: Utilizing Ultrafast Spectroscopy to Characterize Energy and Electron Transfer in Ru^{II} Based Molecular Assemblies Designed for Solar Fuel Devices (Under the direction of John M. Papanikolas)

This dissertation investigates the ultrafast dynamics in molecular assemblies for use in both dye-sensitized solar cells (DSSCs) and dye-sensitized photo electrosynthesis cells (DSPECs). A detailed kinetic analysis of the dynamics for the peptide and layered molecular assemblies provide insight into the orientation of the chromophores and catalysts substituents. The work was made possible from collaborations with both Dr. Marcey Waters' and Dr. Thomas Meyer's research groups, who provided the molecular assemblies for this study. Ultrafast spectroscopy techniques, such as transient absorption and time-resolved emission, were utilized for the kinetic study.

A brief introduction to solar cells and the molecular assemblies studied in the dissertation are described in Chapter 1. The following chapters discuss the ultrafast kinetics of the peptide and layered molecular assemblies. First, Chapter 2 discusses the use of tertiary structure to dictate the position of molecular substituents in a coiled-coil peptide system. Chapter 3 describes the incorporation of an oligoproline peptide chromophore assembly onto a nanocrystalline film for use in DSSCs. The oligoproline scaffold, in Chapter 4, is then used in a DSPEC set up functionalized with both a chromophore and a water oxidation catalyst. Last, the layered approach to a molecular assembly incorporating both a chromophore and

water oxidation catalyst on a nanocrystalline TiO_2 film is investigated in Chapter 5. Overall the work presented in this dissertation gains insight into the structure and orientation of the chromophores and catalysts in the peptide and layered molecular assembly scaffolds from detailed kinetic analyses.

To my family, friends, and loving husband Philip.

ACKNOWLEDGEMENTS

First, I wish to express my appreciation and gratitude to Dr. John Papanikolas for his infinite patience, advice, and wisdom. I cannot express how fortunate it has been to have an advisor who you respect not only as a scientist, but also as a person. Additional recognition and thanks is due to Dr. Kyle Brennaman for always having an open door and the willingness to discuss Ru(II) chemistry.

I'd also like to thank Papanikolas group members both past and present. In our group team work is critical and it has been great to work with all of you. Specifically I'd like to thank Dr. Brittany Westlake for teaching me the ropes of the laser and reminding me that most days it's not out get me. Dr. Ralph House also deserves many thanks for his positive outlook even on the gloomiest of days. I want to thank Dr. Brian Mehl who took the time to teach me not only how to code in MATLAB, but also to love and appreciate all it can do. I also appreciate Dr. Li Wang who shared in many conversations about chemistry from a synthetic perspective and life in general. I am also grateful for Dr. Erik Grumstrup who has been a huge resource for any optical problem that arises, especially when it means cracking open the laser. I'd also like to thank Melissa Gish who has fearlessly jumped in to continue the peptide projects and lead the "north" laser table.

It is also important to me that I thank my many collaborators, without their molecules I would not have had these projects. I want to thank Dr. Marcey Waters, Dr. Dale Wilger, Dr. Da Ma, and Dr. Derek Ryan for not only providing the various peptide samples, but also for

their insight into peptide kinetic dynamics. I also would like to thank Dr. Kenneth Hanson and Dr. Thomas Meyer who provided the layered samples along with many conversations about Ru(II) chemistry.

Finally, I'd like to thank my family and friends. I really appreciate the love and support they have all given me over the years. I am thankful for my parents, MaryJane and Sonny, and my siblings Emily, Kristina, Christopher, and Jonathan for their constant love and support all the way from Georgia. And last but not least I would like to thank my wonderful husband Philip Homan who has never stopped supporting me both as a scientist and a friend.

This research was supported solely by the UNC EFRC: Center for Solar Fuels, an Energy Frontier Research Center funded by the U.S. Department of Energy Office of Basic Energy Science under award DE-SC0001011.

TABLE OF CONTENTS

LIST OF TABLES

LIST OF SCHEMES

LIST OF FIGURES

LIST OF ABBREVIATIONS

bpy	2,2'-bipyridine
CaF_2	calcium fluoride
CMOS	complementary metal oxide semiconductor
CO_2	carbon dioxide
CPA	chirped pulse amplification
CuAAC	copper(I)-catalyzed azide-alkyne cycloaddition
DNA	deoxyribonucleic acid
DSPEC	dye-sensitized photo electrosynthesis cell
DSSC	dye-sensitized solar cell
e^-	electron
FWHM	full width half maximum
Gnd HCl	guanidinium chloride
H^+	proton
H_2O	water
$HClO_4$	perchloric acid
IR	infrared
L	4´-methyl-(2,2´-bipyridine)-4-propargyl amide
L1	4´-methyl-(2,2´-bipyridine)-4-propargyl amide
L2	4´-methyl-(2,2´-bipyridine)-4-dimethyl-ether
ln	natural logarithm
log	logarithm

Mebimpy	2,6-bis(1-methylbenzimidazol-2-yl)pyridine
MeOH	methanol
^{1}MLCT	singlet metal to ligand charge transfer
^{3}MLCT	triplet metal to ligand charge transfer
MOF	metal organic framework
O_2	oxygen gas
OD	optical density
OEC	oxygen evolving complex
OPA	optical parametric amplifier
Os(II)	osmium (II)
$[Os_0]$	initial Os concentration
pbpy	4,4´-$(PO_3H_2)_2$-2,2´-bipyridine
pdb	protein data base
pH	logarithm of the reciprocal of hydrogen ion concentration
phen	phenanthroline
pK_A	logarithmic acid dissociation constant
PP II	polyproline II
PS II	photosystem II
Ru(II)	ruthenium (II)
$[Ru_0]$	initial Ru concentration
[RuOs]	initial Ru/Os peptide concentration
SPPS	solid-phase peptide synthesis
SSE	steady-state emission

SVD	singular value decomposition
TCSPC	time-correlated single photon counting
TiO_2	titanium dioxide
UV-Vis-NIR	ultraviolet-visible-near infrared
Zr^{4+}	zirconium ions
ZrO_2	zirconium dioxide

LIST OF SYMBOLS

$\approx$	approximately
A	absorbance
ΔA	change in absorbance
$<\tau>$	average lifetime
°C	degrees Celsius
^3dd	triplet d-d excited state
E_0	energy gap
ε	molar absorptivity
ν	frequency
ΔG	Gibb's free energy
$\hbar\omega$	quantum spacing frequency mode
I(t)	initial concentration at time t
Φ_{inj}	injection efficiency
k	rate constant
K_a	association equilibrium constant
k_b	Boltzman's constant
k_{EnT}	energy transfer rate constant

k_{Ru}	Ru excited-state rate constant
π-π	pi to pi ligand stacking
ππ*	pi to pi* electronic transition
S	electron-vibrational coupling constant
Γ	surface loading
t	time
T	temperature
τ	lifetime
τ_{EnT}	energy transfer lifetime
$\Delta\bar{\nu}_{0,1/2}$	the full width half-maximum of the 0-0 vibronic component
λ	wavelength
λ_{max}	maximum wavelength

CHAPTER 1. INTRODUCTION

1.1. OVERVIEW

The harvesting of energy from the sun offers a promising strategy as an alternative energy resource.[1-2] The dye-sensitized solar cell (DSSC), or Grätzel cell, is part of the first generation of solar cell devices that utilize light-harvesting chromophores on nanocrystalline semiconductors to generate a charge separation and thus electricity upon photoactivation.[3] DSSCs, however, do not provide a solution to energy storage during times of low solar flux. As a result, recent efforts have been made to design an artificial photosynthetic device that will store the energy in the form of solar fuels such as methane or ethanol. The DSPEC, or dye-sensitized photoelectrosynthesis cell, uses sunlight to drive the oxidation of water and the reduction of protons or carbon dioxide to chemical fuels. [4] Overall, DSPEC devices integrate molecular components that can harvest light, separate the redox equivalents, and drive catalytic water oxidation.

Water oxidation requires the sequential transfer of four electrons and four protons in the net reaction $2H_2O \rightarrow O_2 + 4H^+$.[1] A general strategy to achieve the multi-functional system couples molecular catalysts with the charge separation capability of surface-bound dyes, such as those found in DSSCs, which provide the oxidative equivalents needed to drive the water oxidation cycle. Essential to the efficiency of the DSPEC is the placement of the light-absorbing chromophore and catalyst in close proximity to facilitate charge separation and activation of the catalyst. Thus, a molecular architecture arranging the light-harvesting chromophore and water oxidation catalyst effectively is central to the function of the DSPEC.

A variety of scaffold strategies have been explored for both DSSCs and DSPECs, including polymers,[5-8] dendrimers,[9-10] metal organic frameworks (MOFs),[11-12] molecular assemblies,[13-16] porphyrins,[17-18] peptides,[19-22] and layered approaches.[23] Architectures such as

polymers, dendrimers and MOFs are easily made, but due to the nature of their syntheses, are not monodisperse in structure. Direct synthetic strategies, such as porphyrins and molecular assemblies, offer control over chromophore and catalyst placement, but are difficult to synthesize and not modular in design. Therefore, a scaffold architecture that is both easily synthesized and controls the placement of the molecular substituents is needed.

The two strategies explored within this dissertation are peptide and layered scaffolds. These approaches offer a solution for scaffolds that are both easily synthesized and provide the ability to control chromophore-catalyst placement. The first scaffolds studied are peptides. The studies included here specifically focus on coiled-coils and oligoprolines. Peptide scaffolds are advantageous because they offer control over the placement of the chromophores and catalysts. For example, chromophore placement can be controlled on two levels by both its primary sequence and resulting higher order structure. The primary sequence of a peptide uses weak forces, such as hydrogen bonding and ionic interactions, to dictate the secondary and tertiary structures arranging the chromophores and catalysts. Both peptide systems discussed in this dissertation fold in to a helical structure based on the primary sequence and solvent. The second scaffold architecture discussed is the layered or "layer-by-layer" approach. This strategy simplifies molecular placement by eliminating the need to synthesize a base scaffold. Instead, the "layer-by-layer" approach utilizes coordination chemistry to arrange the chromophores and catalysts on a nanocrystalline film. However, due to the random nature of the "layer-by-layer" structure the exact orientation of the chromophores cannot be controlled.

The focus of this dissertation is the investigation of the kinetics within the peptide and layered scaffolds, which provides insight into the efficiency of their structures for use in

DSSCs and DSPECs. There are a variety of kinetic processes that occur in both the chromophore-chromophore systems and chromophore-catalyst systems. Specifically, upon photoexcitation surface bound chromophores inject electrons into the conduction band of the nanocrystalline TiO_2 film, which is often followed by electron transfer. Once photoexcited, energy transfer between the chromophores and catalysts species is also possible. Lastly charge recombination or back electron transfer from the TiO_2 to the oxidized chromophore or catalyst can occur. These kinetic processes occur with time constants spanning several orders of magnitude ranging from femtoseconds to milliseconds. As a result a variety of photophysical techniques are needed to investigate these processes. Specifically, in this dissertation ultrafast transient absorption, picosecond transient absorption, and time-correlated single photon counting (TCSPC) are used to investigate the scaffolds.

The remainder of this dissertation is divided into four chapters. **Chapter 2** discusses the use of time-resolved emission spectroscopy to measure position-dependent energy transfer that occurs through changes in the sequence of the coiled-coil peptide scaffold. Through the tertiary structure, the coiled-coil supramolecular peptide scaffold controls the functional properties of the Ru(II) and Os(II) assembly.

Chapter 3 discusses the photophysical analysis of oligoproline peptide scaffold containing two Ru(II) complexes, where one Ru(II) complex is bound to nanocrystalline TiO_2. Ultrafast transient absorption and time-resolved emission techniques were used to observe remote injection into TiO_2 due to energy transfer from the outer chromophore to the inner bound chromophore, followed by electron injection into TiO_2.

Chapter 4 reports the use of ultrafast transient absorption spectroscopy to analyze the first photoactivation step for oxidation of water in a chromophore-catalyst proline assembly.

A global kinetic analysis of the transient absorption spectra reveal photoinduced electron injection on the timescale of 18 ps, with subsequent transfer of the oxidative equivalent to the water oxidation catalyst on the hundred of picoseconds timescale.

Chapter 5 discusses the photophysical analysis of a "layer-by-layer" chromophore-catalyst assembly. Again ultrafast transient absorption spectroscopy is used to determine the kinetics of the first photoactivation step for water oxidation. The global analysis results in photoinduced picosecond electron transfer followed by transfer of the oxidative equivalent to the catalyst on the hundreds of picosecond timescale.

The kinetic analyses of the peptide and layered scaffolds revealed that the peptide is a better scaffold overall for use in DSPECs. While the peptide scaffold has a slower rate for transfer of the oxidative equivalent (380 ps) than the layered approach (170 ps), it has a better overall efficiency. The lower efficiency of the layered approach is a result of nonproductive absorption caused by a greater amount of catalysts than chromophores on the surface. The peptide system on the other hand provides control of the chromophore and catalyst placement ensuring a one to one ratio and an overall higher efficiency. Further optimization of the peptide scaffold can be achieved by placing the chromophore and catalyst closer together resulting in a faster transfer rate and even higher overall efficiency.

REFERENCES

(1) Alstrum-Acevedo, J. H.; Brennaman, M. K.; Meyer, T. J. *Inorg. Chem.* 2005, *44*, 6802-6827.

(2) Lewis, N. S.; Nocera, D. G. *Proceedings of the National Academy of Sciences* 2006, *103*, 15729-15735.

(3) O'Regan, B.; Grätzel, M. *Nature* 1991, *353*, 737-740.

(4) Song, W.; Chen, Z.; Brennaman, M. K.; Concepcion, J. J.; Patrocinio, A. O. T.; Murakami Iha, N. Y.; Meyer, T. J. *Pure Appl. Chem.* 2011, 83, 749-768.

(5) Fang, Z.; Eshbaugh, A. A.; Schanze, K. S. *J. Am. Chem. Soc.* 2011, *133*, 3063-3069.

(6) Liu, Y.; Summers, M. A.; Edder, C.; Fréchet, J. M. J.; McGehee, M. D. *Adv. Mater.* 2005, *17*, 2960-2964.

(7) Kim, Y.-G.; Walker, J.; Samuelson, L. A.; Kumar, J. *Nano Lett.* 2003, *3*, 523-525.

(8) Wang, L.; Puodziukynaite, E.; Vary, R. P.; Grumstrup, E. M.; Walczak, R. M.; Zolotarskaya, O. Y.; Schanze, K. S.; Reynolds, J. R.; Papanikolas, J. M. *J. Phys. Chem. Lett.* 2012, *3*, 2453-2457.

(9) Gilat, S. L.; Adronov, A.; Fréchet, J. M. J. *Angew. Chem. Int. Ed.* 1999, *38*, 1422-1427.

(10) Hasobe, T.; Kashiwagi, Y.; Absalom, M. A.; Sly, J.; Hosomizu, K.; Crossley, M. J.; Imahori, H.; Kamat, P. V.; Fukuzumi, S. *Adv. Mater.* 2004, *16*, 975-979.

(11) Lee, C. Y.; Farha, O. K.; Hong, B. J.; Sarjeant, A. A.; Nguyen, S. T.; Hupp, J. T. *J. Am. Chem. Soc.* 2011, *133*, 15858-15861.

(12) Kent, C. A.; Liu, D.; Ma, L.; Papanikolas, J. M.; Meyer, T. J.; Lin, W. *J. Am. Chem. Soc.* 2011, *133*, 12940-12943.

(13) Hu, K.; Robson, K. C. D.; Johansson, P. G.; Berlinguette, C. P.; Meyer, G. J. *J Am. Chem. Soc.* 2012, *134*, 8352-8355.

(14) Huang, Z.; Geletii, Y. V.; Musaev, D. G.; Hill, C. L.; Lian, T. *Ind. Eng. Chem. Res.* 2012, 51, 11850-11859.

(15) Norris, M. R.; Concepcion, J. J.; Harrison, D. P.; Binstead, R. A.; Ashford, D. L.; Fang, Z.; Templeton, J. L.; Meyer, T. J. *J. Am. Chem. Soc.* 2013, *135*, 2080-2083.

(16) Ashford, D. L.; Song, W.; Concepcion, J. J.; Glasson, C. R. K.; Brennaman, M. K.; Norris, M. R.; Fang, Z.; Templeton, J. L.; Meyer, T. J. *J. Am. Chem. Soc.* 2012, *134*, 19189-19198.

(17) Mozer, A. J.; Griffith, M. J.; Tsekouras, G.; Wagner, P.; Wallace, G. G.; Mori, S.; Sunahara, K.; Miyashita, M.; Earles, J. C.; Gordon, K. C.; Du, L.; Katoh, R.; Furube, A.; Officer, D. L. *J. Am. Chem. Soc.* 2009, *131*, 15621-15623.

(18) Uetomo, A.; Kozaki, M.; Suzuki, S.; Yamanaka, K.; Ito, O.; Okada, K. *J. Am. Chem. Soc.* 2011, *133*, 13276-13279.

(19) Wilger, D. J.; Bettis, S. E.; Materese, C. K.; Minakova, M.; Papoian, G. A.; Papanikolas, J. M.; Waters, M. L. *Inorganic Chemistry*. 2012, 51, 11324-11338.

(20) Ma, D.; Bettis, S. E.; Hanson, K.; Minakova, M.; Alibabaei, L.; Fondrie, W.; Ryan, D. M.; Papoian, G. A.; Meyer, T. J.; Waters, M. L.; Papanikolas, J. M. *J. Am. Chem. Soc.* 2013, *135*, 5250-5253.

(21) Hong, J.; Kharenko, O. A.; Ogawa, M. Y. *Inorg. Chem.* 2006, *45*, 9974-9984.

(22) Mecklenburg, S. L.; Peek, B. M.; Schoonover, J. R.; McCafferty, D. G.; Wall, C. G.; Erickson, B. W.; Meyer, T. J. *J. Am. Chem. Soc.* 1993, *115*, 5479-5495

(23) Hanson, K.; Torelli, D. A.; Vannucci, A. K.; Brennaman, M. K.; Luo, H.; Alibabaei, L.; Song, W.; Ashford, D. L.; Norris, M. R.; Glasson, C. R. K.; Concepcion, J. J.; Meyer, T. J. *Angew. Chem. Int. Ed.* 2012, *51*, 12782-12785.

CHAPTER 2. TUNABLE ENERGY TRANSFER RATES VIA CONTROL OF PRIMARY, SECONDARY, AND TERTIARY STRUCTURE OF A COILED COIL PEPTIDE SCAFFOLD[1]

[1]This chapter previously appeared as an article in the Inorganic Chemistry. The original citation is as follows: Wilger, D. J.; Bettis, S. E.; Materese, C. K.; Minakova, M.; Papoian, G. A.; Papanikolas, J. M.; Waters, M. L. *Inorganic Chemistry*. 2012, 51 (21), 11324-11338.

2.1. INTRODUCTION

The design of molecular materials capable of performing complex functions is pivotal to "bottom-up" approaches in molecular electronics,[1] sensing[1a,2] and solar energy conversion.[3,4] The most common strategy for building artificial assemblies uses covalent bond formation to connect molecular components with rigid linkers that dictate both distance and orientation. While this approach provides exquisite control over spatial parameters,[5] the optimization of functional performance often requires the development of new synthetic routes making the implementation very difficult, especially as the number of molecular components increases. Alternatively, chromophores have been placed on easily synthesized scaffolds such as polymers,[6] dendrimers,[1a,3c,7] and organogels[8]. However this approach can yield assemblies that are not monodisperse in molecular weight or chemical composition and incorporate many different morphological constituents. While large systems are readily made and some control over the primary structure is possible, the flexible scaffolds result in solution structures that vary from one assembly to the next.

Another approach to achieve functional architectures draws inspiration from natural systems, which combine simple molecular building-blocks to form highly complex systems. Nature exploits relatively weak noncovalent interactions to achieve functional architectures with a hierarchical control. In these natural systems, sequence defines structure and self-assembly, which defines function. Proteins, lipids, and oligonucleotides form the structural framework that organize elements in spatial proximity and with well-defined orientations.[9] To this end, functionalized biological molecules such as oligonucleotides[10], amyloid-like peptide fibrils[11], and even derivatized virus coated proteins have been designed and investigated as functional materials.[12] These types of artificial systems[11,13-15] that mimic the

organizational strategies of biomolecules provide a number of advantages, including design flexibility, ease of synthesis, and spatial control of functionality through supramolecular architectures that allow for fine-tuning of materials properties.

The design of an artificial polypeptide system based on a heterodimeric coiled-coil architecture includes a primary sequence that defines both the secondary and tertiary structure, resulting in self-assembly. This provides fine control of the positioning of octahedral tris(bipyridyl) transition metal complexes $[M^{II}(bpy)_3]^{2+}$ (M = Ru or Os, bpy = 2,2'-bipyridyl). Coiled-coils are a common protein motif and provide structural architecture for many important protein scaffolds including α-keratin[16] and tropomyosin.[17] Moreover, the sequence-structure rules are well defined, allowing for the design of highly tunable supramolecular architectures by control of the primary sequence.[18a] In this study, the peptide secondary structure controls self-assembly and relative positioning of the octahedral complexes, resulting in systematic tuning of the energy transfer properties of the system. The Ru(II) and Os(II) metal complexes are positioned near the midpoints of two complementary peptide chains, each consisting of 28 residues (Figure 2.1). The primary sequence of each chain is chosen such that they adopt a dimeric supramolecular structure consisting of two α -helical coils, where the hydrophobic residues are shielded from the aqueous environment and the hydrogen bonding and ionic interactions are maximized. Since the metal complexes are placed on different peptide chains, energy transfer is only possible if the two chains associate in solution, making this system particularly sensitive to the secondary and tertiary structure of the peptide scaffold. Therefore, photoexcitation of the Ru(II) complex in the folded assembly results in energy transfer to the lower energy Os(II) acceptor on the opposing chain.

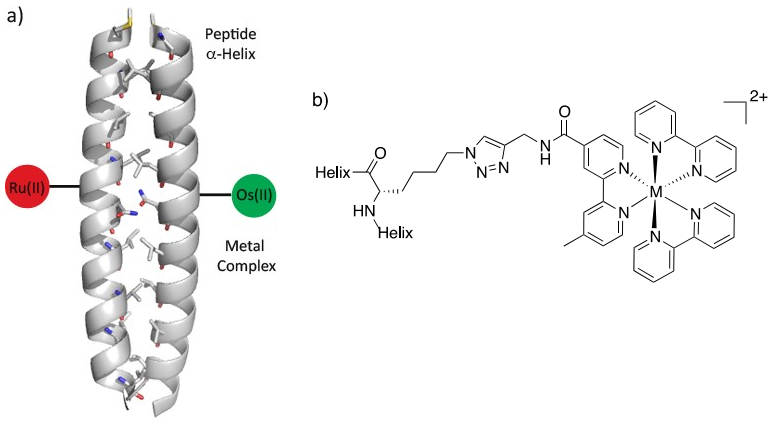

Figure 2.1. (A) Illustration of metallopeptide system containing the α-helical coiled-coil scaffold and metal complexes (coiled coil: pdb 2AHP). (B) Structure of the metal complex and its attachment to the α-helix.

The peptide structures studied here take advantage of two flexible synthetic methodologies: solid-phase peptide synthesis (SPPS) and the copper(I)-catalyzed azide-alkyne cycloaddition (CuAAC or "click reaction"). SPPS is advantageous as it allows for exact positioning of the chromophores in the primary sequence. The use of click chemistry as an orthogonal linkage strategy between the chromophores and peptides has several advantages. First, it avoids issues with formation of statistical mixtures of species, as was obtained in the electron transfer coiled-coil systems developed by Ogawa, in which the chromophore linkage was accomplished via non-specific coordination chemistry.[15] Secondly, click chemistry provides advantages over the direct amide linkage used in the electron-transfer oligoproline systems reported by Meyer, in which orthogonal protecting group strategies had to be employed.[14]

The series of peptide assemblies examined systematically vary the placement of the complexes along the peptide backbone results in predictable changes in the energy transfer rate, which are measured using time-resolved emission methods. Variation in the rate by

almost an order of magnitude across the series, as well as denaturation studies, confirm that energy transfer is the direct result of folding into a well-defined tertiary structure. All-atom molecular dynamics simulations provide insight into the microscopic environment, revealing an assembly with a dynamic, yet robust, tertiary structure that effectively controls the relative positioning of the two complexes.

The work described in this chapter was published in *Inorganic Chemistry* (Wilger, D.; Bettis, S.E., et al. *Inorg. Chem*. 2012, 51 (21), 11324-11338). The paper was a result of close collaboration between three research groups lead by Dr. Marcey Waters, Dr. John Papanikolas and Dr. Garegin A. Papoian. The contribution I made included the photophysical analysis of the peptides and is described in detail in this chapter. The work of my collaborators is summarized in this chapter, and described in detail in our published paper.

2.2. EXPERIMENTAL

2.2.1. Steady-state Techniques

Ground state absorbance measurements were conducted with a Hewlett Packard 8453 UV-VIS-NIR absorption spectrophotometer. Steady state emission (SSE) data were collected using an Edinburgh Instruments FLS920 equipped with a 450 W Xenon lamp and photomultiplier tube (Hamamatsu 2658P). SSE data were collected using a bandwidth no larger than 4.0 nm and, once collected, were corrected for the emission spectrophotometer's spectral response.

2.2.2. Time-Correlated Single Photon Counting

The FLS920 was also used for time-resolved measurements by the time-correlated single photon counting (TCSPC) technique with an instrument response of 2 ns, using a

444.2 nm diode laser (Edinburgh Instruments EPL- 445, 73 ps FWHM pulse width) operated at 200 kHz. A 495 nm long pass color filter was used for emission experiments. The samples were placed in a 2.0 mm cuvette and placed at 45 degree angle from the incident laser beam. Samples were purged in Argon for >25 minutes just prior to emission experiments. All experiments were performed with $Abs_{444\ nm}$< 0.2 OD. The solvent for each sample was 10 mM phosphate buffer at pH 7.

2.3. RESULTS AND DISCUSSION

2.3.1. Peptide Design and Structural Characterization

The coiled-coil peptide design, synthesis, and structural characterization of the peptide coiled-coils were performed by Dr. Dale Wilger in Dr. Waters' research group, and are described in detail in the publication of this work. Briefly, the coiled-coil peptide scaffold consists of 28-residue peptides that contain the canonical repeating heptad sequence (designated *abcdefg*) typical of most coiled-coil peptides. The formation of parallel heterodimeric coiled-coils is obtained through hydrophobic interactions (*a* and d sites), hydrogen bonding between asparagine (single *a* site), and the complementary ionic interactions between the two peptides (*e* and *g* sites), Figure 2.2A.[18a,19-21] Monomeric peptide formation is not present in this system due to the large hydrophobic patch, which is unfavorable in aqueous solution. The helical wheel diagram of the coiled-coil shows the relative orientation of the various amino acids in the primary sequence (Figure 2.2B).

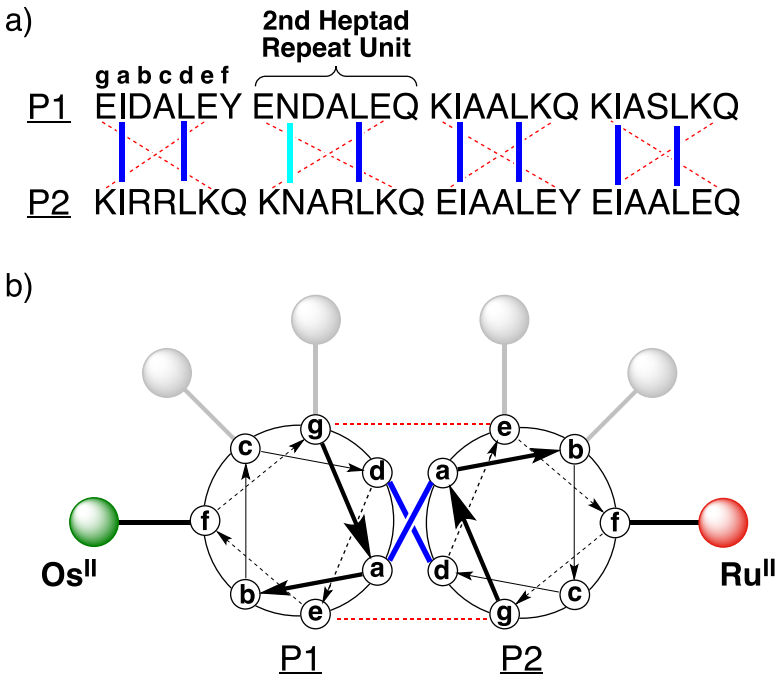

Figure 2.2. (A) Primary sequences of the P1 and P2 peptides using the single letter amino acid code (in capitals). Each 28-residue peptide has four heptad repeat units. The common letter designations for the heptad positions (*abcdefg*) are shown above the first heptad repeat unit for P1. The hydrophobic interactions are shown as blue lines, the hydrogen bonding interaction between Asn sidechains is shown as a cyan line, and the complementary ionic interactions between the two peptides are shown as red dashed lines. (B) A helical-wheel diagram displaying the potential points for attachment when viewed down helix axis from the N-terminus. The P1 peptide is modified with Os(II) at the *f*, *c*, or *g* position within the second heptad. The P2 peptide is modified with Ru(II) at the *f*, *b*, or *c* position within the second heptad.

Three specific pairs of metallopeptides were selected for structural analysis, photophysical characterization, and all-atom molecular dynamics simulation. The 2*f*-Os/2*f*-Ru metallopeptide pair refers to the heterodimer formed by the 2*f*-Os-P1 and 2*f*-Ru-P2 metallopeptides and was expected to provide the largest donor/acceptor separation distance, based on the analysis of parallel dimeric coiled-coils with crystal structures reported in the

protein data base (PDB code: 3NM6, 1UIX, and 3M9B). Based on measurement from the α-carbons, the distance between aligned *f* positions typically ranged from 14.0-14.9 Å. Similar analysis indicated that *b*-*c* separations were 12.7-13.5 Å, and *e*-*g* separations were 9.6-10.3 Å. Although these measurements do not account for the length or flexibility of the azidolysine linker, they qualitatively represent the general trends that may be expected for the rates of energy transfer in the 2*f*-Os/2*f*-Ru, 2*c*-Os/2*b*-Ru, and 2*g*-Os/2*e*-Ru metallopeptide pairs.

The structure of the three peptide systems was characterized with the use of circular dichroism and thermodynamic stability. These studies indicate that all three heterodimeric metallopeptide pairs form coiled-coil structures when mixed in a 1:1 ratio in aqueous buffer at μM concentrations.[22]

2.3.2. Stead-state Spectroscopy

The ground state absorption spectrum for the 2*g*-Os/2*e*-Ru metallopeptide pair exhibits a peak at 450 nm and a lower energy band that is centered at 650 nm (Figure 3). The peak centered at 450 nm is the singlet metal-to-ligand charge transfer (^{1}MLCT) for both the Ru(II) and Os(II) bipyridyl complexes, while the lower energy band corresponds to direct excitation of the ^{3}MLCT in the Os(II) complex which is optically accessible because of large spin-orbit coupling. When excited at 450 nm, the steady-state emission spectrum for the 2*g*-Os/2*e*-Ru peptide exhibits a higher energy band (λ_{max} at 660 nm) that corresponds to Ru(II) ^{3}MLCT emission after fast intersystem crossing from the ^{1}MLCT, while the peak centered at 800 nm is Os(II) ^{3}MLCT emission (Figure 2.3). The steady-state emission spectra show an increase in the Os(II) emission as the chromophores are moved closer to each other, providing direct evidence for Ru(II) to Os(II) energy transfer (Figure 2.4).

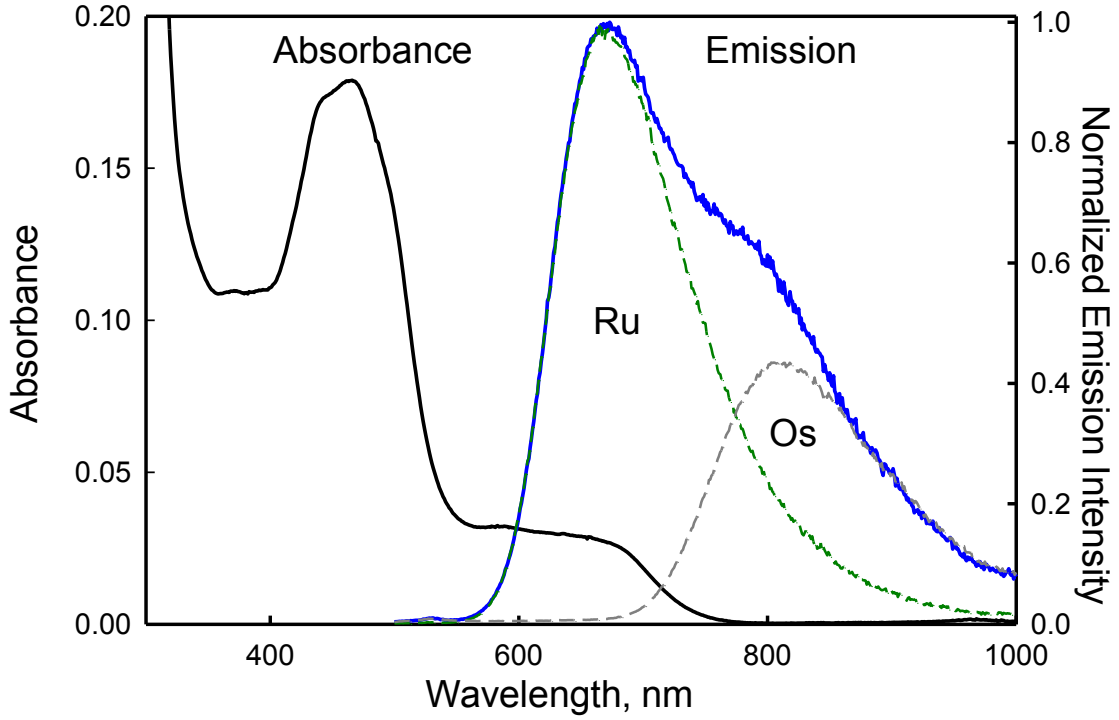

Figure 2.3. The ground-state absorption (black:25 μM 2e-Ru and 50 μM 2g-Os) and steady state emission (blue: 25 μM 2e-Ru and 50 μM 2g-Os) spectra of the 2g-Os/2e-Ru peptide coiled-coil in a 10 mM sodium phosphate buffer solution, pH 7, 25°C. Also shown are the 2*e*-Ru(II) peptide (green dashed: 25 μM 2*e*-Ru) and 2*g*-Os(II) peptide emission spectra (grey dashed: 100 μM 2g-Os). The excitation wavelength was 450 nm.

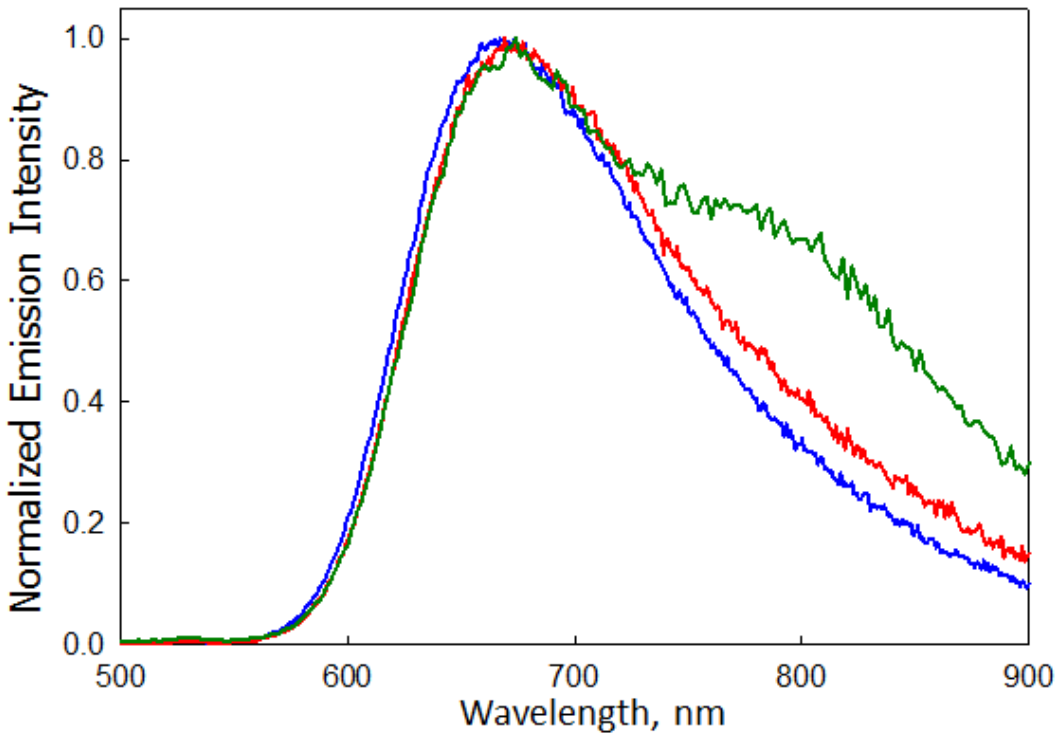

Figure 2.4. Steady-state spectra of the three peptide coiled-coil systems (blue: 25 mM 2f-Ru and 50 mM 2f-Os, red: 25 mM 2b-Ru and 50 mM 2c-Os, and green: 25 mM 2e-Ru and 50 mM 2e-Os) in a 10 mM sodium phosphate buffer solution, pH 7, 25°C. The excitation wavelength was 450 nm.

2.3.3. Time-resolved Spectroscopy

Photoexcitation of the Ru(II) center at 450 nm is followed by rapid relaxation into the ^{3}MLCT band, and potentially triplet-triplet energy transfer to the lower energy Os(II) site. In principle, energy transfer can be observed either through the quenching of Ru(II) emission at 660 nm or the appearance of the Os(II) emission at 800 nm. In practice, however, the Os(II) emission due to energy transfer is obscured by Ru(II) emission in the low energy tail and phosphorescence arising from the direct excitation of Os(II) at 450 nm. Both these contributions make a quantitative analysis of the Os(II) emission difficult. While Ru(II)

emission contaminates the emission of Os(II) at 800 nm, the converse is not true, and both the time-resolved and steady-state emission measurements show no detectable Os(II) emission at 660 nm. Thus, Ru(II) emission provides the cleanest window through which to view Ru-to-Os energy transfer.

The 2*e*-Ru/P1 coiled-coil was used as a control to measure the Ru lifetime in the absence of energy transfer (Figure 2.5A). The decay is single exponential with a lifetime around 450 ns (2.2×10^6 s^{-1}), comparable to the lifetime of $Ru(bpy)_3^{2+}$ in water.[23] Pairing of 2*e*-Ru with the 2*g*-Os peptide instead of the unmodified P1 results in quenched Ru(II) emission due to energy transfer (Figure 2.5A). The decay is biexponential with a fast component of 42 ns that is related to energy transfer and a slow component that matches the Ru(II) lifetime of 450 ns. The slow component is attributed to a small fraction of unassociated Ru(II) chains in solution that are present as a result of the ground state equilibrium between the peptide chains.

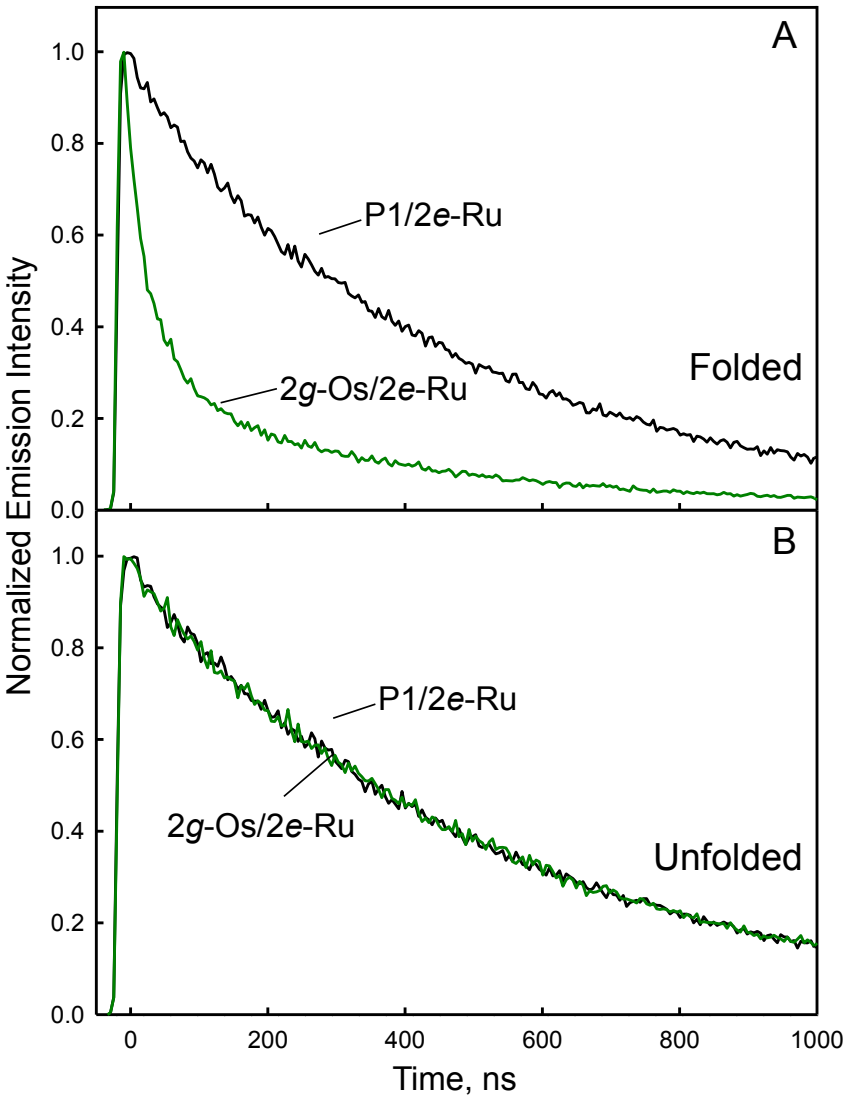

Figure 2.5. (A) Time-resolved emission of 2*e*-Ru peptide in the presence of the P1 peptide (black: 25 μM 2*e*-Ru and 50 μM P1) and the 2*g*-Os peptide (green: 25 μM 2*e*-Ru and 50 μM 2g-Os) in a 10 mM sodium phosphate buffer solution at pH 7 and 25°C. (B) P1/2*e*-Ru peptide with chemical denaturant (black: 25 μM 2*e*-Ru, 50 μM P1 and 5 M guanidinium chloride, 20 mM sodium phosphate, and 100 mM sodium chloride buffer at pH 7 and 25°C) and 2*g*-Os/2*e*-Ru peptide pair with chemical denaturant (green: 25 μM 2*e*-Ru, 50 μM 2g-Os, and 5 M guanidinium chloride 20 mM sodium phosphate and 100 mM sodium chloride buffer at pH 7 and 25°C). Ru(II) emission quenching by energy transfer is turned off in the presence of the chemical denaturant. The time-resolved emission data were collected at 660 nm with an excitation of 444 nm.

2.3.4. Influence of Folding on Energy Transfer

A comparison of the energy transfer dynamics in the folded and unfolded state can be achieved through denaturation of the peptide scaffold, which, in principle, can be accomplished by either heating or incorporating chemical additives. Temperature induced denaturation is more problematic because of the high thermal stability of the coiled-coil peptides. The analysis would be further complicated by the fact that the Ru(II) ^{3}MLCT excited state lifetime is diminished with increasing temperature due to the thermally accessible metal-centered (^{3}dd) excited states that undergo rapid nonradiative decay. Chemical denaturation with GndHCl provides a viable alternative method for studying the denatured state at the same concentration used for time-resolved experiments.

The 660 nm decays for the P1/2*e*-Ru and 2*g*-Os/2*e*-Ru systems in the presence of guanidine denaturant were measured and compared to the nondenatured complex (Figure 2.5B). The excited state lifetime of the 2*e*-Ru peptide is slightly longer in the highly polar 5 M GndHCl denaturation medium (τ = 520 ns compared to 450 ns in buffer), but is unaffected by the presence of up to two equivalents (50 mM) of the 2*g*-Os peptide. The ability of the chemical denaturant to turn off energy transfer confirms that the Ru(II) emission quenching arises from the folded coiled-coil peptide structure, not from non-specific interactions between the peptide chains.

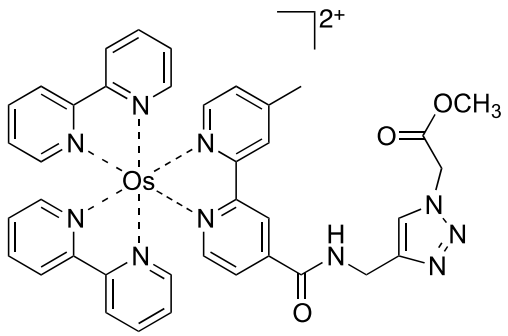

Figure 2.6. The Os(II) complex (1) was used as a diagnostic for intermolecular energy transfer not mediated by the peptide scaffold.

In addition, an Os(II) "control complex" (**1**, Figure 2.6) was designed to mimic the acceptor module, while lacking any molecular recognition elements that would allow for association with the partner peptide. When the control complex (**1)** was mixed with the 2*b*-Ru peptide, no change in the excited-state lifetime was observed with up to 2 equivalents present. This differs from similar studies of Ru(II) and Os(II) modified oligonucleotides, which show that the addition of a noncovalently attached Os(II) complex ($[Os(bpy)_2(phen)]^{2+}$) to a Ru(II)-containing oligonucleotide solution results in some quenching (~8 %) of the Ru(II) based phosphorescence, even at much lower Os(II) concentrations.[10c] This observation could be a consequence of the difference in the net charge on the two scaffolds or intercalation.[10e] The oligonucleotides used in that work are polyanionic molecules, and may have attractive charge-charge interactions with bipyridyl complexes that result in aggregation in solution. The 2*b*-Ru peptide on the other hand contains a net positive (+5) charge at pH 7, resulting in a repulsive charge-charge interactions with the control complex. In addition, weak intercalation of the bpy ligands into the DNA duplex may be responsible for the observed quenching in the DNA system, which is not possible in this peptide scaffold.[10e]

The results of the two control experiments clearly demonstrate that energy transfer within the peptide system occurs between coiled-coil dimer partners, and requires the folded self-assembled peptide scaffold for structural organization.

2.3.5. Positional Variation and Energy Transfer

The Ru(II) emission quenching for the three coiled-coil metallopeptide pairs: 2f-Os/2f-Ru, 2c-Os/2b-Ru, and 2g-Os/2e-Ru (Figure 2.7) was compared along with the transients from three coiled-coils containing the Ru(II) metallopeptides paired to the P1 peptide. All three of the P1/Ru(II) systems exhibit qualitatively similar monoexponential decay kinetics (Table 2.1). Each transient in the mixed Ru(II)/Os(II) systems is biexponential, where the slow component arises from the free Ru chains in solution and the fast component reflects Ru quenching due to energy transfer. The peptide pair that places the complexes the farthest apart, 2*f*-Os/2*f*-Ru (Figure 2.7 blue line), has the largest distance between alpha carbons (14.0-14.9 Å), and results in the slowest energy transfer, k_{EnT} = 816 ns. The 2*g*-Os/2*e*-Ru peptide pair (Figure 2.7, green line) places the complexes the closest to each other with an α-carbon distance of 9.6-10.3 Å, and has the fastest energy transfer, k_{EnT} = 42 ns. Lastly, the 2*c*-Os/2*b*-Ru peptide pair has an intermediate spacing (12.7-13.5 Å) and its energy transfer rate falls in the middle, k_{EnT} = 304 ns (Figure 2.7, red line). The trend of the quenching rates indicates that the peptide assembly influences the relative positions of the Ru(II) and Os(II) complexes, and thus their ability to undergo energy transfer, in a predictable manner.

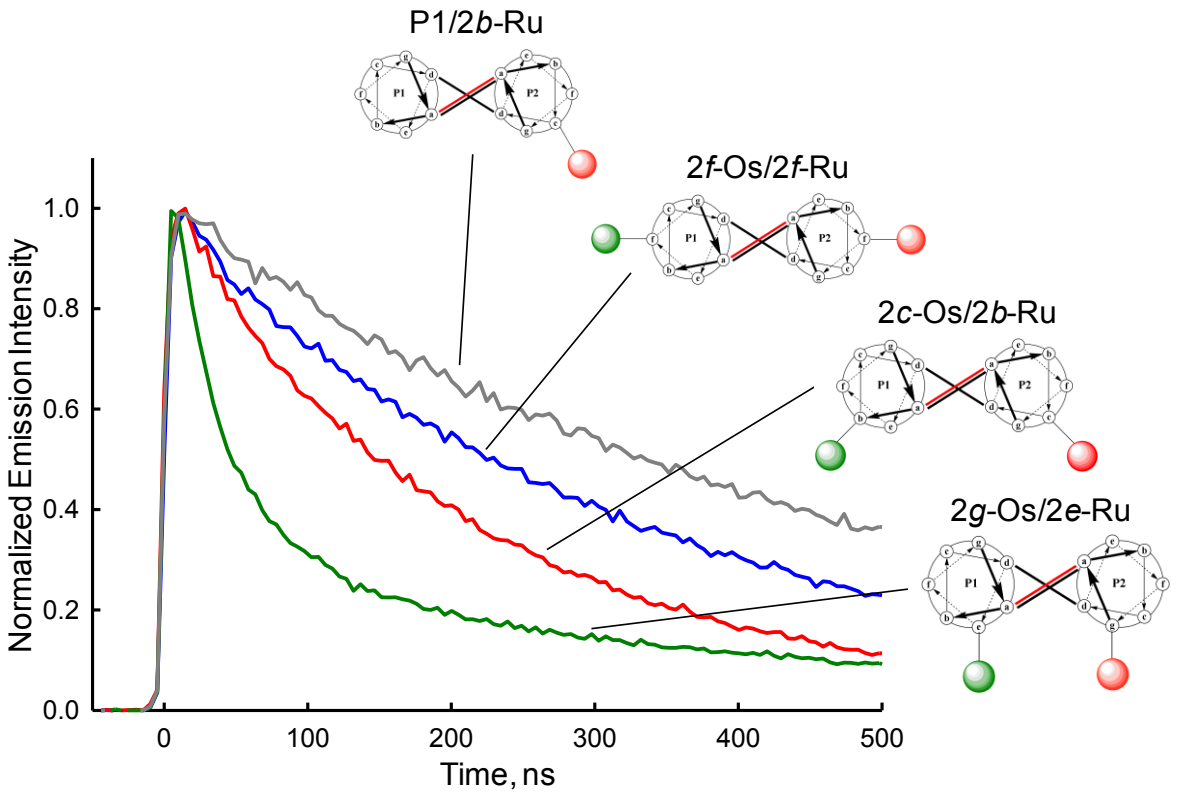

Figure 2.7. Time-resolved emission transients showing the distance dependence of the energy transfer rate for the 2*f*-Os/2*f*-Ru (blue: 25 μM 2*f*-Ru and 50 μM 2*f*-Os), 2*c*-Os/2*b*-Ru (red: 25 μM 2*b*-Ru and 50 μM 2*c*-Os), and 2*g*-Os/2*e*-Ru (green: 25 μM 2*e*-Ru and 50 μM 2g-Os) peptide pairs in 10 mM phosphate buffer solution at pH 7 and 25°C. The P1/2*e*-Ru peptide (grey: 25 μM 2*e*-Ru and 50 μM P1) is shown for comparison. From the transients it is clear that the energy transfer rate is faster the closer the metal complexes are placed to one another. The time-resolved emission data were collected at 660 nm with an excitation wavelength of 444 nm.

2.3.6. Data Analysis

The emission decay was measured in a series of 2*g*-Os/2*e*-Ru samples in which the 2*e*-Ru peptide concentration is kept constant at 25 μM and the 2*g*-Os peptide concentration is incrementally increased from 0 μM to 50 μM (Figures 2.8-2.10). As the 2*g*-Os peptide concentration is increased the slow component decreases in amplitude, consistent with a

diminishing amount of free Ru(II). The relative amplitudes of the two kinetic components reflect the fractions of Ru(II)/Os(II) dimer (fast) and free Ru(II) peptide (slow), resulting in an intensity decay that can be expressed as:

$$I(t) = \left(\frac{[RuOs]}{[Ru]_0}\right) e^{-(k_{Ru}+k_{EnT})t} + \left(\frac{[Ru]_0-[RuOs]}{[Ru]_0}\right) e^{-k_{Ru}t} \tag{2.1}$$

where k_{EnT} is the energy transfer rate and k_{Ru} is the rate of Ru(II) excited state decay. The relative amplitudes of the two components are dependent on the concentration of associated heterodimers, [RuOs], which is determined by the ground state equilibrium:

$$Ru + Os \rightleftarrows RuOs \tag{2.2}$$

$$K_a = \frac{[RuOs]}{[Ru][Os]} = \frac{[RuOs]}{([Ru]_0-[RuOs])([Os]_0-[RuOs])} \tag{2.3}$$

where $[Ru]_0$ and $[Os]_0$ are the total concentrations of the two peptides and K_a is the equilibrium constant.

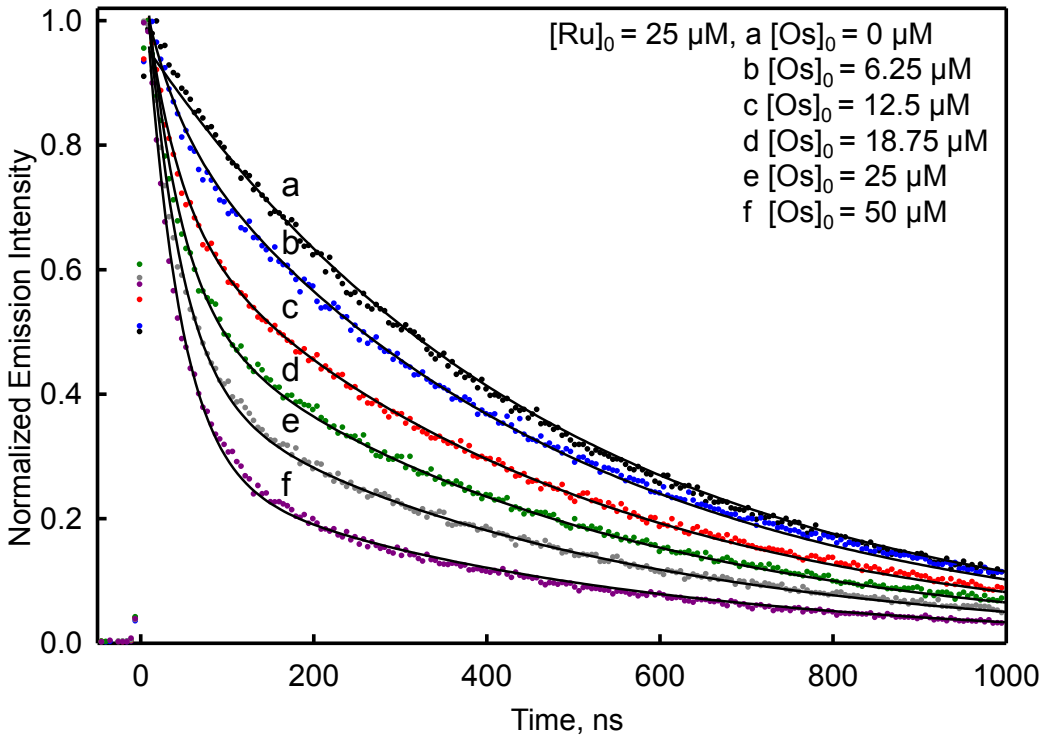

Figure 2.8. Time-resolved emission for P1/2*e*-Ru peptide (black: 25 μM 2*e*-Ru and 50 μM P1) and 2*g*-Os/2*e*-Ru peptide pair containing various amounts of the 2*g*-Os peptide (blue: 6.25 μM, red: 12.5 μM, green: 18.75 μM, grey: 25 μM, and purple: 50 μM with all containing 25 μM 2*e*-Ru) in a 10 mM phosphate buffer solution at pH 7 and 25°C. The increase in 2*g*-Os peptide concentration drives the equilibrium to heterodimer formation and thus greater Ru(II) emission quenching by energy transfer. The time-resolved emission data were collected at 660 nm with an excitation wavelength of 444 nm.

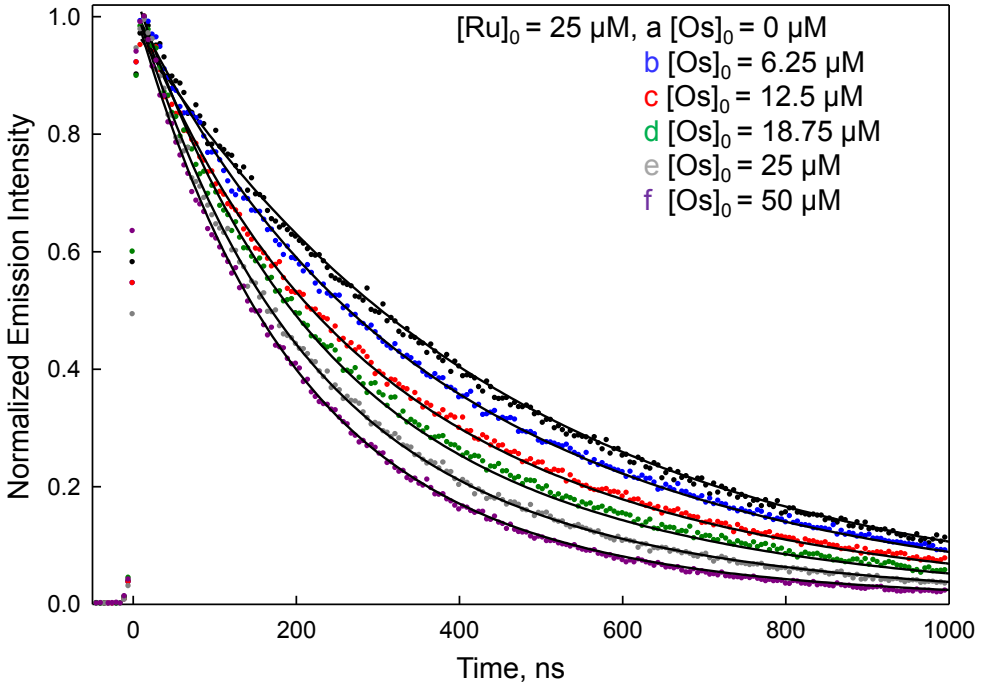

Figure 2.9. Time-resolved emission for P1/2*b*-Ru peptide (black: 25 μM 2*b*-Ru and 50 μM P1) and 2*c*-Os/2*b*-Ru peptide pair containing various amounts of the 2*c*-Os peptide (blue: 6.25 μM, red: 12.5 μM, green: 18.75 μM, grey: 25 μM, and purple: 50 μM with all containing 25 μM 2*b*-Ru) in a 10 mM phosphate buffer solution at pH 7 and collected at 25°C. From the data is you can see that the increase in 2*c*-Os peptide concentration drives the equilibrium to heterodimer formation and thus greater Ru(II) emission quenching by energy transfer. The time-resolved emission data were collected at 660 nm with an excitation of 444 nm.

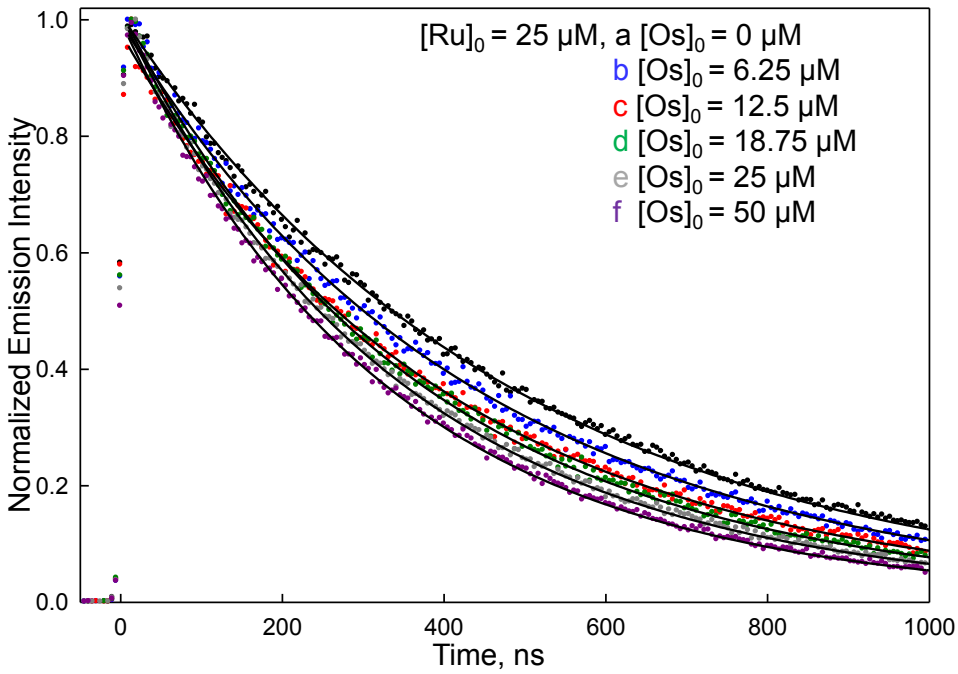

Figure 2.10. Time-resolved emission for P1/2*f*-Ru peptide (black: 25 μM 2*f*-Ru and 50 μM P1) and 2*f*-Os/2*f*-Ru peptide pair containing various amounts of the 2*f*-Os peptide (blue: 6.25 μM, red: 12.5 μM, green: 18.75 μM, grey: 25 μM, and purple: 50 μM with all containing 25 μM 2*f*-Ru) in a 10 mM phosphate buffer solution at pH 7 and collected at 25°C. From the data is you can see that the increase in 2*f*-Os peptide concentration drives the equilibrium to heterodimer formation and thus greater Ru(II) emission quenching by energy transfer. The time-resolved emission data were collected at 660 nm with an excitation of 444 nm.

The solid lines in Figures 2.8-2.10 are the result of a global non-linear least squares fit of the series of decays obtained at different Os(II) concentrations to Equations (2.1-2.3) with k_{EnT}, k_{Ru} and K_a being adjustable parameters. Table 2.1 summarizes the fitting results for the three peptide pairs. The 2*g*-Os/2*e*-Ru peptide pair exhibits the fastest energy transfer with $k_{EnT} = 2.3 \times 10^7\ s^{-1}$ (τ = 42 ns) and the 2*f*-Os/2*f*-Ru peptide pair has the slowest with $k_{EnT} = 1.0 \times 10^6\ s^{-1}$ (τ = 816 ns), and the 2*c*-Os/2*b*-Ru pair fell in the middle at $3.0 \times 10^6\ s^{-1}$ (τ = 304

ns). The relatively slow energy transfer times in comparison with the lifetime of the Os(II) excited state (τ = 16 ns, k = 6.21 x 10^7 s^{-1}) prevents a build-up of Os(II) excited state population. Hence a delayed rise in the Os emission, which has been observed in other systems,[6e] is not observed here. The long linker between the chromophore and the peptide scaffold will cause the attached chromophores to experience a variety of conformations that interconvert on the time scale of the excited state lifetime. Because energy transfer will be more favorable when the two chromophores are in close proximity, the observed rate will likely also reflect the time scale for structural fluctuations.

Table 2.1. Results of the global analysis showing the dependence of the energy transfer rate on the position.[a]

	K_a, μM^{-1} (K_d, μM)	k_{Ru}, x10^6 s^{-1} (lifetime, ns)	k_{EnT}, x10^6 s^{-1} (lifetime, ns)
2*f*-Os/2*f*Ru	0.908 ± 0.005 (1.101 ± 0.006)	2.9 ± 0.002 (478.7 ± 0.5)	1.0 ± 0.02 (816 ± 14)
2*c*-Os/2*b*Ru	0.919 ± 0.001 (1.088 ± 0.002)	2.2 ± 0.002 (450.0 ± 0.5)	3.0 ± 0.02 (304 ± 2)
2*g*-Os/2*e*Ru	0.887 ± 0.001 (1.127 ± 0.001)	2.1 ± 0.002 (468.2 ± 0.4)	23 ± 0.1 (42.0 ± 0.2)

[a]All peptide samples contained 25 μM Ru peptide and 0 to 50 μM Os peptide in 10 mM sodium phosphate buffer at pH 7 and 25°C. The error is from the global fitting analysis.

All-atom molecular dynamics simulations (discussed below) depict the bipyridyl complexes in the 2*g*-Os/2*e*-Ru and 2*c*-Os/2*b*-Ru systems in direct contact, and therefore the energy transfer occurs through Dexter (or electron exchange) energy transfer mechanism.[24] On the other hand, the simulations show the complexes in the 2*f*-Os/2*f*-Ru system remaining at a significant metal-metal separation (3 nm). Therefore, the energy transfer mechanism for

the 2*f*-Os/2*f*-Ru system is unlikely to be through space Dexter energy transfer. However, Förster energy transfer, which occurs through a dipole-dipole mechanism, can occur over larger donor-acceptor separations.[24] Although Förster energy transfer is formally forbidden for triplet-triplet energy transfer, the large spin-orbit coupling in these late transition metal complexes, particularly the Os(II), may provide it with some allowed character.[24] The presence of Förster energy transfer at longer separations is consistent with observations made in other Ru(II)/Os(II) energy transfer systems.[6e,10a-c] Regardless of the mechanism, the coiled-coil peptide system is an effective scaffold for controlling the donor/acceptor placement and hence energy transfer rate in molecular assemblies.

2.3.7. Molecular Modeling

The coiled-coils systems were modeled using all atom molecular dynamics simulations to gain insight into interactions at the molecular level. The simulations were performed by Dr. Christopher Materese and Dr. Maria Minakova from Dr. Papoian's research group. The metal-center distributions for all three coiled-coil peptide systems and the trajectories from which they were derived are shown in Figure 2.11.

The metal-center distributions are non-Gaussian due to the dynamic nature of the peptide coiled-coil system. The dynamic peptides assemblies maintain their α-helical character and exhibit multiple conformations that interchange on the nanosecond timescale. The variety of chromophore geometries is highlighted in Figure 2.12. The metal-centered distances measured in the simulations agree with the photophysical measurements, with the 2*g*-Os/2*e*-Ru peptide system exhibiting the shortest metal-centered distance and 2*f*-Os/2*f*-Ru system the longest metal-center distance. The simulations resulted in an average metal-

centered distance of 12 Å for the 2*g*-Os/2*e*-Ru system, 14 Å for the 2*c*-Os/2b-Ru system and 31 Å for the 2*f*-Os/2*f*-Ru system.

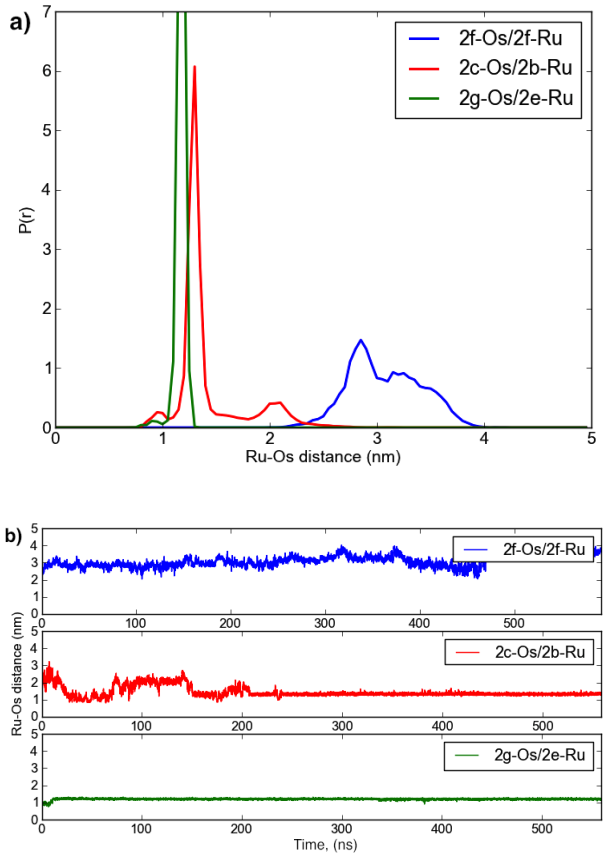

Figure 2.11. (A) Comparative plot of Ru-Os distance histograms (normalized) for different chromophore placements, including 2*f*-Os/2*f*-Ru, 2*c*-Os/2*b*-Ru, and 2*g*-Os/2*e*-Ru. (B) Ru-Os distance evolution in time for the 2*f*-Os/2*f*-Ru, 2*c*-Os/2*b*-Ru, and 2*g*-Os/2*e*-Ru metallopeptide pairs.

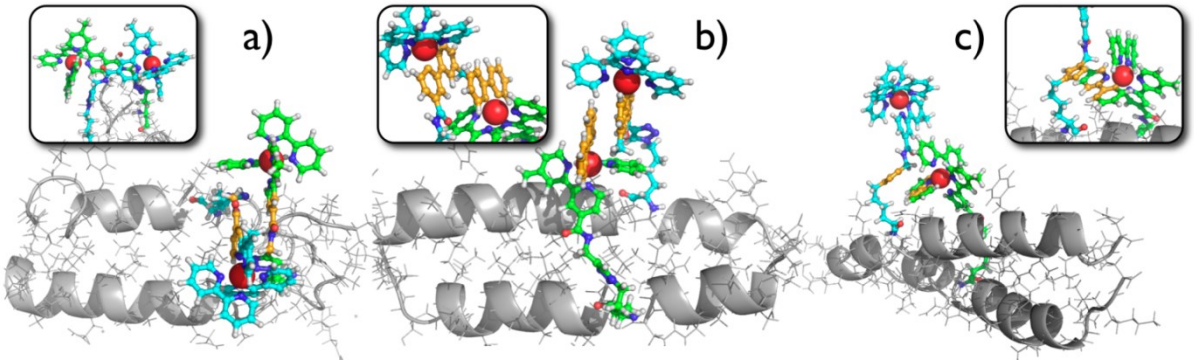

Figure 2.12. (A) Bipyridyl ligands arranged in a "neck" conformation, facing away from each other (1.2 nm feature). This conformation was only observed in the 2g-Os/2e-Ru system. (B) π-π stacking arrangement where bipyridyl rings of two complexes are in Van der Waals contact and parallel to each other (~1 nm feature). This tightly stacked conformation is observed consistently in 2c-Os/2b-Ru system and briefly in 2g-Os/2e-Ru system. (C) "Loose" packing arrangement of the bipyridyl complexes (~2 nm feature) is a stable basin of conformations with characteristic π-π stacking of one of bipyridine rings of one chromophore and the triazole ring on the linker of the other. This stacking is stable in 2c-Os/2b-Ru system and transitory to closer intercomplex packing conformations in 2g-Os/2e-Ru system.

2.4. CONCLUSIONS

The ability to control the positioning and organization of molecular components is central to the design of functional molecular-based materials.[3] However, architectures that rely solely on covalent bonding for structure (e.g. polymers, dendrimers) have limited control over the assembly geometry and higher-order spatial control. Using peptides as scaffolds, an artificial self-assembling system has been designed that utilizes weak forces to control the relative placement of Ru(II) and Os(II) complexes. The assemblies incorporate an α-helical coiled-coil peptide scaffold consisting of α-helical heterodimers in which each coil is functionalized with either a Ru(II)-containing energy donor or with an Os(II)-containing energy acceptor. This architecture differs from many other types of molecular assemblies in that it uses both intra- and intermolecular noncovalent interactions to adopt well-defined

secondary and tertiary structures that control the placement of the energy transfer complexes. Moreover, the use of "click" chemistry allows for straight-forward and well defined control of the placement of the covalently linked chromophores.

Circular dichroism spectroscopy in conjunction with time-resolved emission spectroscopy confirms the importance of the heterodimeric α-helical coiled-coil structure for modulating energy transfer. Ru(II) to Os(II) energy transfer is only observed in the folded structures, and energy transfer rates measured across a series of supramolecular structures are consistent with a systematic variation of the metal complex separation. Chemical agents that denature the peptide scaffold also serve as an on-off switch, and completely disable energy transfer. Molecular dynamics simulations show Ru(II)-Os(II) distance distributions that are consistent with the order of the experimentally measured energy transfer rates. In addition, the simulations suggest that the assemblies maintain their α-helical character, but are dynamic in nature, with multiple conformations interchanging on the nanosecond timescale, despite stable cores. These studies demonstrate the sequence-structure-function paradigm found in natural proteins in a robust artificial self-assembling system and clearly establishes the essential role the supramolecular scaffold plays in controlling function. This system provides a promising new scaffold for functional materials that couples straight-forward synthesis with fine control of three dimensional structure that directly dictates function.

REFERENCES

(1) (a) Astruc, D.; Boisselier, E.; Ornelas, C. *Chem. Rev.* 2010, *110*, 1857-1959. (b) Drain, C. M.; Varotto, A.; Radivojevic, I. *Chem. Rev.* 2009, *109*, 1630-1658. (c) Szacilowski, K. *Chem. Rev.* 2008, *108*, 3481-3548. (d) Hoeben, F. J. M.; Jonkheijm, P.; Meijer, E. W.; Schenning, A. *Chem. Rev.* 2005, *105*, 1491-1546.

(2) (a) Lakowicz, J. R. *Priciples of Fluorescence Spectroscopy*; 3rd ed.; Springer: New York, 2006. (b) McDonagh, C.; Burke, C. S.; MacCraith, B. D. *Chem. Rev.* 2008, *108*, 400-422.

(3) (a) Meyer, T. J. *Acc. Chem. Res.* 1989, *22*, 163-170. (b) Alstrum-Acevedo, J. H.; Brennaman, M. K.; Meyer, T. J. *Inorg. Chem.* 2005, *44*, 6802-6827. (c) Gust, D.; Moore, T. A.; Moore, A. L. *Acc. Chem. Res.* 2009, *42*, 1890-1898. (d) Gust, D.; Moore, T. A. *Science* 1989, *244*, 35-41.

(4) (a) Du, P. W.; Schneider, J.; Luo, G. G.; Brennessel, W. W.; Eisenberg, R. *Inorg. Chem.* 2009, *48*, 4952-4962. (b) Youngblood, W. J.; Lee, S. H. A.; Maeda, K.; Mallouk, T. E. *Acc. Chem. Res.* 2009, *42*, 1966-1973. (c) Bonchio, M.; Carofiglio, T.; Carraro, M.; Fornasier, R.; Tonellato, U. *Org. Lett.* 2002, *4*, 4635-4637.

(5) (a) Hsiao, J. S.; Krueger, B. P.; Wagner, R. W.; Johnson, T. E.; Delaney, J. K.; Mauzerall, D. C.; Fleming, G. R.; Lindsey, J. S.; Bocian, D. F.; Donohoe, R. J. *J. Am. Chem. Soc.* 1996, *118*, 11181-11193. (b) Wagner, R. W.; Lindsey, J. S. *J. Am. Chem. Soc.* 1994, *116*, 9759-9760. (c) Song, H.; Taniguchi, M.; Speckbacher, M.; Yu, L.; Bocian, D. F.; Lindsey, J. S.; Holten, D. *J. Phys. Chem. B* 2009, *113*, 8011-8019. (d) Bellows, D.; Goudreault, T.; Aly, S. M.; Fortin, D.; Gros, C. P.; Barbe, J.-M.; Harvey, P. D. *Organometallics* 2010, *29*, 317-325.

(6) (a) Jones, W. E.; Baxter, S. M.; Strouse, G. F.; Meyer, T. J. *J. Am. Chem. Soc.* 1993, *115*, 7363-7373. (b) Dupray, L. M.; Meyer, T. J. *Inorg. Chem.* 1996, *35*, 6299-6307. (c) Dupray, L. M.; Devenney, M.; Striplin, D. R.; Meyer, T. J. *J. Am. Chem. Soc.* 1997, *119*, 10243-10244. (d) Friesen, D. A.; Kajita, T.; Danielson, E.; Meyer, T. J. *Inorg. Chem.* 1998, *37*, 2756-2762. (e) Fleming, C. N.; Maxwell, K. A.; DeSimone, J. M.; Meyer, T. J.; Papanikolas, J. M. *J. Am. Chem. Soc.* 2001, *123*, 10336-10347. (f) Sowash, G. G.; Webber, S. E. *Macromolecules* 1988, *21*, 1608-1611. (g) Webber, S. E. *Chem. Rev.* 1990, *90*, 1469-1482.

(7) (a) Marcaccio, M.; Paolucci, F.; Paradisi, C.; Roffia, S.; Fontanesi, C.; Yellowlees, L. J.; Serroni, S.; Campagna, S.; Denti, C.; Balzani, V. *J. Am. Chem. Soc.* 1999, *121*, 10081-10091. (b) Campagna, S.; Denti, G.; Serroni, S.; Juris, A.; Venturi, M.; Ricevuto, V.; Balzani, V. *Chem. Eur. J.* 1995, *1*, 211-221. (c) Van Patten, P. G.; Shreve, A. P.; Lindsey, J. S.; Donohoe, R. J. *J. Phys. Chem. B* 1998, *102*, 4209-4216. (d) Xu, Z. F.; Moore, J. S. *Acta Polym.* 1994, *45*, 83-87. (e) Balzani, V.; Campagna, S.; Denti, G.; Juris, A.; Serroni, S.; Venturi, M. *Acc. Chem. Res.* 1998, *31*, 26-34. (f) Tsukube, H.; Suzuki, Y.; Paul, D.; Kataoka, Y.; Shinoda, S. *Chem. Commun.* 2007, 2533-2535. (g) Stapert, H. R.; Nishiyama, N.; Jiang, D. L.; Aida, T.; Kataoka, K. *Langmuir* 2000, *16*, 8182-8188. (h) Ahn, T. S.; Thompson, A. L.; Bharathi, P.; Muller, A.; Bardeen, C. J. *J. Phys. Chem. B* 2006, *110*, 19810-19819. (i) Nantalaksakul, A.; Reddy, D. R.; Bardeen, C. J.; Thayumanavan, S. *Photosynth. Res.* 2006, *87*, 133-150. (j) Larsen, J.; Puntoriero, F.; Pascher, T.; McClenaghan, N.; Campagna, S.; Akesson, E.; Sundstrom, V. *Chemphyschem* 2007, *8*, 2643-2651. (k) Andersson, J.; Puntoriero, F.; Serroni, S.; Yartsev, A.; Pascher, T.; Polivka, T.; Campagna, S.; Sundstrom,

V. *Faraday Discuss.* 2004, *127*, 295-305. (l) Thomas, K. R. J.; Thompson, A. L.; Sivakumar, A. V.; Bardeen, C. J.; Thayumanavan, S. *J. Am. Chem. Soc.* 2005, *127*, 373-383.

(8) (a) Giansante, C.; Raffy, G.; Schaefer, C.; Rahma, H.; Kao, M.-T.; Olive, A. G. L.; Del Guerzo, A. *J. Am. Chem. Soc.* 2011, *133*, 316-325. (b) Babu, S. S.; Kartha, K. K.; Ajayaghosh, A. *Journal of Physical Chemistry Letters* 2010, *1*, 3413-3424. (c) Ajayaghosh, A.; Praveen, V. K.; Vijayakumar, C. *Chem. Soc. Rev.* 2008, *37*, 109-122. (d) Bhattacharya, S.; Samanta, S. K. *Langmuir* 2009, *25*, 8378-8381.

(9) Ferreira, K. N.; Iverson, T. M.; Maghlaoui, K.; Barber, J.; Iwata, S. *Science* 2004, *303*, 1831-1838.

(10) (a) Hurley, D. J.; Tor, Y. *J. Am. Chem. Soc.* 1998, *120*, 2194-2195. (b) Hurley, D. J.; Tor, Y. *J. Am. Chem. Soc.* 2002, *124*, 3749-3762. (c) Hurley, D. J.; Tor, Y. *J. Am. Chem. Soc.* 2002, *124*, 13231-13241. (d) Lewis, F. D.; Zhang, L. G.; Zuo, X. B. *J. Am. Chem. Soc.* 2005, *127*, 10002-10003. (e) Holmlin, R. E.; Tong, R. T.; Barton, J. K. *J. Am. Chem. Soc.* 1998, *120*, 9724-9725.

(11) Channon, K. J.; Devlin, G. L.; MacPhee, C. E. *J. Am. Chem. Soc.* 2009, *131*, 12520-12521.

(12) Nam, Y. S.; Shin, T.; Park, H.; Magyar, A. P.; Choi, K.; Fantner, G.; Nelson, K. A.; Belcher, A. M. *J. Am. Chem. Soc.* 2010, *132*, 1462-1463.

(13) (a) Stryer, L.; Haugland, R. P. *Proc. Natl. Acad. Sci.* 1967, *58*, 719-726. (b) Pispisa, B.; Venanzi, M.; Palleschi, A.; Zanotti, G. *Macromolecules* 1994, *27*, 7800-7808. (c) McGimpsey, W. G.; Chen, L.; Carraway, R.; Samaniego, W. N. *J. Phys. Chem. A* 1999, *103*, 6082-6090. (d) Pispisa, B.; Stella, L.; Venanzi, M.; Palleschi, A.; Viappiani, C.; Polese, A.;

Formaggio, F.; Toniolo, C. *Macromolecules* 2000, *33*, 906-915. (e) Sahoo, H.; Roccatano, D.; Hennig, A.; Nau, W. M. *J. Am. Chem. Soc.* 2007, *129*, 9762-9772.

(14) Photoexcited-state electron transfer is phenomenon closely related to energy transfer and has been extensively studied in a number of different peptide systems. (a) Mecklenburg, S. L.; Peek, B. M.; Erickson, B. W.; Meyer, T. J. *J. Am. Chem. Soc.* 1991, *113*, 8540-8542. (b) Mecklenburg, S. L.; Peek, B. M.; Schoonover, J. R.; McCafferty, D. G.; Wall, C. G.; Erickson, B. W.; Meyer, T. J. *J. Am. Chem. Soc.* 1993, *115*, 5479-5495. (c) Mecklenburg, S. L.; McCafferty, D. G.; Schoonover, J. R.; Peek, B. M.; Erickson, B. W.; Meyer, T. J. *Inorg. Chem.* 1994, *33*, 2974-2983. (d) McCafferty, D. G.; Bishop, B. M.; Wall, C. G.; Hughes, S. G.; Mecklenberg, S. L.; Meyer, T. J.; Erickson, B. W. *Tetrahedron* 1995, *51*, 1093-1106.

(15) (a) Kozlov, G. V.; Ogawa, M. Y. *J. Am. Chem. Soc.* 1997, *119*, 8377-8378. (b) Kornilova, A. Y.; Wishart, J. F.; Ogawa, M. Y. *Biochemistry* 2001, *40*, 12186-12192. (c) Kornilova, A. Y.; Wishart, J. F.; Xiao, W. Z.; Lasey, R. C.; Fedorova, A.; Shin, Y. K.; Ogawa, M. Y. *J. Am. Chem. Soc.* 2000, *122*, 7999-8006. (d) Fedorova, A.; Chaudhari, A.; Ogawa, M. Y. *J. Am. Chem. Soc.* 2003, *125*, 357-362. (e) Fedorova, A.; Ogawa, M. Y. *Bioconjugate Chem.* 2002, *13*, 150-154. (f) Hong, J.; Kharenko, O. A.; Ogawa, M. Y. *Inorg. Chem.* 2006, *45*, 9974-9984.

(16) Crick, F. H. C. *Nature* 1952, *170*, 882-883.

(17) (a) Talbot, J. A.; Hodges, R. S. *Acc. Chem. Res.* 1982, *15*, 224-230. (b) Holtzer, A.; Holtzer, M. E. *Macromolecules* 1987, *20*, 671-675.

(18) (a) D. N. Woolfson, Advances in Protein Chem, 2005, 70, 79-112. (b) Pandya, M. J.; Spooner, G. M.; Sunde, M.; Thorpe, J. R.; Rodger, A.; Woolfson, D. N. *Biochemistry* 2000, *39*, 8728-8734. (c) Ryadnov, M. G.; Woolfson, D. N. *Angew. Chem., Int. Ed.* 2003, *42*, 3021-

3023. (d) Ryadnov, M. G.; Woolfson, D. N. *Nat. Mater.* 2003, *2*, 329-332. (e) Ryadnov, M. G.; Woolfson, D. N. *J. Am. Chem. Soc.* 2004, *126*, 7454-7455. (f) Mahmoud, Z. N.; Gunnoo, S. B.; Thomson, A. R.; Fletcher, J. M.; Woolfson, D. N. *Biomat.* 2011, *32*, 3712-3720.

(19) (a) Oshea, E. K.; Klemm, J. D.; Kim, P. S.; Alber, T. *Science* 1991, *254*, 539-544. (b) Harbury, P. B.; Zhang, T.; Kim, P. S.; Alber, T. *Science* 1993, *262*, 1401-1407. (c) Woolfson, D. N.; Alber, T. *Protein Sci.* 1995, *4*, 1596-1607.

(20) (a) Oshea, E. K.; Rutkowski, R.; Kim, P. S. *Cell* 1992, *68*, 699-708. (b) Kohn, W. D.; Kay, C. M.; Hodges, R. S. *J. Mol. Biol.* 1998, *283*, 993-1012. (c) Litowski, J. R.; Hodges, R. S. *J. Biol. Chem.* 2002, *277*, 37272-37279. (d) Zhou, N. E.; Kay, C. M.; Hodges, R. S. *J. Mol. Biol.* 1994, *237*, 500-512.

(21) (a) Lumb, K. J.; Kim, P. S. *Biochemistry* 1995, *34*, 8642-8648. (b) Oakley, M. G.; Kim, P. S. *Biochemistry* 1998, *37*, 12603-12610. (c) Gonzalez, L.; Woolfson, D. N.; Alber, T. *Nat. Struct. Biol.* 1996, *3*, 1011-1018.

(22) (a) Woody, R. W. *Biochemical Spectroscopy* 1995, *246*, 34-71. (b) Greenfield, N. J. *Nature Protocols* 2006, *1*, 2876-2890. (c) Hodges, R. S. *Biochem. Cell Biol.* 1996, *74*, 133-154. (d) Zhou, N. E.; Zhu, B. Y.; Kay, C. M.; Hodges, R. S. *Biopolymers* 1992, *32*, 419-426.

(23) Juris, A.; Balzani, V.; Barigelletti, F.; Campagna, S.; Belser, P.; Vonzelewsky, A. *Coord. Chem. Rev.* 1988, *84*, 85-277.

(24) (a) Dexter, D. L. *J. Chem. Phys.* 1953, *21*, 836-850. (b) Förster, Th. *Discuss. Faraday Soc.* 1959, *27*, 7-17. (c) Murtaza, Z.; Graff, D. K.; Zipp, A. P.; Worl, L. A.; Jones, W. E.; Bates, W. D.; Meyer, T. J. *J. Phys. Chem.* 1994, *98*, 10504-10513.

CHAPTER 3. INTERFACIAL ENERGY CONVERSION IN RU(II) POLYPYRIDYL-DERIVATIZED OLIGOPROLINE ASSEMBLIES ON TIO_2[2]

[2]This chapter previously appeared as an article in the Journal of the American Chemical Society. The original citation is as follows: Ma, D.; Bettis, S. E., Hanson, K.; Minakova, M.; Alibabaei, L.; Fondrie, W.; Ryan, D. M.; Papoian, G. A.; Meyer, T.J.; Papanikolas, J. M.; Waters, M. L. *J. Am. Chem. Soc*., 2013, 135 (14), 5250–5253.

3.1. INTRODUCTION

Molecular structure and organization are key elements in molecular-level energy conversion. An object lesson is photosystem II (PSII) in natural photosynthesis where light-driven oxidation of water occurs. Absorption of light in an antenna complex drives a sequence of five electron transfer reactions resulting in oxidative activation of the oxygen evolving complex (OEC) and delivery of a reductive equivalent, as the semiquinone form of plastoquinone, separated by a distance of ~50 Å.[1,2]

At the heart of PSII is a structurally controlled array of light absorbers, electron transfer relays, and catalysts in the thylakoid membranes of chloroplasts. Mimicking these features, both in content and relative orientation, in an artificial device poses a significant synthetic challenge. The systematic strategy reported here is based on solid phase peptide synthesis (SPPS) combined with the copper catalyzed azide-alkyne cycloaddition (CuAAC or 'click' reaction) for modular synthesis of a spatially pre-organized bichromophoric assembly.[3] This strategy has been applied to the preparation of an interfacial assembly for photochemical electron and energy transfer when bound in nanocrystalline films of TiO_2.

A number of strategies have been explored for the preparation of light harvesting assemblies including porphyrin arrays,[4] polymers,[5] DNA,[6] dendrimers,[7] metal-organic frameworks (MOFs),[8] and molecular assemblies.[9] For interfacial applications, as in dye-sensitized solar cells (DSSC)[10] or dye-sensitized photoelectrosynthesis cells (DSPEC),[11] it is important to combine broad visible-near IR absorption with directional control of energy and electron transfer toward the semiconductor interface. Several examples of surface-bound assemblies have been discussed in the context of DSSCs,[12] but lack detailed kinetic analysis of the excited state photophysics.

Controlling the direction of electron and energy transfer requires the control of chromophore positioning and orientation relative to the surface as well as the ability to incorporate different chromophores at specific positions. Peptides are useful as molecular scaffolds for multiple functional units due to the ability to encode highly ordered secondary and tertiary structures based on their amino acid sequence. Oligoprolines with at least five proline residues are particularly notable in this regard because they form left-handed polyproline II (PPII) helices in polar solvents, providing a rigid scaffold for positioning multiple chromophores.[13] Additionally, SPPS allows for absolute control of the positioning of functional groups. With application of 'click' coupling, the amino acid sequence can be modified systematically with assembly structures by incorporating the appropriate functional groups (i.e. azide or alkyne) at specific locations in the peptide sequence.[3] This offers the additional advantage of incorporating molecular components with different functionalities (e.g. light-harvesting chromophores and molecular catalysts for water splitting) with a high degree of structural control.

The well-defined structural characteristics of oligoprolines[14] and other peptide scaffolds[15] have been exploited previously to investigate the distance dependence of electron and energy transfer in Ru^{II}-bpy modified derivatives. In this study, ultrafast transient spectroscopic measurements are used to evaluate intra-assembly energy transfer and excited-state injection in an oligoproline assembly containing two different chromophores on the surface of nano-structured films of TiO_2.[16]

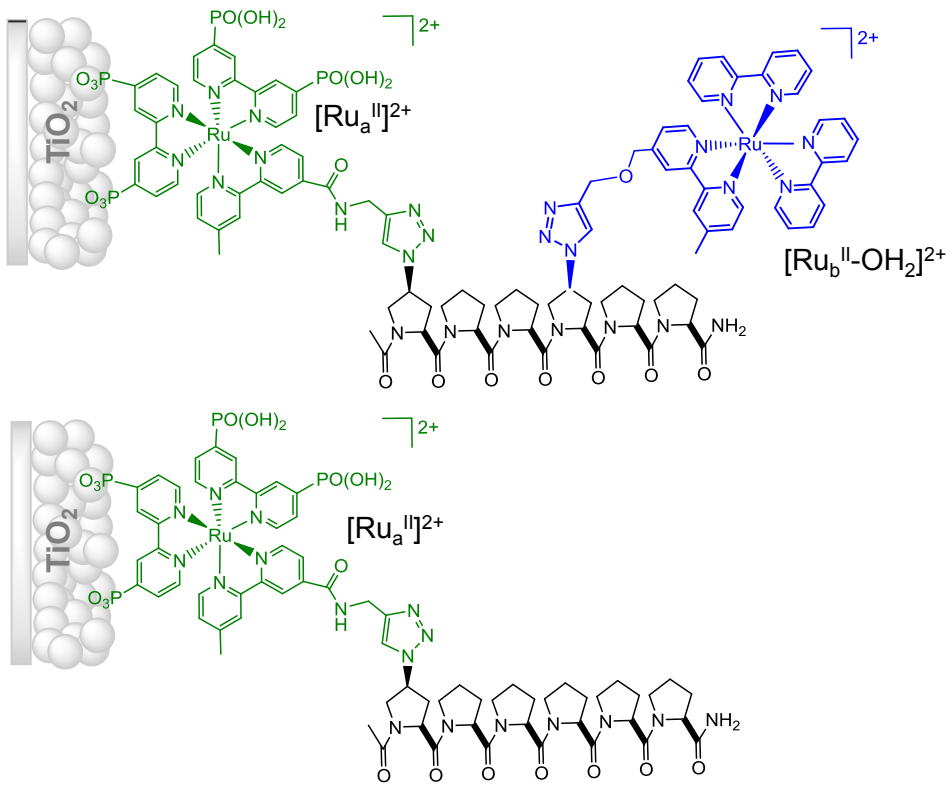

Figure 3.1. Structure of $[Ru_a^{II}]^{2+}$ and $[Ru_a^{II}\text{-}Ru_b^{II}]^{4+}$ on nanocrystalline TiO2 films.

Two peptide-chromophore assemblies investigated were synthesized by Dr. Da Ma in Dr. Waters group and are shown in Figure 3.1. The control assembly $[Ru_a^{II}]^{2+}$ contains only the inner chromophore $Ru_a^{II} = [Ru(pbpy)_2(L1)]^{2+}$ (pbpy = 4,4′-$(PO_3H_2)_2$-2,2′-bipyridine, L1 = 4′-methyl-(2,2′-bipyridine)-4-propargyl amide), which binds directly to the surface. The second assembly $[Ru_a^{II}\text{-}Ru_b^{II}]^{4+}$ contains both an inner and outer chromophore Ru_a^{II} and $Ru_b^{II} = [Ru(L2)(bpy)_2]^{2+}$ (L2 = 4′-methyl-(2,2′-bipyridine)-4-dimethyl-ether). The design of structure $[Ru_a^{II}\text{-}Ru_b^{II}]^{4+}$ was guided by: 1) having six proline residues to induce helical secondary structure; 2) including a Ru^{II} polypyridyl complex with phosphonate-derivatized bipyridine ligands for binding to metal oxide surfaces;[17] 3) using a two-proline spacer unit between the Ru^{II} chromophores, which in the PPII helix (Figure 3.2), aligns the two chromophores on the same side of the helix and minimizes their internuclear separation

distance; 4) incorporating Ru^{II} chromophores with metal-to-ligand charge transfer (MLCT) excited states "tuned" to create an energy transfer gradient toward the interface. Although subtle, the latter feature is present in $[Ru_a^{II}\text{-}Ru_b^{II}]^{4+}$ because of the electronic effects of the substituents on the π* acceptor levels in the MLCT excited states of $[Ru_a^{II}]^{2+}$. The unfunctionalized bpy ligands in $[Ru_b^{II}]^{2+}$ form an excited state that is slightly higher in energy than the functionalized ligands on $[Ru_a^{II}]^{2+}$.

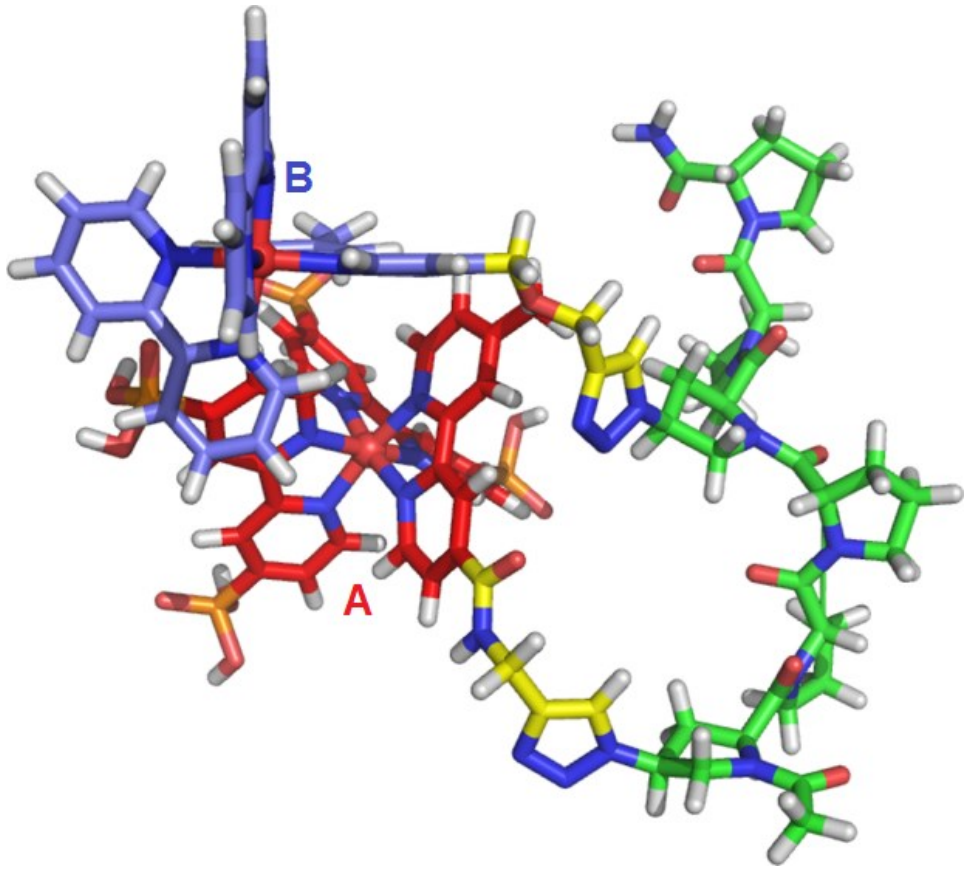

Figure 3.2. All atom molecular dynamics simulation of $[Ru_a^{II}\text{-}Ru_b^{II}]^{4+}$ in solution showing the Ru^{II} chromophores in close contact. Green indicates oligoproline backbone, yellow indicates linkers, red indicated chromophore $[Ru_a^{II}]^{2+}$, and blue indicates chromophore $[Ru_b^{II}]^{2+}$.

In water, at pH = 1.0, pH = 4.0, pH = 7.4, or in MeOH, the assembly $[Ru_a^{II}\text{-}Ru_b^{II}]^{4+}$ exhibits left handed PPII helical structure as indicated by circular dichroism performed by Dr. Da Ma.[16] Molecular dynamics simulations, performed by Dr. Maria Minakova, support the formation of a PPII helical conformation (Figure 3.2) with the chromophores in close contact and an average Ru-Ru spacing of 13 Å.[16]

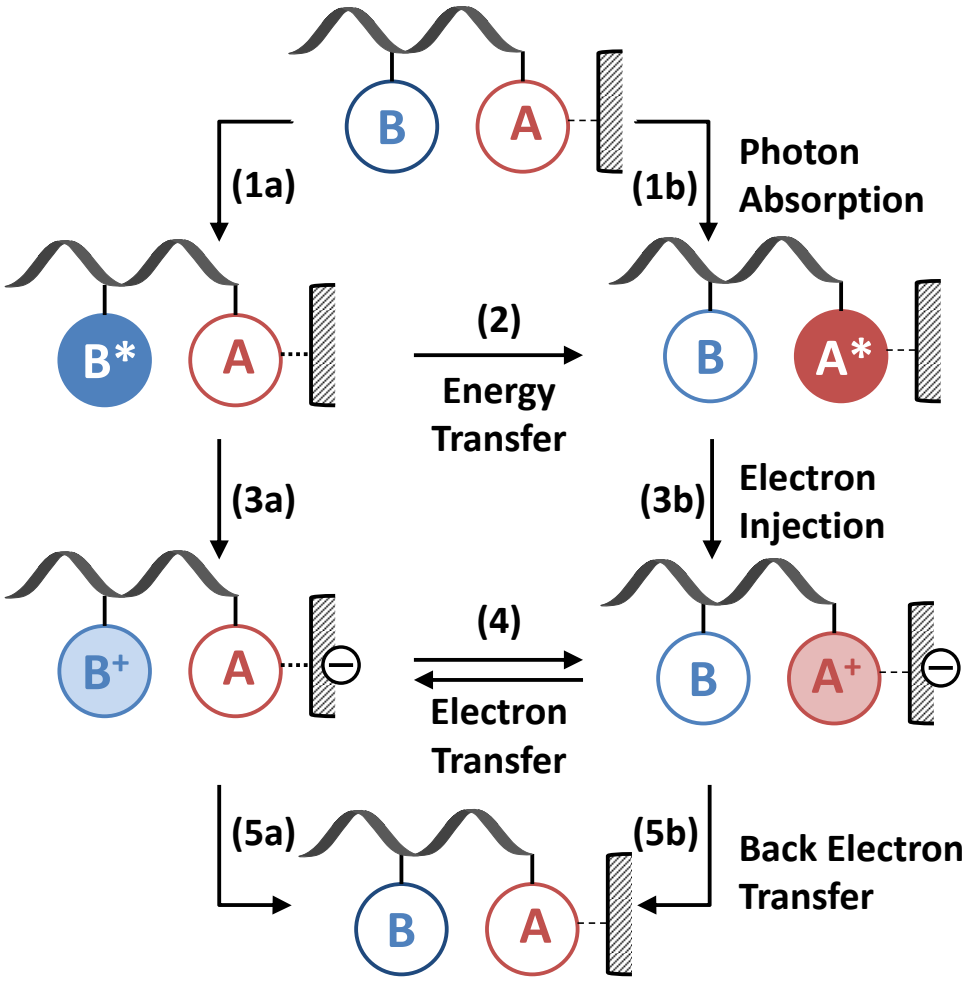

Scheme 3.1. Schematic representation of photophysical events of $[Ru_a^{II}\text{-}Ru_b^{II}]^{4+}$ on nanocrystalline TiO_2.

The dynamic events anticipated to occur following transient excitation of TiO_2-[Ru_a^{II}-Ru_b^{II}]$^{4+}$ on are illustrated in Scheme 3.1. Photon absorption can occur at either chromophore. Photoexcitation at the inner chromophore [Ru_a^{II}*]$^{2+}$ is expected to result in rapid electron injection into TiO_2 (TiO_2-[Ru_a^{II}*-Ru_b^{II}]$^{4+}$→TiO_2(e^-)-[Ru_a^{III}-Ru_b^{II}]$^{5+}$) as previously observed for TiO_2-[Ru^{II}(pbpy)(bpy)$_2$]$^{2+}$ (Scheme 3.1, Eq. 1b).[18] Deactivation of [Ru_b^{II}*]$^{2+}$ can occur either by energy transfer to [Ru_a^{II}]$^{2+}$ (TiO_2-[Ru_a^{II}-Ru_b^{II}*]$^{4+}$→TiO_2-[Ru_a^{II}*-Ru_b^{II}]$^{4+}$, Scheme 3.1, Eq. 2) followed by electron injection from [Ru_a^{II}*]$^{2+}$ (Scheme 3.1, Eq. 3b) or by remote injection from [Ru_b^{II}*] (Scheme 3.1, Eq. 3a). Following electron injection, electron transfer from [Ru_b^{II}] to [Ru_a^{III}]$^{3+}$ (TiO_2(e^-)-[Ru_a^{III}-Ru_b^{II}]$^{5+}$→TiO_2(e^-)-[Ru_a^{II}-Ru_b^{III}]$^{5+}$, Scheme 3.1, Eq. 4) is energetically favorable by ~130 mV as indicated by electrochemical measurements. Ultimately the electron in TiO_2 will recombine with the oxidized complex ([Ru_a^{III}]$^{3+}$ or [Ru_b^{III}]$^{3+}$) through back electron transfer (Scheme 3.1, Eq. 5).

The work described in this chapter was published in *Journal of the American Chemical Society* (Ma, D.; Bettis, S.E., et al. *JACS.* 2013, 135 (14), 5250–5253.). The paper was a result of collaboration between three research groups lead by Dr. Marcey Waters, Dr. John Papanikolas and Dr. Garegin A. Papoian. The peptide system was synthesized and structurally characterized by Dr. Da Ma in Dr. Waters' group. The all-atom simulations were performed by Dr. Maria Minakova in Dr. Papoian's group. The contribution I made included the photophysical analysis of the peptides and is described in detail in this chapter. The work of my collaborators is summarized in this chapter, and described in detail in our published paper.

3.2. EXPERIMENTAL METHODS

3.2.1. Sample Preparation

All samples were loaded onto 3 μm thick nanocrystalline films of TiO_2 and ZrO_2 by soaking overnight in a 150 mM aqueous 0.1 M $HClO_4$ solution. The surface coverage (Γ) was estimated using Equation 3.1.[19]

$$\Gamma = A(\lambda) / \varepsilon(\lambda) / 1000 \qquad (3.1)$$

The absorbance, A(λ), was taken at the maximum wavelength 450 nm and the molar extinction coefficient at that wavelength, ε(λ), of 14,500 cm^{-1} was used for the estimation. $[Ru^{II}(pbpy)(bpy)_2]^{2+}$, which exhibits full surface coverage,[18] has a surface coverage of Γ = 8.6 x 10^{-8} mol/cm^2 (2.9 x 10^{-8} mol/cm^2/μm).

The surface coverage for TiO_2-$[Ru_a^{II}]^{2+}$ and TiO_2-$[Ru_a^{II}$-$Ru_b^{II}]^{4+}$ are nearly full with Γ = 2.6 x 10^{-8} mol/cm^2/μm and 2.4 x 10^{-8} mol/cm^2/μm respectively and Γ = 1.8 x 10^{-8} mol/cm^2/μm and 1.7 x 10^{-8} mol/cm^2/μm for ZrO_2-$[Ru_a^{II}]^{2+}$ and ZrO_2-$[Ru_a^{II}$-$Ru_b^{II}]^{4+}$ respectively.[18] The films were placed in a 1.0 cm cuvette at 45 degree angle from the incident laser beam. The solution experiments were done in 2.0 mm cuvette placed at 45 degrees from the incident beam. All samples were in aqueous 0.1 M $HClO_4$ and purged in Argon for >45 minutes just prior to data collection.

3.2.2. Steady-state Techniques

Ground state absorbance measurements were conducted with a Hewlett Packard 8453 UV-VIS-NIR absorption spectrophotometer. Steady state emission (SSE) data were collected using an Edinburgh Instruments FLS920 equipped with a 450 W Xenon lamp and photomultiplier tube (Hamamatsu 2658P). SSE data were collected using a bandwidth no

larger than 4.0 nm and, once collected, were corrected for the emission spectrophotometer's spectral response.

The emission spectra were fit using a single-mode Franck-Condon analysis using Equation 3.2.

$$I(\bar{\nu}) = \sum_{\nu}^{5} \left\{ \left(\frac{E_0 - \nu\hbar\omega}{E_0} \right)^3 \frac{S^{\nu}}{V!} \times \exp\left[-4\ln 2 \left(\frac{(E - E_0 + \nu\hbar\omega}{\Delta\bar{\nu}_{0,1/2}} \right)^2 \right] \right\} \tag{3.2}$$

The output of the fit included four parameters: E_0, S, $\hbar\omega$, and $\Delta\bar{\nu}_{0,1/2}$. The energy gap between the lowest energy level excited state and the ground state is represented by E_0, the electron-vibrational coupling constant is S, the medium frequency mode of quantum spacing is $\hbar\omega$, and the full width half-maximum of the 0-0 vibronic component is $\Delta\bar{\nu}_{0,1/2}$.[20-23] It is noted that the $\hbar\omega$ term was fixed at 1350 cm^{-1} from the precedent set in the literature for ruthenium(II) polypyridyl complexes.[21,24] The emission spectral fitting was done with least-squares analysis with a confidence limit of 5%, but the significant figures of the parameters are limited by the 50 cm^{-1} resolution of the instrument. The driving force for energy transfer (ΔG) was calculated with Equations 3.3 and 3.4.[22]

$$\chi' = (\Delta\bar{\nu}_{0,1/2})^2 / 16\ln 2 k_b T \tag{3.3}$$

$$\Delta G^{\circ} = (E_{0,(A^*/A)} + \chi'_A) - (E_{0,(D^*/D)} + \chi'_D) \tag{3.4}$$

The calculation used the E_0 from the emission spectral fitting of the donor and the acceptor and the χ' value for the donor and acceptor. The χ' term was calculated in Equation 3.2

using the $\Delta\bar{\nu}_{0,1/2}$ term from the fits, along with Boltzman's constant k_b and the temperature, T. The calculated driving force for energy transfer was ΔG = -70meV.

3.2.3. Time-Correlated Single Photon Counting

The FLS920 was also used for time-resolved measurements by the time-correlated single photon counting (TCSPC) technique with an instrument response of 2 ns, using a 444.2 nm diode laser (Edinburgh Instruments EPL- 445, 73 ps FWHM pulsewidth) operated at 200 kHz. A 495 nm long pass color filter was used for emission experiments. The global analysis of the time-resolved emission spectra was performed with the commercial package ReactLab KINETICS with the singular value decomposition and evolving-factor analysis functions.

3.2.4. Ultrafast Transient Absorption

The femtosecond transient absorption measurements were done using a pump-probe technique based on a Ti:Sapphire chirped pulse amplification (CPA) laser system (Clark-MXR CPA-2001). The 475 nm pump pulse (100 nJ) was produced by sum frequency generation of the 1230 nm output from the Optical Parametric Amplifier (OPA) and a portion of the 775 nm regenerative amplifier beam. The probe pulse was a white light continuum generated in a CaF_2 window. The pump and the probe polarizations were set to magic angle, and the two beams were focused to a 150 μm spot size spatially overlapped at the sample. The probe beam was then collected and directed into a fiber optic coupled multichannel spectrometer with a CMOS sensor. The pump beam was chopped at 500 Hz with a mechanical chopper synchronized to the laser, and pump-induced changes in the white light continuum were measured on a pulse-to-pulse basis. The instrument has a sensitivity of 1

mOD and is capable of measuring transient absorption spectra from 360 nm to 750 nm with a time resolution of approximately 250 fs.

3.2.5. Picosecond Transient Absorption

The pump-probe transient absorption measurements on the ps-μs time scale were accomplished using the same pump pulse as the femtosecond instrument. The probe pulse was generated by continuum generation in a diode-laser pumped photonic crystal fiber and electronically delayed relative to the pump pulse. The time resolution of the instrument is 500 ps dictated by the timing electronics.

3.3. RESULTS AND DISCUSSION

3.3.1. Steady-state Spectroscopy

The ground-state absorption spectra for the chromophores $[Ru_a^{II}]^{2+}$ and $[Ru_b^{II}]^{2+}$ in solution (Figure 3.3A) exhibit the typical singlet metal-to-ligand charge transfer (^{1}MLCT) band centered between 400 – 500 nm. The maximum absorbance of $[Ru_a^{II}]^{2+}$ (465 nm) is slightly red shifted in relation to the maximum absorbance of $[Ru_b^{II}]^{2+}$ (453 nm). From the normalized spectra it is obvious that the two chromophores have very different absorbance at the excitation wavelength (475 nm). The inner chromophore $[Ru_a^{II}]^{2+}$ has a relative absorbance of 58%. The proline systems loaded onto TiO_2 and ZrO_2 (Figures 3.3B and 3.3C) maintain the ^{1}MLCT ground-state absorbance between 400-500 nm.

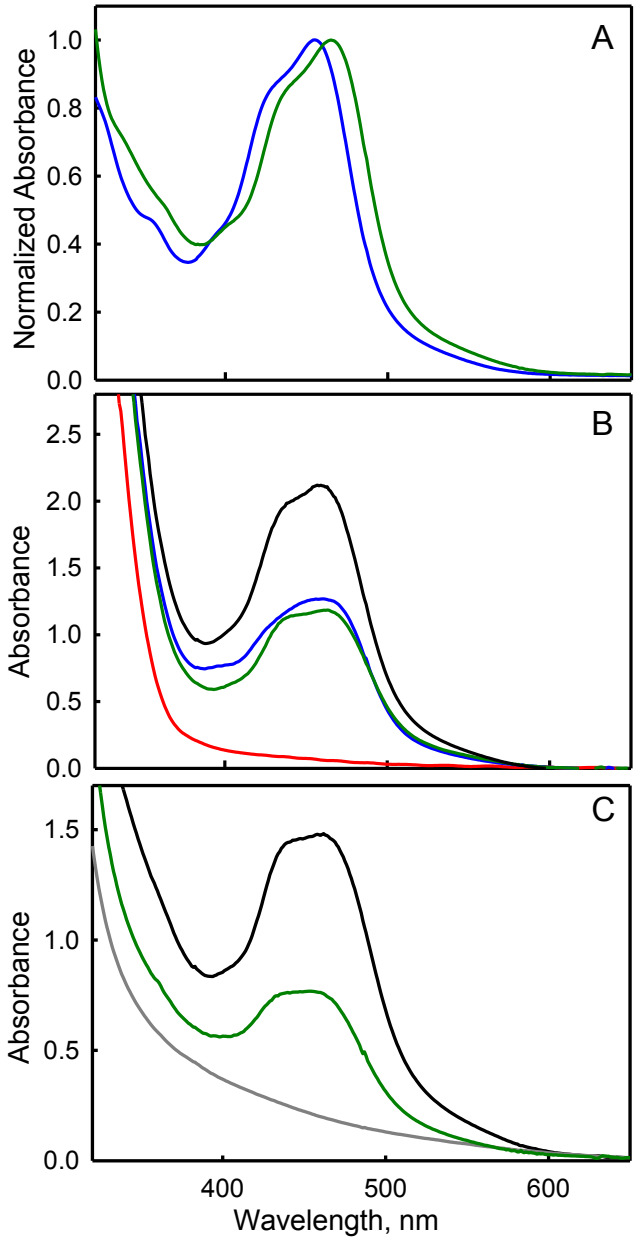

Figure 3.3. (A) Normalized ground state ultraviolet-visible spectra of the inner chromophore $[Ru_a^{II}]^{2+}$ (green) and outer chromophore $[Ru_b^{II}]^{2+}$ (blue) in 0.1 M $HClO_4$ pH 1 solution, 25 °C. (B) Ground state absorption spectra of TiO_2-$[Ru_a^{II}]^{2+}$ (green), TiO_2-$[Ru_a^{II}$-$Ru_b^{II}]^{4+}$ (black), TiO_2-$[Ru^{II}(bpy)_2(pbpy)]^{2+}$ (blue), and 3 μm thick TiO_2 (red). (C) Ground-state absorption of ZrO_2-$[Ru_a^{II}]^{2+}$ (green), ZrO_2-$[Ru_a^{II}$-$Ru_b^{II}]^{4+}$ (black), and 3 μm thick ZrO_2 (grey). Film samples were in quartz cuvette containing aqueous 0.1 M $HClO_4$ at 25 °C.

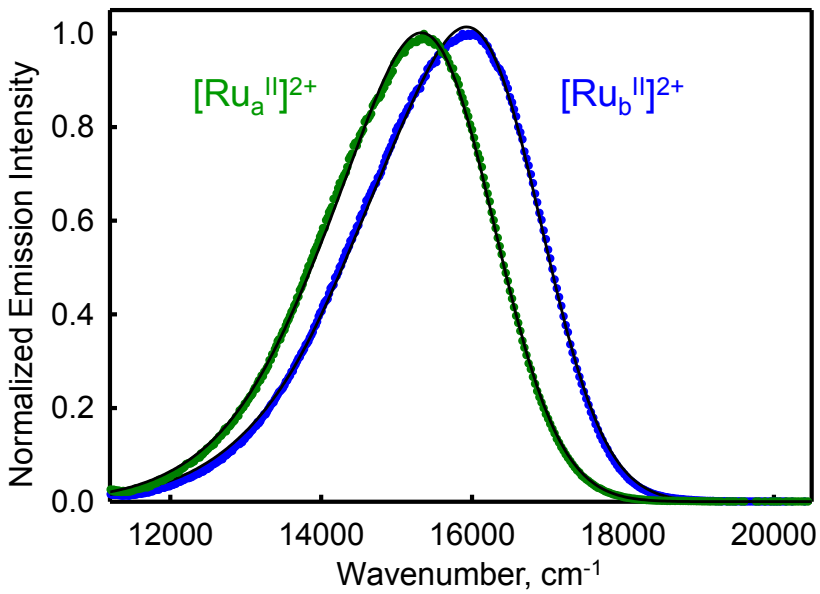

Figure 3.4. Steady-state emission spectra of the energy transfer donor or outer chromophore $[Ru_b^{II}]^{2+}$ (blue: 25 μM) and energy transfer acceptor or inner chromophore $[Ru_a^{II}]^{2+}$ (green: 25 μM) in 0.1 M $HClO_4$, pH 1 solution, 25°C. The excitation wavelength was 450 nm. Emission spectral fitting are shown black lines.

The steady-state emission (SSE) spectra of $[Ru_a^{II}]^{2+}$ and $[Ru_b^{II}]^{2+}$ in solution are shown in Figure 3.4. The emission is photoluminescence from the ^{3}MLCT excited-state after intersystem crossing from ^{1}MLCT occurs on the femtosecond time scale. The emission maximum of $[Ru_a^{II}]^{2+}$ is red shift by 15 nm relative to $[Ru_b^{II}]^{2+}$ due to stabilization of the Ru^{II} excited-state from the phosphonated bpy ligands in $[Ru_a^{II}]^{2+}$. The spectra were then fit using emission spectral fitting described in the data analysis section above. The results from the fits are $[Ru_b^{II}]^{2+}$: E_o = 16180 cm^{-1}, S = 0.690, and $\Delta\bar{\nu}_{0,1/2}$ = 1920 cm^{-1} and $[Ru_a^{II}]^{2+}$: E_o = 15520 cm^{-1}, S = 0.530, and $\Delta\bar{\nu}_{0,1/2}$ = 1980 cm^{-1}, where the error of the least squares fit is 5% but is limited by the 50 cm^{-1} resolution of the instrument. The results of the fit were then used with

Eq. 3.4 to calculate a driving force for energy transfer ($[Ru_a^{II}\text{-}Ru_b^{II}*]^{4+} \rightarrow [Ru_a^{II}*\text{-}Ru_b^{II}]^{4+}$) of $\Delta G = -0.07$ eV.

3.3.2. Energy Transfer Characterized by Time-resolved Emission Mapping

The energy transfer dynamics of $[Ru_a^{II}\text{-}Ru_b^{II}]^{4+}$ (Scheme 3.1, Eq. 2) were investigated by time-resolved emission measurements in aqueous 0.1 M $HClO_4$ at room temperature on the nanosecond timescale both in solution and on nanocrystalline ZrO_2 (where electron injection does not occur). As shown in Figure 3.5, excitation of $[Ru_a^{II}\text{-}Ru_b^{II}]^{4+}$ in solution and on ZrO_2 at 450 nm results in ^{3}MLCT emission with a time-dependent shift in the emission maximum from 630 to 645 nm. These observations are consistent with excitation of $[Ru_b^{II}]^{2+}$ (Scheme 3.1, Eq. 1a) followed by intra-assembly energy transfer to $[Ru_a^{II}]^{2+}$ (Scheme 3.1, Eq. 2), which is favored by 70 meV (Figure 3.3). Analysis of the time-dependent emission data by application of model free global analysis resulted in $\tau_{EnT} = 31$ ns in solution and $\tau_{EnT} = 33$ ns on ZrO_2 (Figures 3.6-3.7 and Tables 3.1-3.2). The comparable energy transfer rate constants in solution and on nanocrystalline ZrO_2 suggest that the secondary structure of the oligoproline assembly is retained on the surface of ZrO_2.

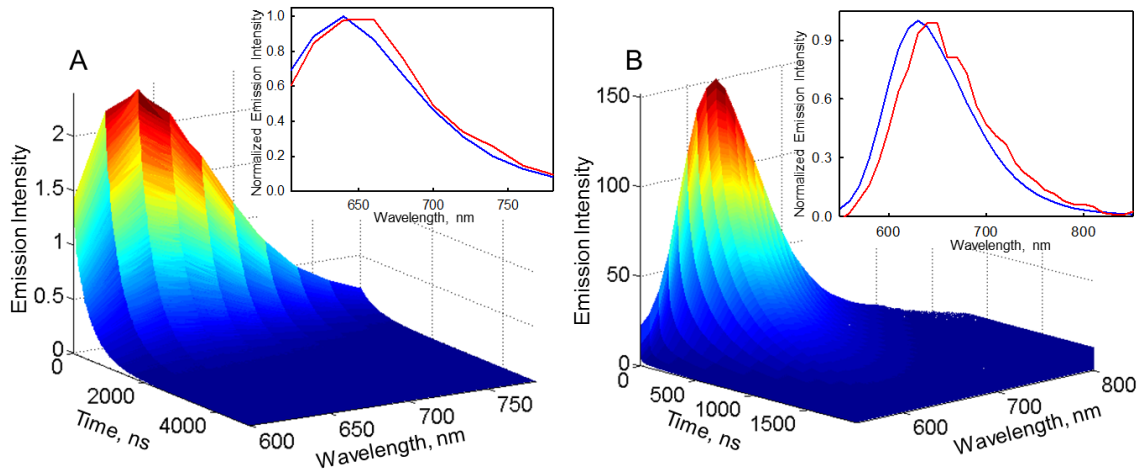

Figure 3.5. Time-resolved emission map of (A) $[Ru_a^{II}\text{-}Ru_b^{II}]^{4+}$ in aqueous 0.1 M $HClO_4$ and (B) $ZrO_2\text{-}[Ru_a^{II}\text{-}Ru_b^{II}]^{4+}$ on 3 μm thick ZrO_2 in aqueous 0.1 M $HClO_4$. The insets are spectra taken at early (blue: 5 ns) and late times (red: 1.7 μs). The red shift in the emission is evidence for energy transfer from chromophore $[Ru_b^{II}]^{2+}$ to chromophore $[Ru_a^{II}]^{2+}$.

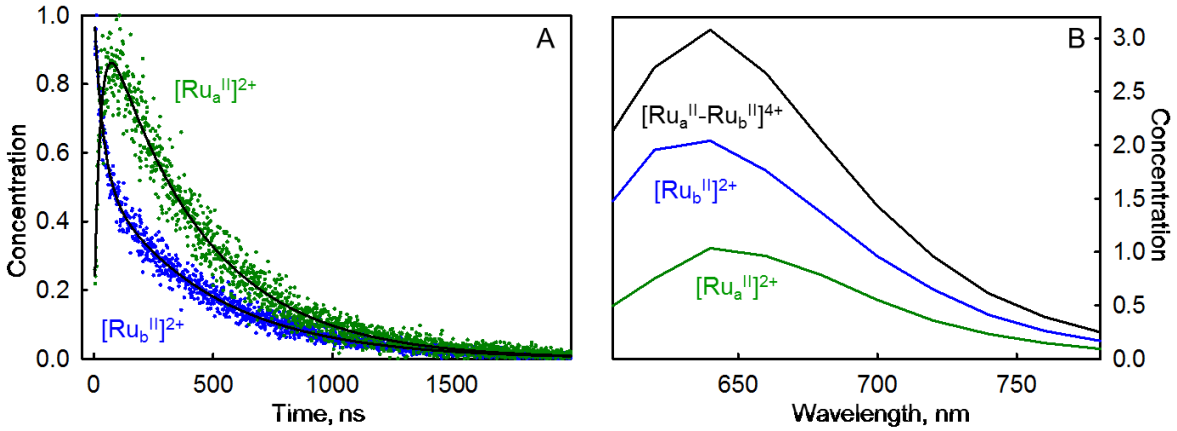

Figure 3.6. Global analysis results of $[Ru_a^{II}\text{-}Ru_b^{II}]^{4+}$ in aqueous 0.1 M $HClO_4$. (A) Plot of the evolution of the concentration of $[Ru_b^{II}]^{2+}$ (blue) and $[Ru_a^{II}]^{2+}$ (green). The biexponential fit to the curves is shown with black line and is summarized in Table 3.1. (B) The spectra of the concentration of the $[Ru_a^{II}\text{-}Ru_b^{II}]^{4+}$ (black), $[Ru_b^{II}]^{2+}$ (blue), and $[Ru_a^{II}]^{2+}$ (green).

Table 3.1. Fit results for the global analysis of $[Ru_a^{II}\text{-}Ru_b^{II}]^{4+}$ in aqueous 0.1 M $HClO_4$.

	A_1	k_1, x 10^6 s^{-1} (τ_1, ns)[a]	A_2	k_2, x 10^6 s^{-1} (τ_2, ns)[b]	Average τ (ns)
$[Ru_a^{II}]^{2+}$	0.48	0.39 (25.5)	0.52	0.024 (411)	31
$[Ru_b^{II}]^{2+}$	0.49	0.28 (36.4)	0.51	0.022 (465)	

[a]The fast component is a reflection of the energy transfer rate.

[b]The slow component is attributed to the excited state decay.

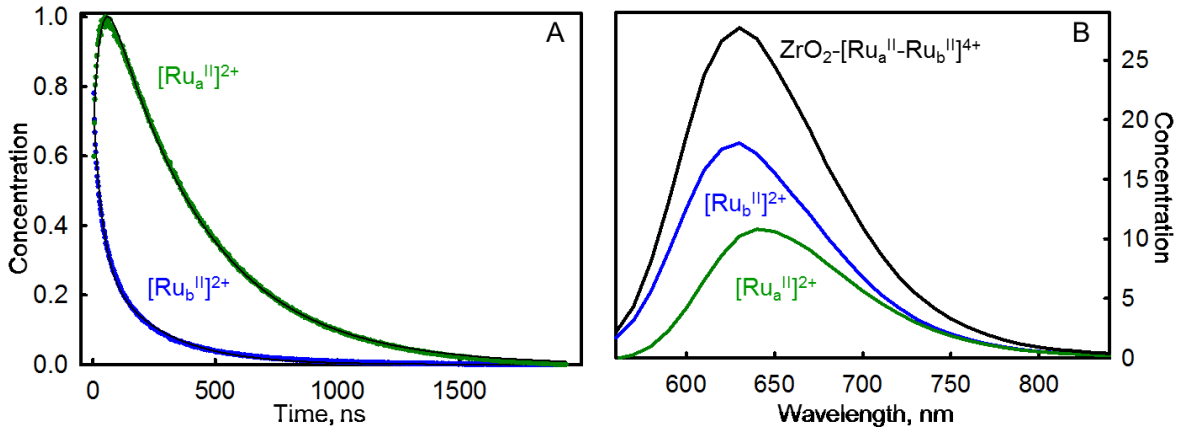

Figure 3.7. Global analysis results of ZrO_2-$[Ru_a^{II}\text{-}Ru_b^{II}]^{4+}$ in aqueous 0.1 M $HClO_4$. (A) Plot of the evolution of the concentration of $[Ru_b^{II}]^{2+}$ (blue) and $[Ru_a^{II}]^{2+}$ (green). The biexponential fit to the curves is shown with black line and is summarized in Table 3.2. (B) The spectra of the concentration of $[Ru_a^{II}\text{-}Ru_b^{II}]^{4+}$ (black), $[Ru_b^{II}]^{2+}$ (blue) and $[Ru_a^{II}]^{2+}$ (green).

Table 3.2. Fit results for the global analysis of ZrO_2-$[Ru_a^{II}\text{-}Ru_b^{II}]^{4+}$.

	A_1	k_1, x 10^6 s^{-1} (τ_1, ns)[a]	A_2	k_2, x 10^6 s^{-1} (τ_2, ns)[b]	Average τ (ns)
$[Ru_a^{II}]^{2+}$	0.33	0.34 (29.2)	0.67	0.025 (395)	33
$[Ru_b^{II}]^{2+}$	0.60	0.27 (36.8)	0.40	0.041 (244)	

[a]The fast component is a reflection of the energy transfer rate.

[b]The slow component is attributed to the excited state decay.

3.3.3. Ultrafast Electron Injection into TiO_2

Electron injection kinetics from TiO_2-$[Ru_a^{II}*]^{2+}$ and TiO_2-$[Ru_a^{II}*-Ru_b^{II}]^{4+}$ into nanocrystalline TiO_2 were measured by transient absorption spectroscopy. In transient absorption difference spectra, obtained 600 fs after excitation at 475 nm, Figure 3.8, characteristic $\pi\pi^*$ absorptions appear at 375 nm for the reduced polypyridyl ligand radical anion characteristic of the MLCT excited state, along with a prominent ground-state bleach of ^{1}MLCT absorption band of $[Ru_a^{II}]^{2+}$ and $[Ru_b^{II}]^{2+}$ at 450 nm. For TiO_2-$[Ru_a^{II}]^{2+}$ and TiO_2-$[Ru_a^{II}-Ru_b^{II}]^{4+}$ the transient absorption feature at 375 nm disappears rapidly (<1 ns) leaving behind the 450 nm bleach. These spectral changes are a clear signature of electron injection from the assembly into TiO_2. On longer time scales, 100's of ns, the bleach recovers, due to recombination by back electron transfer of the injected electron in TiO_2 with the oxidized chromophore on the surface.

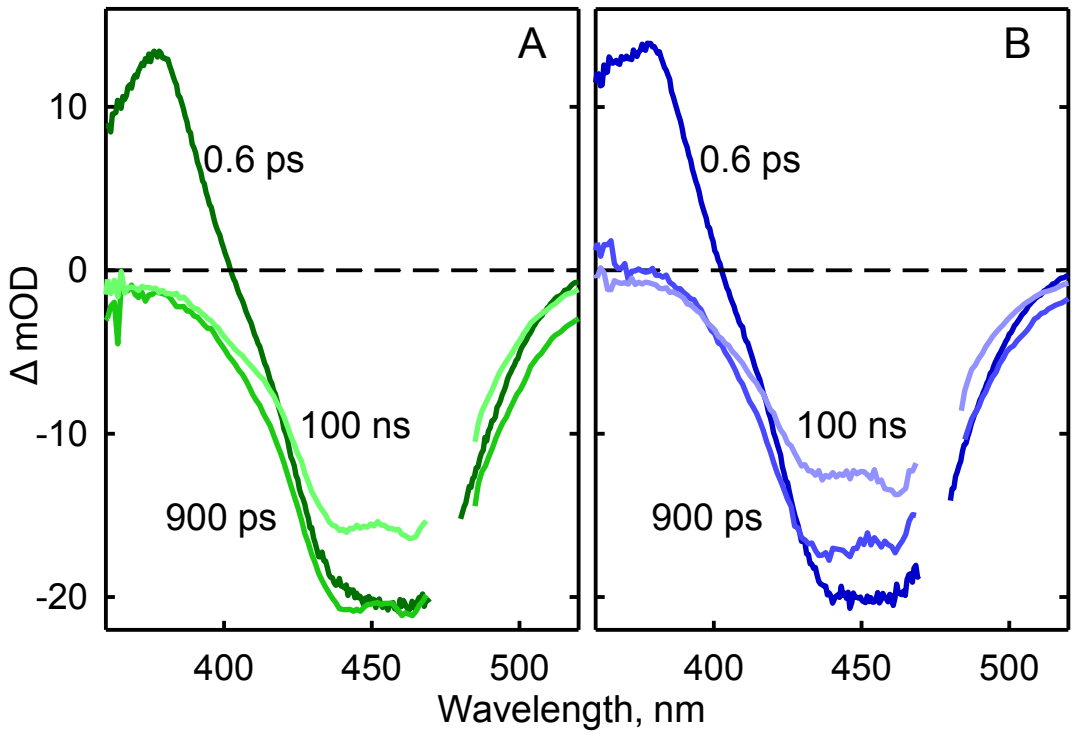

Figure 3.8. Transient absorption spectra of (A) TiO_2-$[Ru_a^{II}]^{2+}$ and (B) TiO_2-$[Ru_a^{II}$-$Ru_b^{II}]^{4+}$ at 0.6 ps (dark line), 900 ps (medium line), and 100 ns (light line) after laser excitation. Both samples were on 3 μm thick nanocrystalline TiO_2 film in aqueous 0.1 M HClO4 at 25 °C. The excitation wavelength was 475 nm.

The intensity of the transient absorption signal at 375 nm is shown as a function of pump-probe delay in Figure 3.4. For both TiO_2-$[Ru_a^{II}]^{2+}$ and TiO_2-$[Ru_a^{II}$-$Ru_b^{II}]^{4+}$ an initial decay in the absorbance occurs in the first 20 ps (Figure 3.9A), indicative of rapid electron injection of $[Ru_a^{II}*]^{2+}$ by the inner chromophore in TiO_2-$[Ru_a^{II}$-$Ru_b^{II}]^{4+}$ (Scheme 3.1, Eq. 1 followed by Eq. 3). There is a presumably sub-100 fs injection component that lies within the instrument response and is not detected here, but has been reported for similar systems.[25] The initial decay is followed by a slower decay which becomes a bleach feature on the 100 ps to 1 ns time scale. Although dominated by the excited state absorption at early times, the transient

absorption signal has contributions from positive going signal due to the appearance of excited state absorption and a negative going signal due to loss of ground state absorption, i.e. bleach. The approach to an overall negative signal at 375 nm reflects the presence of a small bleach contribution at this wavelength that becomes apparent as the excited state absorption band disappears due to injection.

Kinetic analysis of the time-dependent absorbance changes for TiO_2-$[Ru_a^{II}]^{2+}$ and TiO_2-$[Ru_a^{II}$-$Ru_b^{II}]^{4+}$ over this time range (Figure 3.9A) were fit to biexponential kinetics with τ_1 = 20 ps and τ_2 = 200 ps (Table 3.3) with the difference being in the amplitudes. We estimate an injection efficiency for assembly TiO_2-$[Ru_a^{II}]^{2+}$ to be 56% based on the amplitude of the 405 nm transient absorption at 1 ns.[18] The injection efficiency calculations were based on the literature precedent shown in Equation 3.5.

$$\Phi_{inj} = \frac{\left[\left(\frac{\Delta A_{sam}(\lambda_p)}{\Delta \varepsilon_{sam}(\lambda_p)}\right) / (1-10^{-A_{sam}(\lambda_{ex})})\right]}{\left[\left(\frac{\Delta A_{ref}(\lambda_p)}{\Delta \varepsilon_{ref}(\lambda_p)}\right) / (1-10^{-A_{ref}(\lambda_{ex})})\right]} \tag{3.5}$$

The $\Delta A(\lambda_p)$ is the amplitude of the 405 nm transient absorption probe signal at 1 ns for both the probe and the sample. The $\Delta\varepsilon(\lambda_p)$ is the change in the molar extinction coefficient at the probe wavelength from the ground to excited/oxidized state. Finally, A is the absorbance at the excitation wavelength. The reference species for this calculation was chosen to be $[Ru^{II}(bpy)_2(pbpy)]^{2+}$ on nanocrystalline TiO_2 that has 100% electron injection.[18]

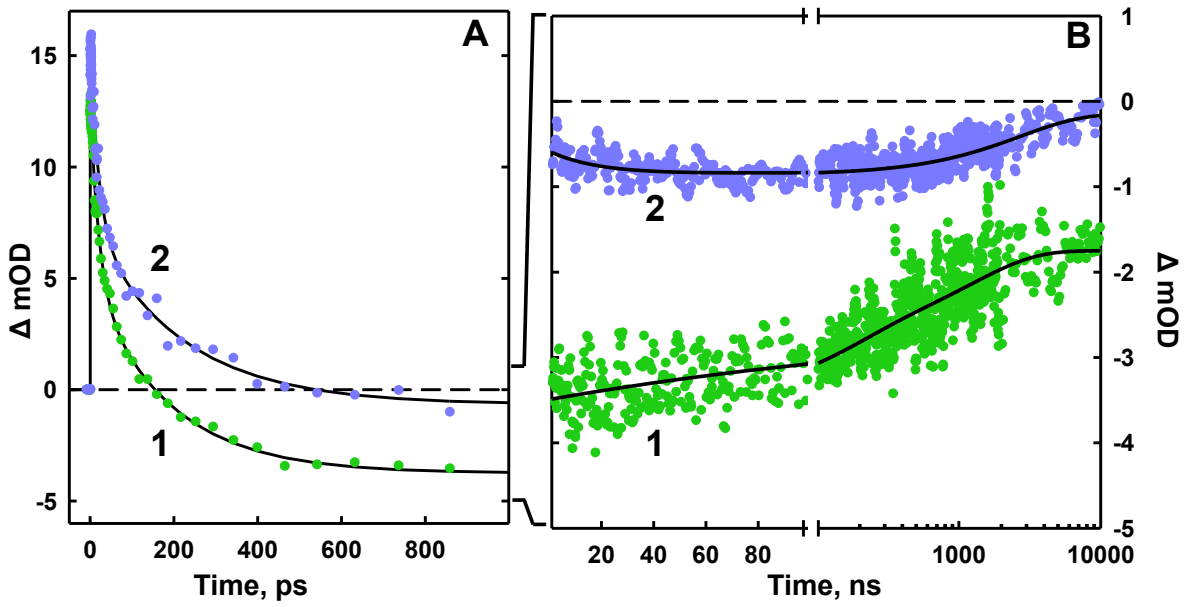

Figure 3.9. Transient absorption kinetics and fits of the ππ* absorption (375 nm ± 3 nm) for TiO_2-$[Ru_a^{II}]^{2+}$ (green) and TiO_2-$[Ru_a^{II}$-$Ru_b^{II}]^{4+}$ (blue) in (A) the first 1000 ps and (B) 1 to 10,000 ns after excitation at 475 nm. The fits are shown in black lines and summarized in Tables 3.3 and 3.4. All samples were on 3 μm thick nanocrystalline TiO_2 film in aqueous 0.1 M $HClO_4$ solution at 25 °C.

After 1 ns (Figure 3.9B), TiO_2-$[Ru_a^{II}]^{2+}$ decays by complex non-exponential kinetics over a period of several microseconds as found for TiO_2-$[Ru^{II}(bpy)_2(pbpy)]^{2+}$.[18] This is consistent with slow back electron transfer process (Scheme 3.1, Eq. 5). Assembly TiO_2-$[Ru_a^{II}$-$Ru_b^{II}]^{4+}$, on the other hand, shows a continued decrease in the amplitude of the excited state absorption band over the next 100 ns, followed by a slow decay back to zero. Kinetic analysis of the data by multiexponential fit resulted in τ = 20 ns for the growth of a negative signal (Table 3.4).

Table 3.3. Fit results for TiO_2-$[Ru_a^{II}]^{2+}$ and TiO_2-$[Ru_a^{II}$-$Ru_b^{II}]^{4+}$ for the electron injection (375 nm) for the first 1 ns.

Complex	Offset	A_1	k_1, x 10^8 s^{-1} (τ_1)	A_2	k_2, x 10^8 s^{-1} (τ_2)
TiO_2-$[Ru_a^{II}]^{2+}$	-3.8 ± 0.2	8.1 ± 0.6	488 ± 43 (21 ps ± 2)	8.7 ±0.5	54 ± 6 (185 ps ±22)
TiO_2-$[Ru_a^{II}$-$Ru_b^{II}]^{4+}$	-0.7 ± 0.4	8.0 ± 0.8	498 ± 68 (20 ps ± 3)	8.1 ±0.7	47 ± 9 (215 ps ±43)

Table 3.4. Fit results for TiO_2-$[Ru_a^{II}]^{2+}$ and TiO_2-$[Ru_a^{II}$-$Ru_b^{II}]^{4+}$ for the electron injection (375 nm) for 1 ns to 10 μs.

Complex	Offset	A_1	k_1, x 10^6 s^{-1} (τ_1)	A_2	k_2, x 10^4 s^{-1} (τ_2)
TiO_2-$[Ru_a^{II}]^{2+}$	-1.75 ± 0.05	0.73 ± 0.11	6.4 ± 1.4 (157 ns ± 35)	1.01 ± 0.11	0.78 ± 0.15 (1.3 μs ± 0.25)
TiO_2-$[Ru_a^{II}$-$Ru_b^{II}]^{4+}$	-0.15 ± 0.34	0.28 ± 0.04	53.4 ± 12.1 (**18.7 ns ± 4.2**)	0.71 ± 0.03	0.36 ± 0.04 (2.8 μs ± 0.27)

The continued loss of excited state absorption in TiO_2-$[Ru_a^{II}$-$Ru_b^{II}]^{4+}$ is indicative of delayed injection into TiO_2 that occurs with a 20 ns time constant. We attribute this delayed injection to excitation of the outer chromophore $[Ru_b^{II}]^{2+}$, which then takes one of two pathways. Following excitation, $[Ru_b^{II}]^{2+}$ can inject remotely (Scheme 3.1, Eq. 3a), or undergo energy transfer to $[Ru_a^{II}]^{2+}$ (Scheme 3.1, Eq. 2) followed by fast electron injection (Scheme 3.1, Eq. 3b). Given the similarity in time scale for loss of excited state absorption in TiO_2-$[Ru_a^{II}$-$Ru_b^{II}]^{4+}$ (20 ns) and intra-assembly energy transfer in ZrO_2-$[Ru_a^{II}$-$Ru_b^{II}]^{4+}$ (~30 ns), we ascribe the delayed injection to the latter. In either case, these results point to high efficiency, ≈ 96%, energy transfer/electron injection based on the relative lifetimes for

excited state decay ($\tau \approx 490$ ns) and energy transfer/injection, and imply an injection efficiency for TiO_2-$[Ru_a^{II}$-$Ru_b^{II}]^{4+}$ of 54%. Therefore, TiO_2-$[Ru_a^{II}$-$Ru_b^{II}]^{4+}$ is an efficient antenna for interfacial sensitization by energy transfer.

3.3.4. Back Electron Transfer

The rates of back electron transfer are reflected in the decay of the ground state bleach transient absorption signal at 450 nm (Figure 3.10). The back electron transfer kinetics for TiO_2-$[Ru_a^{II}]^{2+}$ and TiO_2-$[Ru_a^{II}$-$Ru_b^{II}]^{4+}$ exhibit multiexponential behavior due to the variety of back electron migration pathways in TiO_2, as shown previously for TiO_2-$[Ru^{II}(bpy)_2(pbpy)]^{2+}$ under the same conditions.[18] The average lifetime for recovery of the bleach at 450 nm, $\langle\tau\rangle$, are 19 μs and 11 μs for assemblies TiO_2-$[Ru_a^{II}]^{2+}$ and TiO_2-$[Ru_a^{II}$-$Ru_b^{II}]^{4+}$ compared to 17 μs for TiO_2-$[Ru^{II}(bpy)_2(pbpy)]^{2+}$ (Table 3.5).[18] While the average back electron transfer time exceeds a microsecond, there is 20 ns component in TiO_2-$[Ru_a^{II}$-$Ru_b^{II}]^{4+}$ resulting presumably from direct excitation of $[Ru_a^{II}]^{2+}$ (Scheme 3.1, Eq. 1b) that occurs along with the slower injection arising from excitation of $[Ru_b^{II}]^{2+}$ (Table 3.5). This 20 ns back electron transfer component makes it problematic to draw quantitative conclusions regarding injection efficiencies from the amplitudes of the kinetic components.

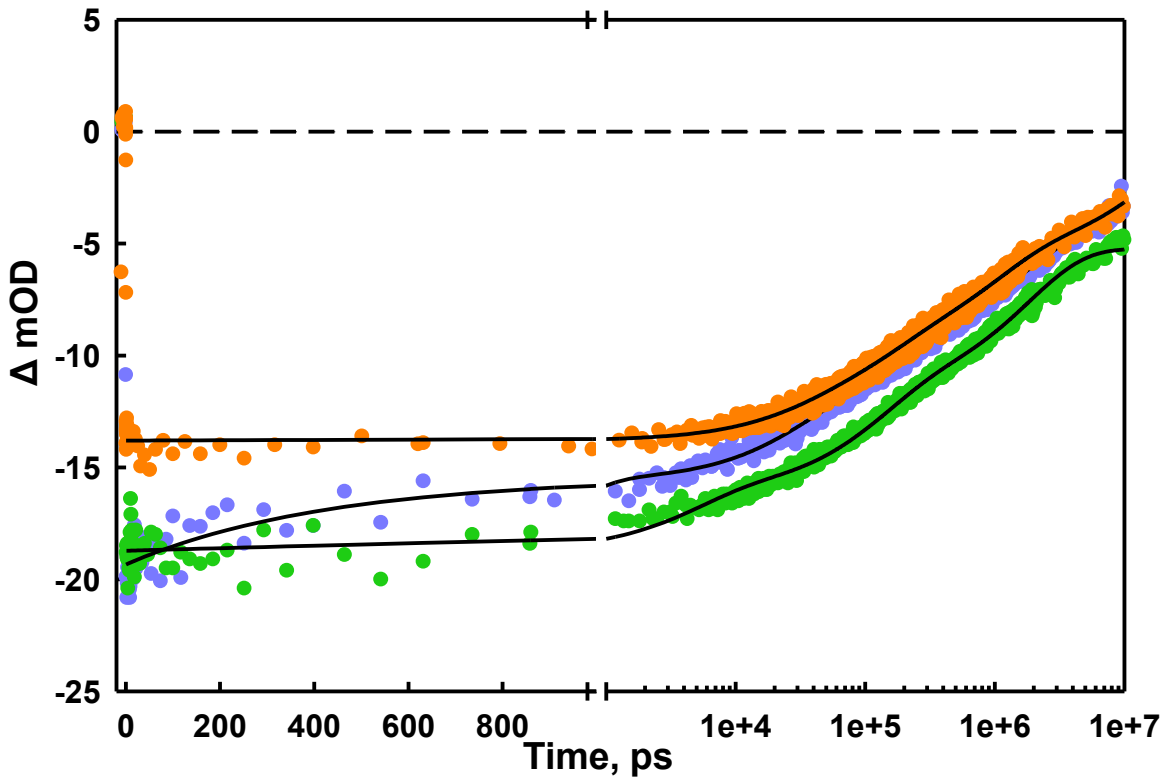

Figure 3.10. Transient absorption kinetics and fits for the ground state bleach (collected at 450 nm ± 3 nm) of TiO_2-$[Ru_a^{II}]^{2+}$ (green), TiO_2-$[Ru_a^{II}$-$Ru_b^{II}]^{4+}$ (blue), and TiO_2-$[Ru^{II}(bpy)_2(pbpy)]^{2+}$ (orange) in aqueous 0.1 M $HClO_4$ at 25 °C. The fits are shown with solid black line and summarized in Table 3.5. The excitation wavelength was 475 nm.

Table 3.5. Fit results TiO_2-$[Ru_a^{II}]^{2+}$ and TiO_2-$[Ru_a^{II}$-$Ru_b^{II}]^{4+}$ for back electron transfer (450 nm) from 1 ns to 10 μs.

	TiO_2-$[Ru_a^{II}]^{2+}$	TiO_2-$[Ru_a^{II}$-$Ru_b^{II}]^{4+}$	TiO_2-$[Ru^{II}(bpy)_2(pbpy)]^{2+}$
A_1	-2.3 ± 0.1	-4.0 ± 0.1	-1.2 ± 0.3
k_1, x 10^6 s^{-1} (τ_1)	320 ± 27 (3.1 ns ± 0.3)	1980 ± 142 (5.1 ps ± 0.4)	36 ± 8.8 (28 ns ± 7)
A_2	-3.8 ± 0.1	-3.6 ± 0.1	-2.8 ± 0.2
k_2, x 10^6 s^{-1} (τ_2)	11.7 ± 0.5 (86 ns ± 4)	22 ± 1 (45 ns ± 2)	7.8 ± 1.3 (128 ns ± 22)
A_3	-4.9 ± 0.1	-4.7 ± 0.1	-4.3 ± 0.2
k_3, x 10^6 s^{-1} (τ_3)	± 0.1 (870 ns ± 47)	1.9 ± 0.1 (518 ± 22)	1.1 ± 0.1 (950 ns ± 92)
A_4	-7.7 ± 0.1	-7.0 ± 0.1	-5.5 ± 0.2
k_4, x 10^6 s^{-1} (τ_3)	0.05 ± 0.01 (19 μs ± 1)	0.09 ± 0.01 (11 μs ± 1)	0.06 ± 0.01 (18 μs ± 2)
$\langle\tau\rangle$[a]	19 μs ± 1	11 μs ± 1	17 μs ± 1

[a]Average lifetimes are calculated using the equation $\langle\tau\rangle = \sum A_i\tau_i^2 / \sum A_i\tau_i$.[18]

3.4. CONCLUSIONS

Our results are notable in introducing a new, modular approach to the synthesis of pre-organized and highly tunable assemblies for interfacial molecular energy conversion using solid phase peptide synthesis coupled with 'click' chemistry. We have demonstrated that such scaffolds maintain their secondary structure in solution and on surfaces as well as provide the necessary arrangement of chromophores for directional energy transfer followed by electron injection into TiO_2. We are currently synthesizing a family of multichromophoric

oligoprolines to explore the distance dependence of intra-assembly electron and energy transfer. Additionally chromophore-catalyst assemblies are being investigated for applications in dye sensitized photoelectrosynthesis cells.

REFERENCES

(1) Ferreira, K. N.; Iverson, T. M.; Maghlaoui, K.; Barber, J.; Iwata, S. *Science*, 2004, *303*, 1831-1838.

(2) Gagliardi, C. J.; Vannucci, A. K.; Concepcion, J. J.; Chen, Z.; Amadelli, T.J. *Energy Environ. Sci.,* 2012, 5, 7704-7717.

(3) Kümin, M.; Sonntag, L.-S.; Wennemers, H. *J. Am. Chem. Soc.* 2007, *129*, 466-467.

(4) Mozer, A. J.; Griffith, M. J.; Tsekouras, G.; Wagner, P.; Wallace, G. G.; Mori, S.; Sunahara, K.; Miyashita, M.; Earles, J. C.; Gordon, K. C.; Du, L.; Katoh, R.; Furube, A.; Officer, D. L. *J. Am. Chem. Soc.* 2009, *131*, 15621-15623. Uetomo, A.; Kozaki, M.; Suzuki, S.; Yamanaka, K.; Ito, O.; Okada, K. *J. Am. Chem. Soc.* 2011, *133*, 13276-13279.

(5) Fang, Z.; Eshbaugh, A. A.; Schanze, K. S. *J. Am. Chem. Soc.* 2011, *133*, 3063-3069. Liu, Y.; Summers, M. A.; Edder, C.; Fréchet, J. M. J.; McGehee, M. D. *Adv. Mater.* 2005, *17*, 2960-2964. Kim, Y.-G.; Walker, J.; Samuelson, L. A.; Kumar, J. *Nano Lett.* 2003, *3*, 523-525. Wang, L.; Puodziukynaite, E.; Vary, R. P.; Grumstrup, E. M.; Walczak, R. M.; Zolotarskaya, O. Y.; Schanze, K. S.; Reynolds, J. R.; Papanikolas, J. M. *J. Phys. Chem. Lett.* 2012, *3*, 2453-2457.

(6) Dutta, P. K.; Varghese, R.; Nangreave, J.; Lin, S.; Yan, H.; Liu, Y. *J. Am. Chem. Soc.* 2011, *133*, 11985-11993. Garo, F.; Häner, R. *Angew. Chem. Int. Ed.* 2012, *51*, 916-919.

(7) Gilat, S. L.; Adronov, A.; Fréchet, J. M. J. *Angew. Chem. Int. Ed.* 1999, *38*, 1422-1427. Hasobe, T.; Kashiwagi, Y.; Absalom, M. A.; Sly, J.; Hosomizu, K.; Crossley, M. J.; Imahori, H.; Kamat, P. V.; Fukuzumi, S. *Adv. Mater.* 2004, *16*, 975-979.

(8) Lee, C. Y.; Farha, O. K.; Hong, B. J.; Sarjeant, A. A.; Nguyen, S. T.; Hupp, J. T. *J. Am. Chem. Soc.* 2011, *133*, 15858-15861. Kent, C. A.; Liu, D.; Ma, L.; Papanikolas, J. M.; Meyer, T. J.; Lin, W. *J. Am. Chem. Soc.* 2011, *133*, 12940-12943.

(9) Hu, K.; Robson, K. C. D.; Johansson, P. G.; Berlinguette, C. P.; Meyer, G. J. *J Am. Chem. Soc.* 2012, *134*, 8352-8355. Huang, Z.; Geletii, Y. V.; Musaev, D. G.; Hill, C. L.; Lian, T. *Ind. Eng. Chem. Res.* 2012, 51, 11850-11859.

(10) O'Regan, B.; Grätzel, M. *Nature* 1991, *353*, 737-740.

(11) Song, W.; Chen, Z.; Brennaman, M. K.; Concepcion, J. J.; Patrocinio, A. O. T.; Murakami Iha, N. Y.; Meyer, T. J. *Pure Appl. Chem.* 2011, 83, 749-768.

(12) O'Regan, B.; Gratzel, M. *Nature.* 1991, 353, 737-740. Amadelli, R.; Argazzi, R.; Bignozzi, C. A.; Scandola, F. *J. Am. Chem. Soc.* 1990, 112, 7099-7103. Parussulo, A. L. A.; Iglesias, B. A.; Toma, H. E.; Araki, K. *Chem Commun*. 2012, 48, 6939-6941. Kleverlaan, C.; Alebbi, M.; Argazzi, R.; Bignozzi, C. A.; Hasselmann, G. M.; Meyer, G. J. *Inorg. Chem*. 2000, 39, 1342-1343.

(13) Deber, C. M.; Bovey, F. A.; Carver, J. P. Blout, E. R. *J. Am. Chem. Soc.* 1970, *92*, 6191-6198.

(14) Serron, S. A.; Aldridge, W. S; Fleming, C. N.; Danell, R. M.; Baik, M.-H.; Sykora, M.; Dattelbaum, D. M.; Meyer, T. J. *J. Am. Chem. Soc.* 2004, *126*, 14506-14514. Striplin, D. R.; Reece, S. Y.; McCafferty, D. G.; Wall, C. G.; Friesen, D. A.; Erickson, B. W.; Meyer, T. J. *J. Am. Chem. Soc.* 2004, *126*, 5282-5291.

(15) Springer, J. W.; Parkes-Loach, P. S.; Reddy, K. R.; Krayer, M.; Jiao, J.; Lee, G. M.; Niedzwiedzki, D. M.; Harris, M. A.; Kirmaier, C.; Bocian, D. F.; Lindsey, J. S.; Holten, D.; Loach, P. A. *J. Am. Chem. Soc.* 2012, *134*, 4589-4599. Channon, K. J.; Devlin, G. L.;

MacPhee, C. E. *J. Am. Chem. Soc.* 2009, *131*, 12520-12521. Hong, J.; Kharenko, O. A.; Ogawa, M. Y. *Inorg. Chem.* 2006, *45*, 9974-9984. Knorr, A.; Galoppini, E.; Fox, M. A. *J. Phys. Org. Chem.* 1997, 10, 484-498. Wilger, D. J.; Bettis, S. E.; Materese, C. K.; Minakova, M.; Papoian, G. A.; Papanikolas, J. M.; Waters, M. L. *Inorg. Chem.* 2012, *51*, 11324-11338. Hanson, K.; Wilger, D.; Jones, S. T.; Harrision, D. P.; Bettis, S. E.; Luo, H.; Papanikolas, J. M.; Waters, M. L.; Meyer, T. J. *Biopolymers.* 2013, 100, 25-37.

(16) Ma, D.; Bettis, S. E., Hanson, K.; Minakova, M.; Alibabaei, L.; Fondrie, W.; Ryan, D. M.; Papoian, G. A.; Meyer, T.J.; Papanikolas, J. M.; Waters, M. L. *J. Am. Chem. Soc*., 2013, 135, 5250–5253.

(17) Hanson, K.; Brennaman, M. K.; Luo, H.; Glasson, C. R. K.; Concepcion, J. J.; Song, W.; Meyer, T. J. *ACS Appl. Mater. Interfaces* 2012, *4*, 1462-1469.

(18) Hanson, K.; Brennaman, M. K.; Ito, A.; Luo, H.; Song, W.; Parker, K. A.; Ghosh, R.; Norris, M. R.; Glasson, C. R. K.; Concepcion, J. J.; Lopez, R.; Meyer, T. J. *J. Phys. Chem. C.* 2012, 116, 14837-14847. (19) Gallagher, L. A.; Serron, S. A.; Wen, X.; Hornstein, B. J.; Dattelbaum, D. M.; Schoonover, J. R.; Meyer, T. J. Inorg. Chem. 2005, 44, 2089−2097.

(20) Knight, T. E.; Goldstein, A. P.; Brennaman, K.; Cardolaccia, T.; Pandya, A., Desimone, J. M.; Meyer, T. J. *J. Phys. Chem. B* 2001, 115, 64-70.

(21) Meylemans, H. A.; Lel, C.; Damrauer, N. H. *Inorganic Chemistry.* 2008, 47, 4060-4076.

(22) Murtaza, Z.; Graff, D. K.; Zipp, A. P.; Wori, L. A.; Jones, Jr, W. E.; Bates, W. D.; Meyer, T. J. *J. Phys. Chem.* 1994, 98, 10504-10513.

(23) Caspar, J. V.; Meyer, T. J. *J. Am. Chem. Soc.* 1983, 105, 5583-5590.

(24) Graff, D; Claude, J. P.; Meyer, T. J. *Electron Transfer Reactions: Inorganic Organometallic and Biological Applications* American Chemical Society, Washington DC, 1997, vol. 253, pp. 183-198.

(25) Asbury, J. B.; Ellingson, R. J.; Ghosh, H. N.; Ferrere, S.; Nozik, A. J.; Lian, T. J. Phys. Chem. B. 1999, 103, 3110-3119.

CHAPTER 4. PHOTOPHYSICAL CHARACTERIZATION OF A HELICAL PEPTIDE CHROMOPHORE-WATER OXIDATION CATALYST ASSEMBLY ON A SEMICONDUCTOR SURFACE USING ULTRAFAST SPECTROSCOPY[3]

[3]This chapter has been submitted for publication as an article in the Journal of Physical Chemistry C.

4.1. INTRODUCTION

Dye sensitized photoelectrosynthesis cells (DSPECs) provide a promising strategy for using sunlight to drive the conversion of water and carbon dioxide into chemical fuels.[1-2] Integral to the DSPEC approach is integration of molecular components for harvesting light, separating redox equivalents, and using them to drive the solar fuels half reactions. The functional elements have been demonstrated separately but examples where all three have been integrated are rare.[3-7] Described within is the use of ultrafast spectroscopy to characterize the initial photo-activation step in a molecular assembly that couples a light-harvesting chromophore and water oxidation catalyst.

Water oxidation requires the transfer of four electrons and four protons with O-O bond formation in a net reaction, $2H_2O \rightarrow O_2 + 4H^+$.[1] Significant progress has been made in the development of polypyridyl-based Ru(II)-aqua catalysts for water oxidation with mechanistic details established both in solution and on oxide surfaces (Scheme 4.1).[8-10] The initial activation step involves oxidation of $[Ru^{II}\text{-}OH_2]^{2+}$ to $[Ru^{III}\text{-}OH_2]^{3+}$ followed by proton loss to give $[Ru^{III}\text{-}OH]^{2+}$ above the pK_a of the coordinated water. Further oxidation results in e^-/H^+ loss to give $[Ru^{IV}{=}O]^{2+}$. Transfer of the 3rd oxidative equivalent yields $[Ru^{V}{=}O]^{3+}$. It is active toward water oxidation by O—O bond formation and proton loss to give $[Ru^{III}\text{-}OOH]^{2+}$ in what is typically the rate limiting step. Transfer of the 4th oxidative equivalent occurs with H^+ loss to give $[Ru^{IV}\text{-}OO]^{2+}$, where O_2 replaced water H_2O in a reductive substitution step to regenerate the initial catalyst $[Ru^{II}\text{–}OH_2]^{2+}$.

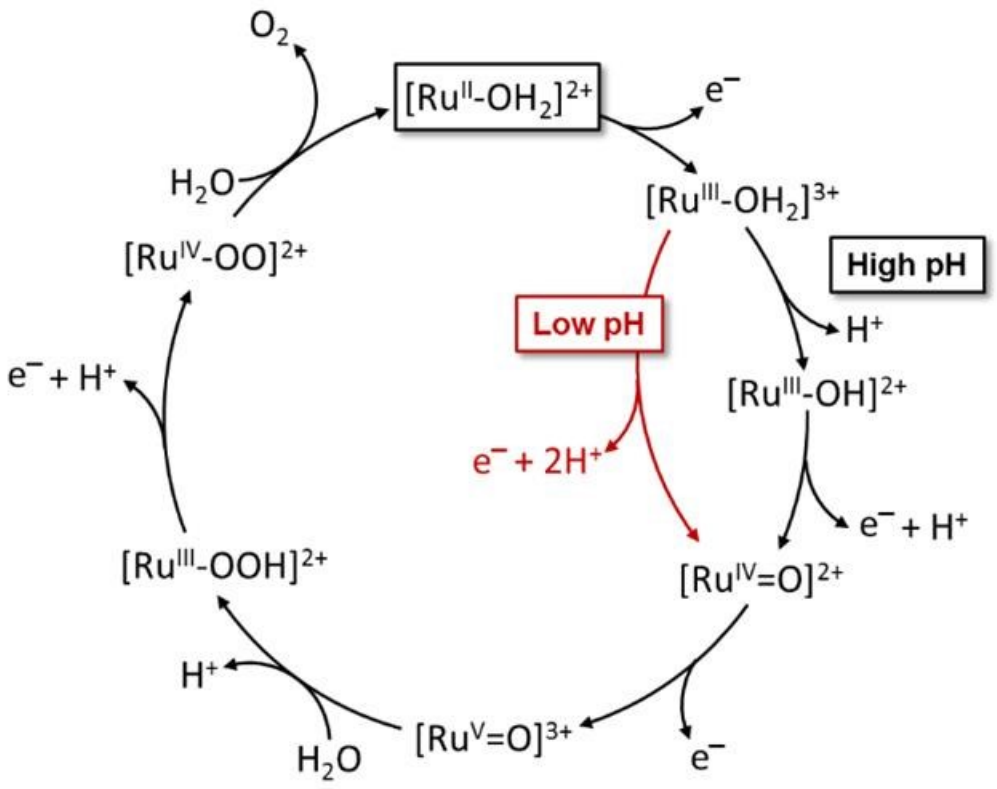

Scheme 4.1. Illustration of the water oxidation catalytic cycle for single-site Ru^{II} catalysts.

The DSPEC approach marries the excitation, electron transfer, catalyst activation steps in surface–bound chromophore-catalyst assemblies with the interfacial and electron transport properties of high band gap oxide semiconductors. A variety of chemical approaches have explored the design of chromophore-catalyst assemblies, but most require a unique synthetic approach for each new assembly.[4-7] In contrast, peptide scaffolds offer a flexible design motif since step-by-step synthesis techniques can be used to control primary sequence and secondary structure as a way to control electron transfer flow and rates. In a previous report we described an assembly consisting of two Ru^{II} complexes positioned along an oligoproline chain.[11] The double-chromophore assembly was anchored by chemical

binding to TiO_2, and intra-assembly energy transfer and electron injection were characterized by ultrafast spectroscopic methods.

This chpater extends that work to a functioning molecular assembly for water oxidation, TiO_2-$[Ru_a^{II}$-Ru_b^{II}-$OH_2]^{4+}$. It consists of a light-harvesting chromophore ($[Ru_a^{II}]^{2+}$ = $[Ru(pbpy)_2(L)]^{2+}$ (pbpy = 4,4′-$(PO_3H_2)_2$-2,2′-bipyridine, L = 4′-methyl-(2,2′-bipyridine)-4-propargyl amide)) and water oxidation catalyst ($[Ru_b^{II}$-$OH_2]^{2+}$ = $[Ru(Mebimpy)(L)OH_2]^{2+}$ (Mebimpy = 2,6-bis(1-methylbenzimidazol-2-yl)pyridine)) linked by a six-residue oligoproline scaffold, Figure 4.1. The chromophore is placed on the *N*-terminal residue (i), and the water oxidation catalyst on the fourth proline residue (i+3).[12] In aqueous solution the peptide chain adopts a left-handed PPII helical structure with 3 residues per turn bringing the chromophore and catalyst on adjacent turns into close spatial proximity. Molecular dynamics simulations on the double-chromophore system gave a Ru-Ru inter-unit spacing of 13 Å suggesting that the two complexes are close contact.[11]

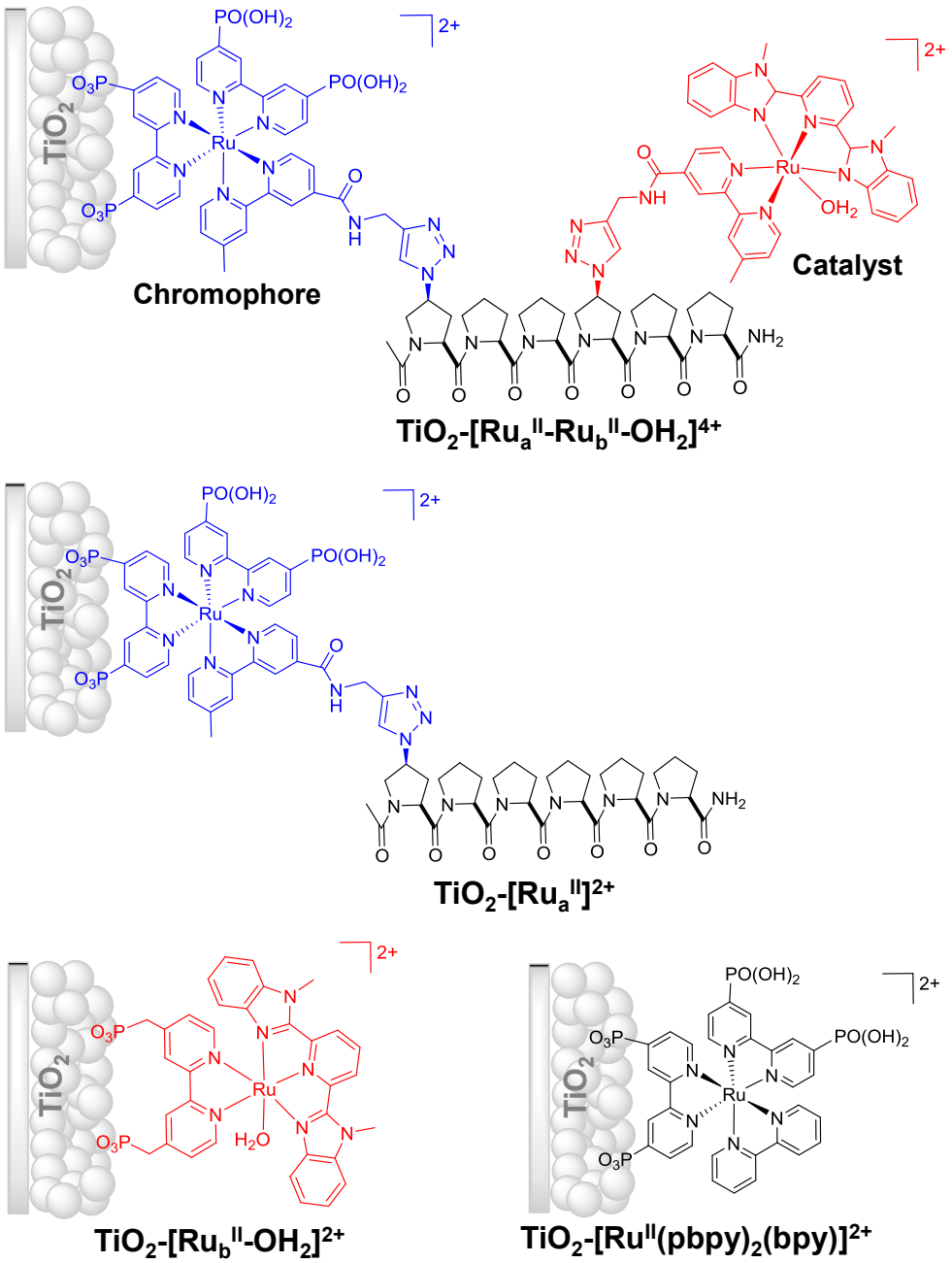

Figure 4.1. Illustration of the molecular structures of the assembly $[Ru_a^{II}\text{-}Ru_b^{II}\text{-}OH_2]^{4+}$, chromophore $[Ru_a^{II}]^{2+}$, catalyst $[Ru_b^{II}\text{-}OH_2]^{2+}$ and control chromophore $[Ru^{II}(pbpy)_2(bpy)]^{2+}$on nanocrystalline TiO_2.

This work focuses on the use of ultrafast spectroscopy to characterize the initial photoactivation step of this chromophore-catalyst assembly. Photoexcitation of the assembly

on TiO_2, TiO_2-$[Ru_a^{II}$-Ru_b^{II}-$OH_2]^{4+}$, results in either excitation of the chromophore (Scheme 4.2, Eq. 1a), or the catalyst (Eq. 1b). Chromophore excitation is followed by efficient electron injection, TiO_2-$[Ru_a^{II}*$-Ru_b^{II}-$OH_2]^{4+} \rightarrow TiO_2(e^-)$-$[Ru_a^{III}$-$Ru_b^{II}$-$OH_2]^{5+}$ (Eq. 4), resulting in the formation of oxidized chromophore at the surface. Once formed, transfer of the oxidative equivalent to the catalyst occurs by intra-assembly electron transfer, $TiO_2(e^-)$-$[Ru_a^{III}$-Ru_b^{II}-$OH_2]^{5+} \rightarrow TiO_2(e^-)$-$[Ru_a^{II}$-$Ru_b^{III}$-$OH_2]^{5+}$ (Eq. 5), completing the first of four steps in the water oxidation catalytic cycle. Energy transfer from photoexcited chromophore to the catalyst, TiO_2-$[Ru_a^{II}*$-Ru_b^{II}-$OH_2]^{4+} \rightarrow TiO_2$-$[Ru_a^{II}$-$Ru_b^{II}*$-$OH_2]^{4+}$ (Eq. 3) is also possible, and a potentially deleterious energy loss pathway, however it is significantly slower than electron injection and does not interfere with injection.

Following injection, "recombination" by back electron transfer from the semiconductor surface, $TiO_2(e^-)$-$[Ru_a^{II}$-Ru_b^{III}-$OH_2]^{5+} \rightarrow TiO_2$-$[Ru_a^{II}$-$Ru_b^{II}$-$OH_2]^{4+}$ (Eq. 6b) returns the surface assembly to its initial state with the transiently stored oxidative equivalent lost as heat. Successful utilization of the interfacial injection/electron transfer schemes requires long recombination times or rapid removal of injected electrons from the semiconductor, both of which are being pursued experimentally.

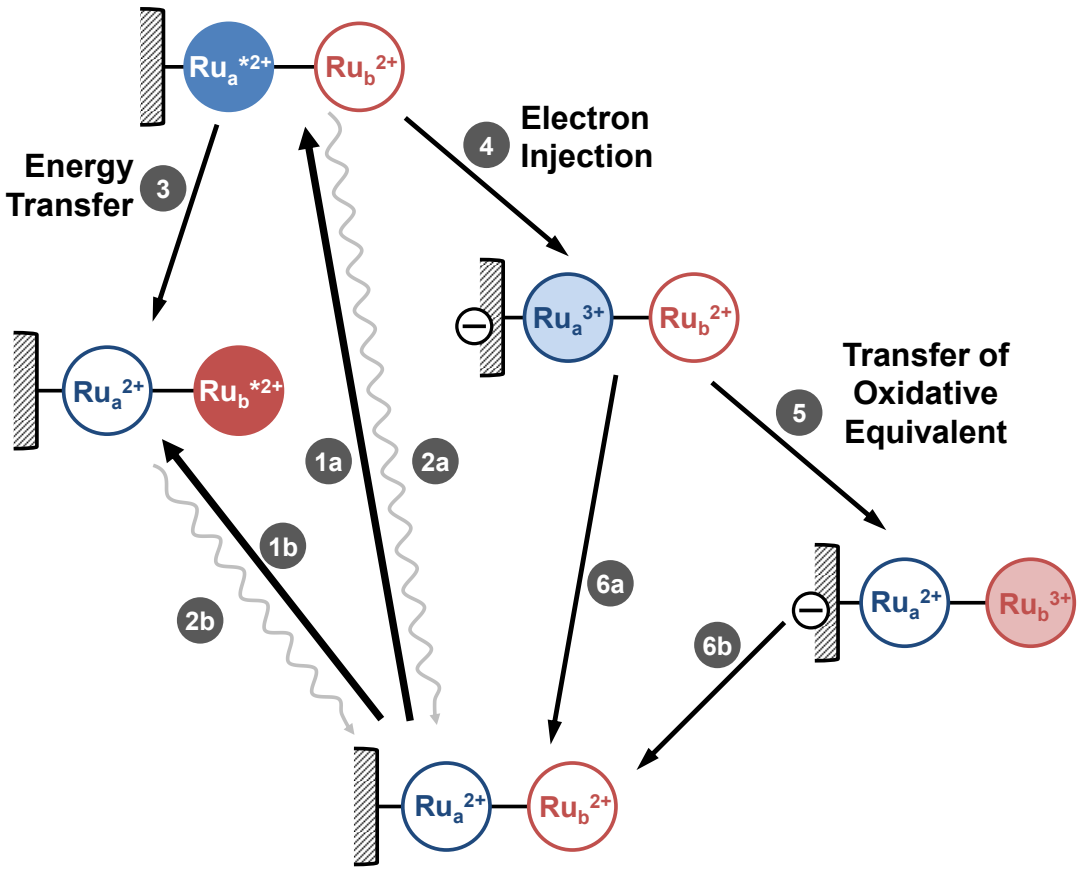

Scheme 4.2. Schematic representation of the events in TiO_2-[Ru_a^{II}-Ru_b^{II}-OH_2]$^{4+}$ upon photoexcitation.

4.2. EXPERIMENTAL SECTION

4.2.1. Sample Preparation

The synthesis and structural characterization of the [Ru_a^{II}]$^{2+}$ and [Ru_a^{II}-Ru_b^{II}-OH_2]$^{4+}$ oligoproline peptides was performed by Dr. Derek Ryan in Dr. Waters' research group. All samples were loaded onto nanocrystalline films of TiO_2 (1 μm thick) and ZrO_2 (3 μm thick) by soaking overnight in a 150 mM aqueous 0.1 M $HClO_4$ solution. The surface coverage for [Ru_a^{II}]$^{2+}$ and [Ru_a^{II}-Ru_b^{II}-OH_2]$^{4+}$ is nearly full with $\Gamma = 2.2 \times 10^{-8}$ mol/cm^2/μm and 1.7×10^{-8} mol/cm^2/μm respectively on TiO_2 and $\Gamma = 2.2 \times 10^{-8}$ mol/cm^2/μm and 1.5×10^{-8} mol/cm^2/μm respectively on ZrO_2.[13] The films were placed in a 1.0 cm cuvette at 45 degree angle from the

incident laser beam. All samples were in 0.1 M $HClO_4$ and purged with Argon for >45 minutes just prior to data collection.

4.2.2. Steady-state Techniques

Ground-state absorbance measurements were conducted with a Hewlett Packard 8453 UV-VIS-NIR absorption spectrophotometer. Steady-state emission (SSE) data were collected using an Edinburgh Instruments FLS920 equipped with a 450 W Xenon lamp and photomultiplier tube (Hamamatsu 2658P). SSE data were collected using a bandwidth no larger than 4.0 nm and, once collected, were corrected for the emission spectrophotometer's spectral response.

4.2.3. Time-resolved Emission

The FLS920 was also used for time-resolved measurements by the time-correlated single photon counting (TCSPC) technique with an instrument response of 2 ns, using a 444.2 nm diode laser (Edinburgh Instruments EPL- 445, 73 ps FWHM pulse width) operated at 200 kHz. A 495 nm long pass color filter was used for emission experiments.

4.2.4. Ultrafast Transient Absorption

Femtosecond transient absorption measurements were done using a pump-probe technique based on a 1 kHz Ti:Sapphire chirped pulse amplifier (Clark-MXR CPA-2001). The 420 nm pump pulse (100 nJ) was produced by sum frequency generation of 900 nm, the frequency doubled output from an Optical Parametric Amplifier (OPA), and a portion of the 775 nm regenerative amplifier beam. A white light continuum generated in a CaF_2 window was used as a probe pulse. The pump and probe polarizations were set to magic angle, and the two beams were focused to 150 μm spot size spatially overlapped at the sample. The probe beam was then collected and directed into a fiber optic coupled multichannel

spectrometer with a CMOS sensor. The pump beam was chopped at 500 Hz with a mechanical chopper synchronized to the laser, and pump-induced changes in the white light continuum were measured on a pulse-to-pulse basis. The instrument has a sensitivity of 1 mOD, and is capable of measuring transient absorption spectra from 360 nm to 750 nm with a time resolution of approximately 250 fs.

4.2.5. Picosecond Transient Absorption

Pump-probe transient absorption measurements on the ps-µs time scale were accomplished using the same pump pulse as the femtosecond instrument, but the probe pulse was generated by continuum generation in a diode-laser pumped photonic crystal fiber and electronically delayed relative to the pump pulse. The time resolution of the instrument is 500 ps dictated primarily by the timing electronics.

4.3. RESULTS AND DISCUSSION

Transient absorption spectroscopy, on time scales ranging from sub-picosecond to hundreds of microseconds, was used to characterize the initial photoactivation step in the water oxidation cycle of a chromophore-catalyst assembly anchored to TiO_2. In the sub-sections that follow the dynamical processes involved in the initial photo-activation step are described.

4.3.1. Photoexcitation

Ground-state absorption spectra for the chromophore $[Ru_a^{II}]^{2+}$ and the catalyst $[Ru_b^{II}\text{-}OH_2]^{2+}$ anchored to TiO_2 and ZrO_2 are shown in Figure 4.2. Both complexes in the assembly exhibit singlet metal-to-ligand charge transfer (^{1}MLCT) bands centered between 400-500 nm, which is typical of Ru(II) polypyridyl complexes (Figure 4.2).[14] The absorption

maximum for the catalyst (495 nm) appears at lower energy compared to the chromophore (465 nm), in large part due to greater π conjugation in the Mebimpy ligand.

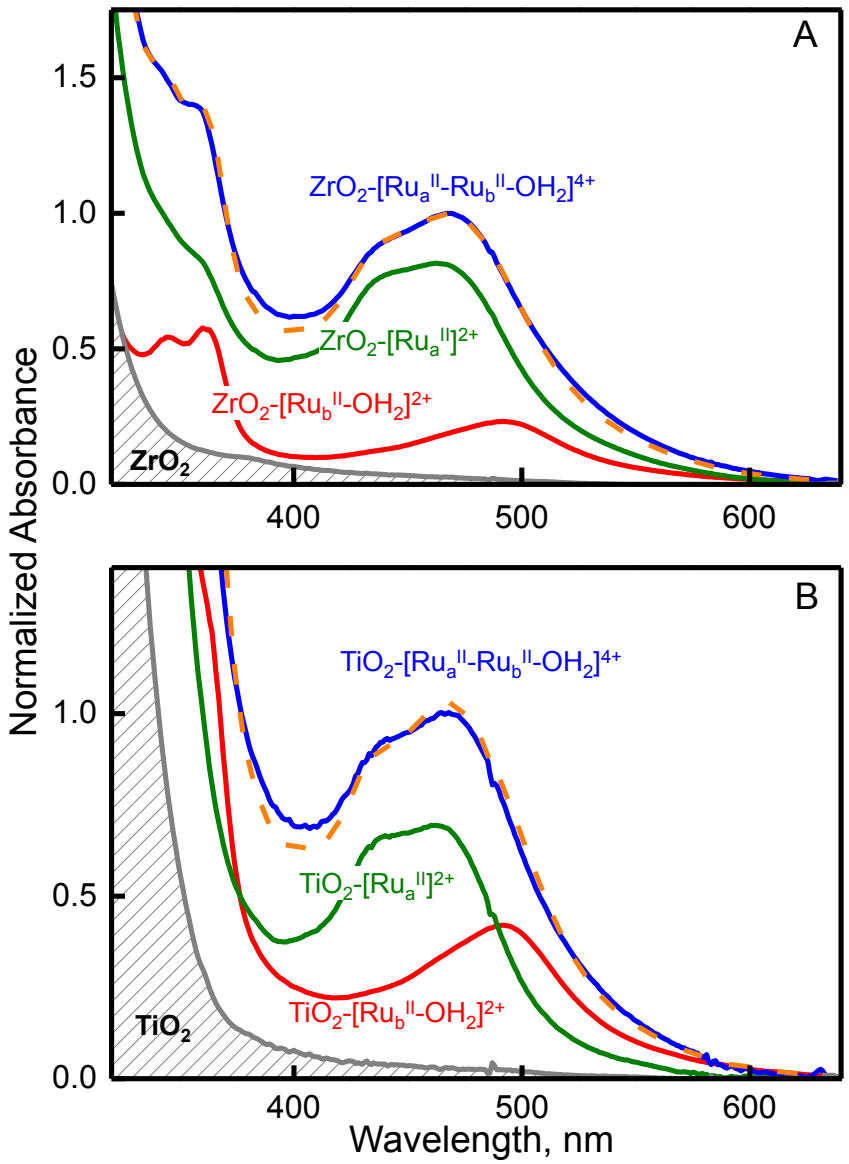

Figure 4.2. (A) Ground-state absorption of 3 μm ZrO_2 (grey), ZrO_2-$[Ru_a^{II}]^{2+}$ (green), ZrO_2-$[Ru_b^{II}$-$OH_2]^{2+}$ (red), ZrO_2-$[Ru_a^{II}$-Ru_b^{II}-$OH_2]^{4+}$ (blue), and sum of ZrO_2-$[Ru_a^{II}]^{2+}$ and ZrO_2-$[Ru_b^{II}$-$OH_2]^{2+}$ (dashed). (B) Ground-state absorption for1 μm TiO_2 film (black), TiO_2-$[Ru_a^{II}]^{2+}$ (green), TiO_2-$[Ru_b^{II}$-$OH_2]^{2+}$ (red), TiO_2-$[Ru_a^{II}$-Ru_b^{II}-$OH_2]^{4+}$ (blue), and the sum of TiO_2-$[Ru_a^{II}]^{2+}$ and TiO_2-$[Ru_b^{II}$-$OH_2]^{2+}$ (dashed). All film samples were in quartz cuvette containing aqueous 0.1 M $HClO_4$, 25 °C.

The ground-state absorption at centered 470 nm of the assembly on ZrO_2 (ZrO_2-$[Ru_a^{II}$-Ru_b^{II}-$OH_2]^{4+}$) is the superposition of absorption spectra for the chromophore (ZrO_2-$[Ru_a^{II}]^{2+}$) and model catalyst (ZrO_2-$[Ru_b^{II}$-$OH_2]^{2+}$), consistent with weak interactions and essentially electronically isolated chromophores. The intensity of the catalyst absorption in the assembly on ZrO_2 is ~3.5 times smaller than the chromophore at their respective maxima while the ratio of molar extinction coefficients, $\varepsilon_{[Rua]}/\varepsilon_{[Rub]}$, is only 1.3 times smaller. The apparent decrease is consistent with samples partly converted to the Ru(IV) peroxide form of the assembly, $[Ru_a^{II}$-$Ru_b^{IV}(OO)]^{4+}$. On both ZrO_2 and TiO_2 equilibria are set up on the surfaces between the two forms, ZrO_2-$[Ru_a^{II}$-Ru_b^{II}-$OH_2]^{4+}$ + O_2 ⇄ ZrO_2-$[Ru_a^{II}$-$Ru_b^{II}(OO)]^{4+}$ + H_2O, with the underlying details currently under investigation.

On the ZrO_2-loaded slide, ~40% of the assembly sites were converted into the weakly absorbing peroxide forms, $[Ru_b^{IV}$-$OO]^{2+}$, as assessed by ground-state absorption measurements. In the photophysical measurements, the peroxide forms behave dynamically as isolated ($[Ru_a^{II}*]^{2+}$) sites without noticeable perturbation or participation by the peroxide sites $[Ru_b^{II}(OO)^{2+}]$. A similar conversion occurs on TiO_2 films, but the extent of conversion to the peroxide depends on conditions and, in those samples, spectral comparisons show that ~20% of the catalysts were converted to the peroxide for the samples used. Since the Ru(IV) peroxide form in assemblies is only weakly absorbing in the visible, is not further oxidized by the chromophore, and is not involved in the photophysical properties of the assembly, it is spectator to the photophysics studied here.

Because of the large degree of overlap in the absorption spectra, between chromophore and catalyst in $[Ru_a^{II}$-Ru_b^{II}-$OH_2]^{4+}$, selective excitation of the chromophore is not possible. Based on the relative intensities of the component ground-state spectra on TiO_2,

we estimate that at 420 nm, the excitation wavelength used in this work, 85% of the photons are absorbed by the chromophore and 15% by the catalyst.

4.3.2. Electron Injection

Transient absorption spectra observed 1 ps after photoexcitation for both TiO_2-$[Ru_a^{II}]^{2+}$ and TiO_2-$[Ru_a^{II}$-Ru_b^{II}-$OH_2]^{4+}$ are depicted in Figure 4.3. Both show excited-state absorptions at 380 nm and to the red of 500 nm that arise primarily from $\pi \rightarrow \pi^*$ transitions on the polypyridyl radical anion of the excited-state, as well as, the ground-state bleach centered at 450 nm. The decay of the excited-state absorptions, which occur without loss of the ground-state bleach (Figure 4.3A), are a direct signature of electron injection from excited-state ($[Ru_a^{II*}]^{2+}$) into TiO_2 (Scheme 4.2, Eq. 4).

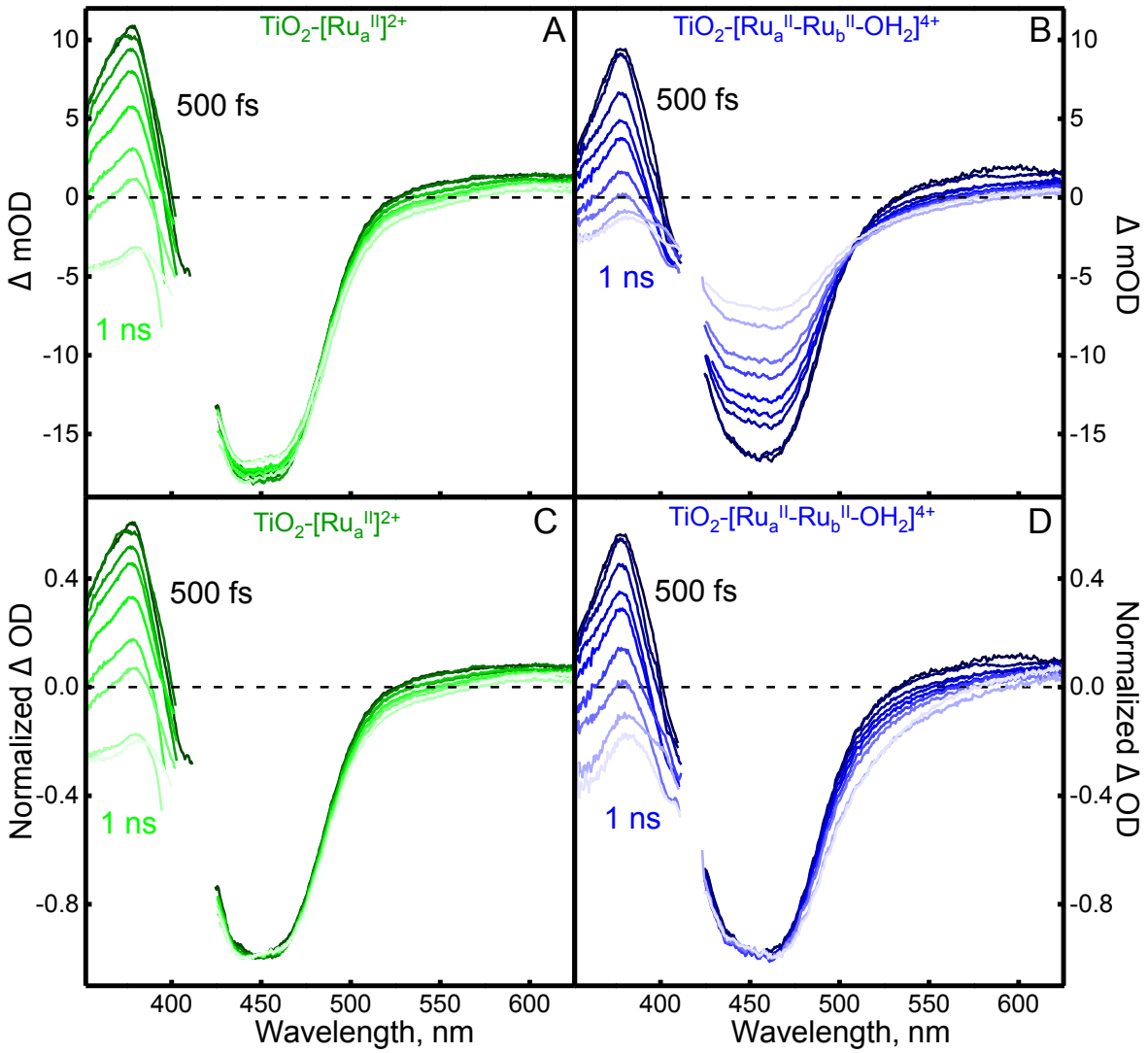

Figure 4.3. Transient absorption spectra of (A) TiO_2-$[Ru_a^{II}]^{2+}$ and (B) TiO_2-$[Ru_a^{II}$-Ru_b^{II}-$OH_2]^{4+}$, and normalized (C) TiO_2-$[Ru_a^{II}]^{2+}$ and (D) TiO_2-$[Ru_a^{II}$-Ru_b^{II}-$OH_2]^{4+}$ at 500 fs (dark line), 1 ps, 5 ps, 10 ps, 20 ps, 50 ps, 100 ps, 500 ps, and 1 ns (light line) after laser excitation. Both samples were on 1 μm thick nanocrystalline TiO_2 films in aqueous 0.1 M $HClO_4$ at 25 °C. The excitation wavelength was 420 nm.

The rate of electron injection was determined by monitoring the decay of the 380 nm absorption as a function of pump-probe delay, Figure 4.4A. The decay is multiexponential, with both fast ($k = 5.18 \times 10^{10}$ s^{-1}; $\tau = 19$ ps) and slow ($k = 5.0 \times 10^{9}$ s^{-1}; $\tau = 200$ ps)

components. In addition to these slower components, there is most likely a sub-100 fs component that falls within our instrument response and, as a consequence is not detected, but has been observed in related complexes.[15]

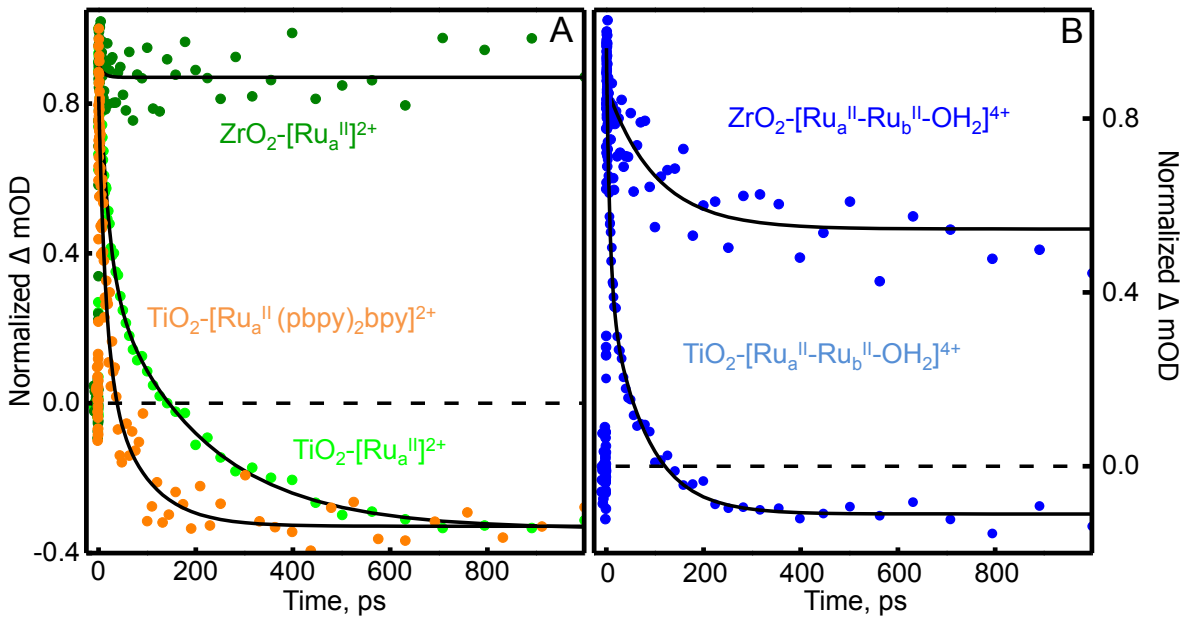

Figure 4.4. Electron injection kinetics monitored at 380 nm for (A) TiO_2-$[Ru_a^{II}]^{2+}$ (light green), ZrO_2-$[Ru_a^{II}]^{2+}$ (dark green), TiO_2-$[Ru^{II}(pbpy)_2(bpy)]^{2+}$ (orange) (B) TiO_2-$[Ru_a^{II}$-Ru_b^{II}-$OH_2]^{4+}$ (light blue) and ZrO_2-$[Ru_a^{II}$-Ru_b^{II}-$OH_2]^{4+}$ (dark blue). The fits are shown in black and parameters are summarized in Table 4.1. The films were immersed in aqueous 0.1 M $HClO_4$ at 25 °C. The excitation wavelength was 420 nm.

Table 4.1. Summary of fit for electron injection kinetics at 380 nm of $[Ru_a^{II}]^{2+}$, $[Ru_a^{II}\text{-}Ru_b^{II}\text{-}OH_2]^{4+}$, and $[Ru^{II}(pbpy)_2(bpy)]^{2+}$ on TiO_2 and ZrO_2.

	A_1	τ_1	A_2	τ_2	Offset
TiO_2-$[Ru_a^{II}]^{2+}$	0.59 ± 0.31	19.3 ± 1.5	0.69 ± 0.03	201.7 ± 18.5	-0.34 ± 0.14
ZrO_2-$[Ru_a^{II}]^{2+}$	0.03 ± 0.02	9.7 ± 17.6	--	--	0.87 ± 0.12
TiO_2-$[Ru^{II}(pbpy)_2(bpy)]^{2+}$	0.71 ± 0.20	14.3 ± 4.3	0.46 ± 0.20	77.5 ± 36.1	-0.33 ± .02
TiO_2-$[Ru_a^{II}\text{-}Ru_b^{II}\text{-}OH_2]^{4+}$	0.57 ± 0.02	6.85 ± 0.55	0.53 ± 0.02	77.10 ± 6.44	-0.11 ± 0.07
ZrO_2-$[Ru_a^{II}\text{-}Ru_b^{II}\text{-}OH_2]^{4+}$	0.33 ± 0.02	101.3 ± 23.7	--	--	0.55 ± 0.02

The distribution of injection rates most likely arises from a combination of factors. Following excitation, the initially formed ^{1}MLCT state, or vibrationally hot triplet states, undergo rapid injection. Injection from thermally equilibrated ^{3}MLCT states occurs on time scales ranging from sub-ps to tens of picoseconds.[16-17] The physical origin of the slower injection components is unclear. Injection from TiO_2-$[Ru^{II}(pbpy)_2(bpy)]^{2+}$ (with an amide functionalized ligand replacing bipyridine, Figure 4.1) is significantly faster than TiO_2-$[Ru_a^{II}]^{2+}$, indicating that the slow components arise from the presence of the amide functional group on the third ligand (Figure 4.4). Excitation results in partitioning of the photoexcitation amongst the three ligands, which gives rise to three distinct excited-states corresponding to placement of the charge on each of the three ligands. The difference in substituents lifts the degeneracy of the three ligands, and if the lowest energy ligand is not bound to the surface, then injection would either occur remotely,[18-19] or by inter-ligand excitation transfer to the bound ligand followed by injection.[20] Experiments currently underway on a family of related

complexes suggest that ligand stabilization is responsible for injection components on the picosecond timescale.

The efficiency of electron injection for TiO_2-$[Ru_a^{II}]^{2+}$ is estimated from the transient absorption spectra on TiO_2 and ZrO_2 to be 72%, with 9% occurring in the first 500 fs after photoexcitation (Figure 4.5). Since similar phosphonated chromophores exhibit injection efficiencies approaching unity,[13] the low efficiency observed for this chromophore is most likely due to the slow injection.

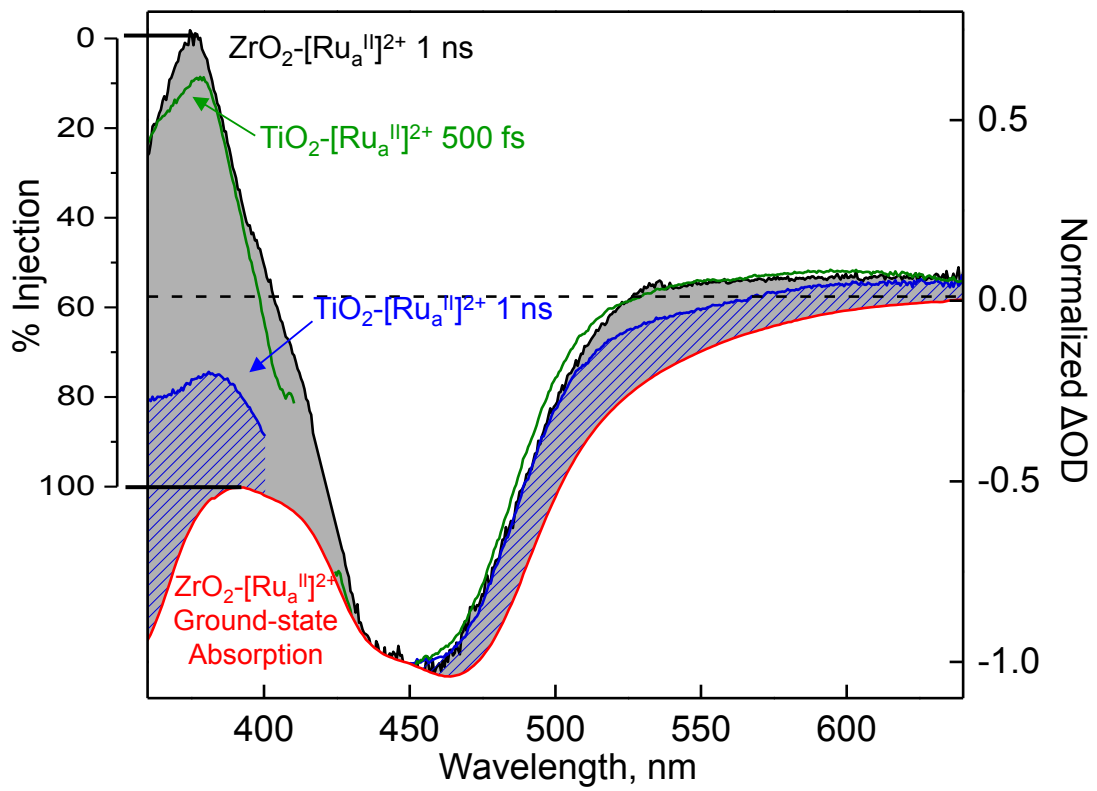

Figure 4.5. The electron injection efficiency for TiO_2-$[Ru_a^{II}]^{2+}$ is calculated from the ratio of the difference between the transient absorption intensity at 380 nm of $[Ru_a^{II}]^{2+}$ on TiO_2 (blue) and ZrO_2 (black) at 1 ns and the difference between intensity of ZrO_2 at 1 ns (black) and the inverse of the ground state absorption on ZrO_2 (red) at 380 nm. The electron injection efficiency for TiO_2-Ru_a^{II} is 72%. The 9% ultrafast injection is seen in the ratio between ZrO_2-$[Ru_a^{II}]^{2+}$ (black) and TiO_2-$[Ru_a^{II}]^{2+}$ at 500 fs (green).

4.3.3. Energy Transfer

The photoexcited chromophore can also be deactivated by energy transfer to the catalyst and is observable on ZrO_2 in the absence of injection. Steady-state emission for ZrO_2-$[Ru_a^{II}]^{2+}$ (centered at 640 nm) and ZrO_2-$[Ru_b^{II}OH_2]^{2+}$ (centered at 700 nm) arise from ^{3}MLCT emission following fast intersystem crossing from initially excited ^{1}MLCT (Figure 4.6A). Emission from ZrO_2-$[Ru_a^{II}$-Ru_b^{II}-$OH_2]^{4+}$ (centered at 665 nm) is quenched and broadened to the red relative to ZrO_2-$[Ru_a^{II}]^{2+}$ due to energy transfer from $[Ru_a^{II}*]^{2+}$ to $[Ru_b^{II}$-$OH_2]^{2+}$ (Scheme 4.2, Eq. 3). Because the rate of energy transfer ($k = 4.8 \times 10^7\ s^{-1}$, $\tau = 21$ ns), measured by time-resolved emission quenching (Figure 4.6B), is much faster than the excited state lifetime of the chromophore (450 ns), the efficiency of energy transfer on ZrO_2 is ≈ 95%. The emission quantum yield for the catalyst is least 100 times less than emission from the chromophore, based on the relative lifetimes of the two complexes. As a result, emission from the assembly on ZrO_2 arises primarily from the ≈ 5% of unquenched chromophores that do not undergo energy transfer as shown by an emission spectrum that resembles the chromophore emission rather than the catalyst. The energy transfer rate for chromophore-catalyst assembly (21 ns) is on the same time scale as in the two chromophore system (33 ns)[4], indicating the chromophore and catalyst are in close contact.

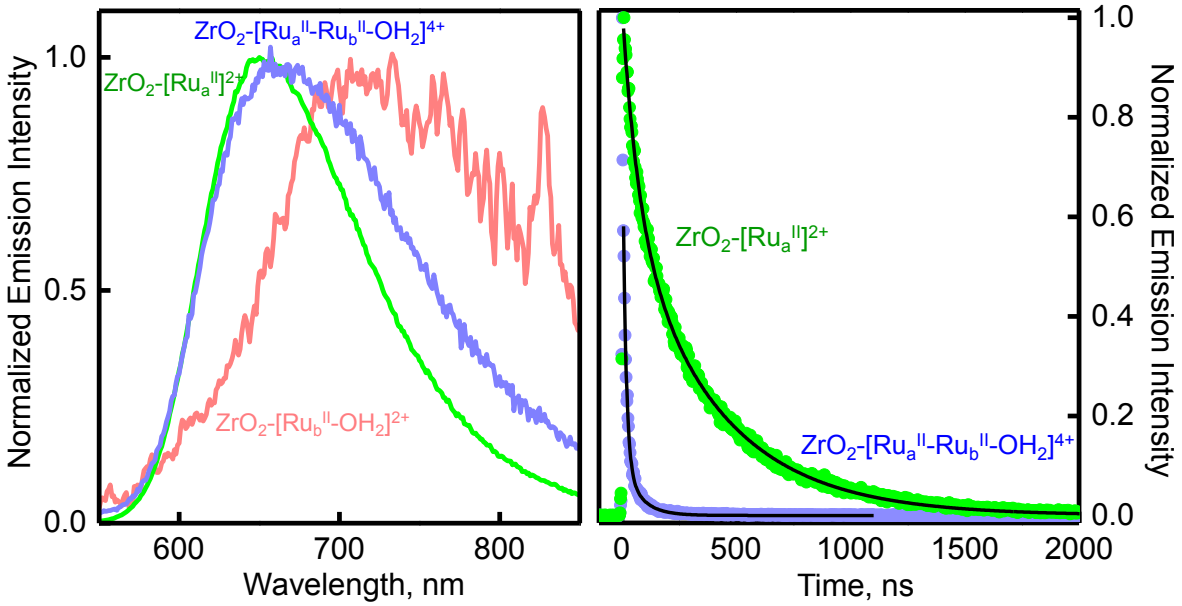

Figure 4.6. (A) Normalized steady-state emission spectra of ZrO_2-$[Ru_a^{II}]^{2+}$ (green), ZrO_2-$[Ru_a^{II}$-Ru_b^{II}-$OH_2]^{4+}$ (blue) and ZrO_2-$[Ru_b^{II}$-$OH_2]^{2+}$ (red). (B) Time-resolved emission collected at 640 nm of ZrO_2-$[Ru_a^{II}]^{2+}$ (green) and ZrO_2-$[Ru_a^{II}$-Ru_b^{II}-$OH_2]^{4+}$ (blue). The fits (black lines) are summarized in Table 4.2. All film samples were in quartz cuvette containing aqueous 0.1 M $HClO_4$, 25 °C. The excitation for emission was 450 nm.

Table 4.2. Summary of the fits of time-resolved emission for ZrO_2-$[Ru_a^{II}]^{2+}$ and ZrO_2-$[Ru_a^{II}$-Ru_b^{II}-$OH_2]^{4+}$.

	A_1	k_1, x10^6 s^{-1} (τ_1,ns)	A_2	k_1, x10^6 s^{-1} (τ_2, ns)	Average k_1, x10^6 s^{-1} (<τ>, ns)
ZrO_2-$[Ru_a^{II}]^{2+}$	0.4 ± 0.01	14.2 ± 0.2 (70.4 ± 1.0)	0.6 ± 0.01	2.57 ± 0.01 (389 ± 1.4)	3.82 ± 0.02 (261.5 ± 1.2)
ZrO_2-$[Ru_a^{II}$-Ru_b^{II}-$OH_2]^{4+}$	0.87 ± 0.01	73.6 ± 1.1 (13.6 ± 0.2)	0.13 ± 0.01	14.3 ± 0.4 (70.0 ± 2.1)	47.8 ± 0.9 (20.9 ± 0.4)

4.3.4. Transfer of the Oxidative Equivalent to the Catalyst

The transient absorption spectra of the assembly, TiO_2-$[Ru_a^{II}$-Ru_b^{II}-$OH_2]^{4+}$, differ in detail from those of the chromophore control, TiO_2-$[Ru_a^{II}]^{2+}$. The most notable difference is a decay of the bleach during the first 1 ns after photoexcitation (Figure 4.3B). This loss of bleach amplitude is primarily due to catalyst excited-states, which are created upon photoexcitation and decay with a lifetime of 360 ps (Figure 4.7). In addition, there is a broadening of the bleach to the red, which is particularly apparent when the transient spectra are normalized to the maximum bleach intensity (Figure 4.3D). This evolution of the spectrum corresponds to an 8-10 nm shift in the red edge of the bleach (measured at the 50% point) that begins at about 10 ps and continues over the first nanosecond (Figure 4.8). This broadening is not observed to the same extent in the chromophore control, which shows only a 2 nm shift over this same time period.

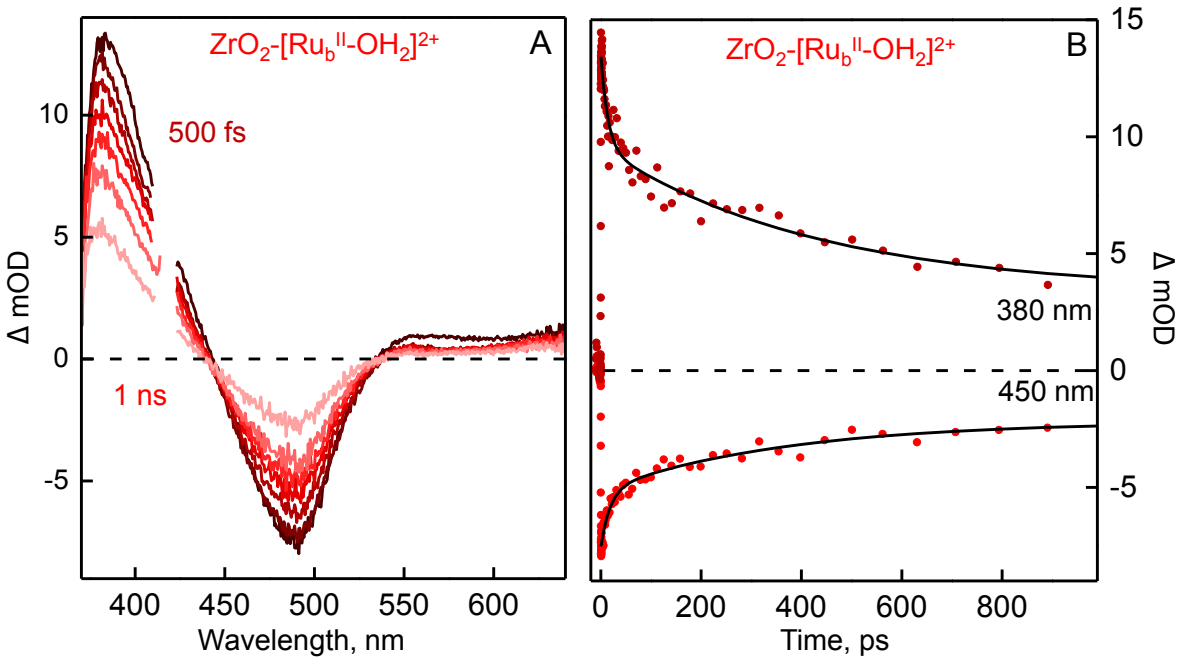

Figure 4.7. (A) Transient absorption spectra of ZrO_2-$[Ru_b^{II}$-$OH_2]^{2+}$ at 1 ps (dark line), 5 ps, 10 ps, 20 ps, 50 ps, 100 ps, 500 ps, and 1 ns (light line) after laser excitation. (B) Transient absorption kinetics of ZrO_2-$[Ru_b^{II}$-$OH_2]^{2+}$ at 380 nm (dark) and 490 nm (light). The fit is shown with black line and summarized in Table 4.3. The sample was on 3 μm thick nanocrystalline ZrO_2 in aqueous 0.1 M $HClO_4$ at 25 °C. The excitation wavelength was 420 nm.

Table 4.3. Summary of the multiexponential fit to the transient absorption signal for ZrO_2-$[Ru_b^{II}$-$OH_2]^{4+}$.

	A_1	k_1, x10^9 s^{-1} (τ_1,ps)	A_2	k_1, x10^9 s^{-1} (τ_2, ns)	Offset
380 nm	3.96 ± 0.35	71.7 ± 0.01 (13.9 ± 2.79)	6.18 ± 0.64	2.33 ± 0.71 (429.7 ± 30.71)	3.37 ± 0.79
490 nm	-2.43 ± 0.23	54.5 ± 9.64 (18.3 ± 3.25)	-2.95 ± 0.25	2.75 ± 0.82 (363.6 ± 108.6)	-2.18 ± 0.32

The broadening of the ground-state bleach to the red in TiO_2-$[Ru_a^{II}$-Ru_b^{II}-$OH_2]^{4+}$ is attributed to the transfer of the oxidative equivalent from the oxidized chromophore to the

catalyst (Scheme 4.2, Eq. 5), whose ground-state absorption spectrum lies to lower energy. The shift of the ground-state bleach takes place with both fast (26 ps) and slow (340 ps) components. While the faster component is also observed in the chromophore control, TiO2-$[Ru_a^{II}]^{2+}$, the slower component is not and we attribute it to the timescale for transfer of the oxidative equivalent to the catalyst, $TiO_2(e^-)$-$[Ru_a^{III}$-Ru_b^{II}-$OH_2]^{5+}$→ $TiO_2(e^-)$-$[Ru_a^{II}$-Ru_b^{III}-$OH_2]^{5+}$.

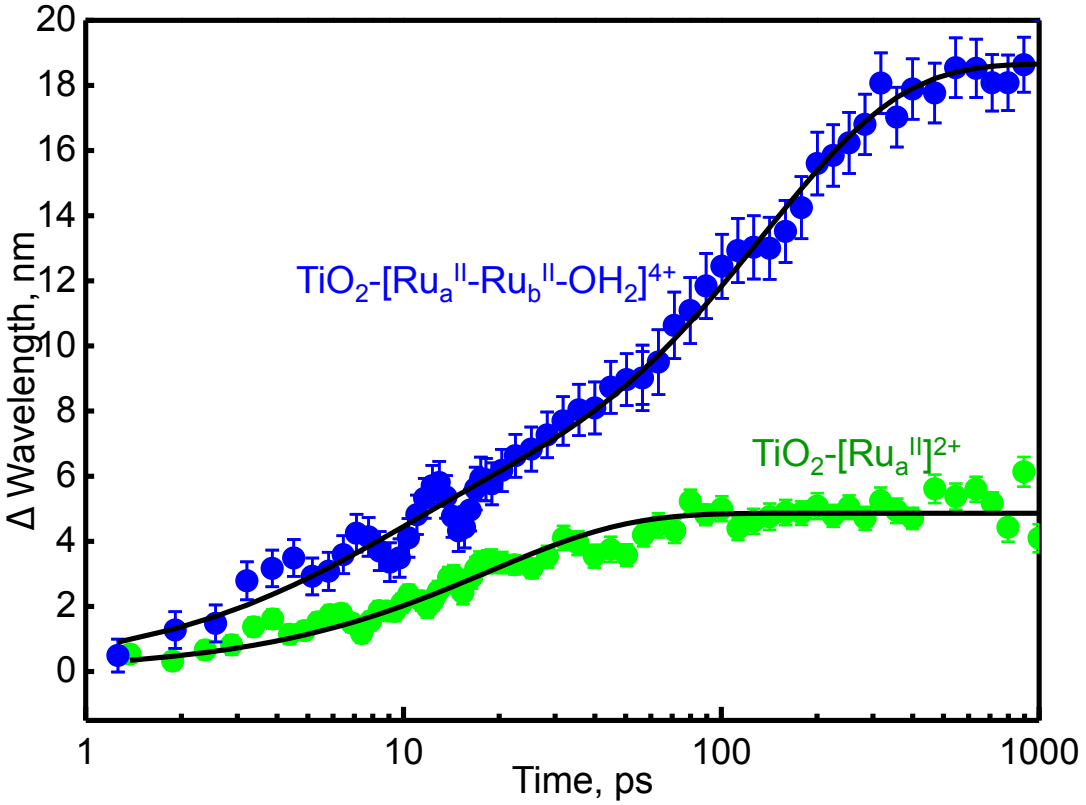

Figure 4.8. The change in red wavelength shift in ground-state bleach (at the 50% point) verses time for TiO_2-$[Ru_a^{II}]^{2+}$ (green) and TiO_2-$[Ru_a^{II}$-Ru_b^{II}-$OH_2]^{4+}$ (blue). The error bars from the linear fit are included. The fits to the curves are shown in black with parameters summarized in Table 4.4.

Table 4.4. Summary of the fit to the change in wavelength of the bleach (at 50% point) for TiO_2-$[Ru_a^{II}]^{2+}$ and TiO_2-$[Ru_a^{II}$-Ru_b^{II}-$OH_2]^{4+}$.

	A_1	τ_1 (ps)	A_2	τ_2 (ps)
TiO_2-$[Ru_a^{II}]^{2+}$	1 ± 0.05	80.84 ± 12.34	--	--
TiO_2-$[Ru_a^{II}$-$Ru_b^{II}]^{4+}$	0.3 ± 0.03	25.51 ± 3.89	0.7 ± 0.03	342.91 ± 48.52

Because $[Ru_a^{II}*]^{2+}$, $[Ru_a^{III}]^{3+}$, $[Ru_b^{II}*$-$OH_2]^{2+}$, and $[Ru_b^{III}$-$OH_2]^{3+}$ all contribute to the transient absorption signal in this spectral window, determining the electron transfer rate simply by monitoring the absorption changes at a single wavelength is problematic. Disentangling the kinetic processes is accomplished by using global analysis based on a singular-value decomposition (SVD) algorithm.

The global analysis fits the transient absorption data matrix between 10 ps and 5 ns to a pre-defined kinetic model, extracting both spectra for each species and their concentration profiles as a function of time. The kinetic model includes the following processes: (i) electron injection from chromophore excited-state (Scheme 4.2, Eq. 4), (ii) the transfer of oxidative equivalent to the catalyst (Scheme 4.2, Eq. 5), and (iii) excited-state decay of catalyst (Scheme 4.2, Eq. 2b). The remaining kinetic processes occur on time scales greater than 5 ns, and are not included in the model. In particular, energy transfer to the catalyst from the chromophore excited-state (Scheme 4.2, Eq. 3) is 20.9 ns, $[Ru_a^{II}*]^{2+}$ excited-state decay (Scheme 4.2, Eq. 2a) is 450 ns, and back electron transfer (Scheme 4.2, Eq. 6) occurs on the microsecond time scale (as discussed below).

The number of adjustable parameters in the global fit of TiO_2-$[Ru_a^{II}$-Ru_b^{II}-$OH_2]^{4+}$ data were reduced by incorporating several key constraints to the spectra and rate constants, which are summarized in Table 4.5. The injection process was characterized separately by performing the same analysis on the chromophore control, TiO_2-$[Ru_a^{II}]^{2+}$ (Figure 4.9). This

analysis gave the rate of electron injection (Scheme 4.2, Eq. 4) and transient spectra for the chromophore excited-state ($[Ru_a^{II}*]^{2+}$) and oxidized chromophore ($[Ru_a^{III}]^{3+}$). In the analysis of the chromophore control data, the spectrum of $[Ru_a^{II}*]^{2+}$ was fixed to the spectrum of TiO_2-$[Ru_a^{II}]^{2+}$ at 500 fs. The initial concentrations of the two species were based on the injection efficiency analysis described above. Specifically, the initial concentrations of $[Ru_a^{II}*]^{2+}$ and $[Ru_a^{III}]^{3+}$ were set at 0.93 and 0.07 to account for the loss of 9% of the injecting chromophores during the instrument response time. The model also accounted for the 28% of chromophores that do not inject during the first nanosecond. The analysis returned a rate constant of $5.6 \times 10^{10}\ s^{-1}$ ($\tau = 18$ ps) and the spectra shown in Figure 4.9A. The global analysis is limited to describing the injection with a single average rate constant, and thus cannot reproduce the kinetic complexity observed in the transient data. Nevertheless, it represents a reasonable description of the injection kinetics and was used for the injection rate in the analysis of the assembly.

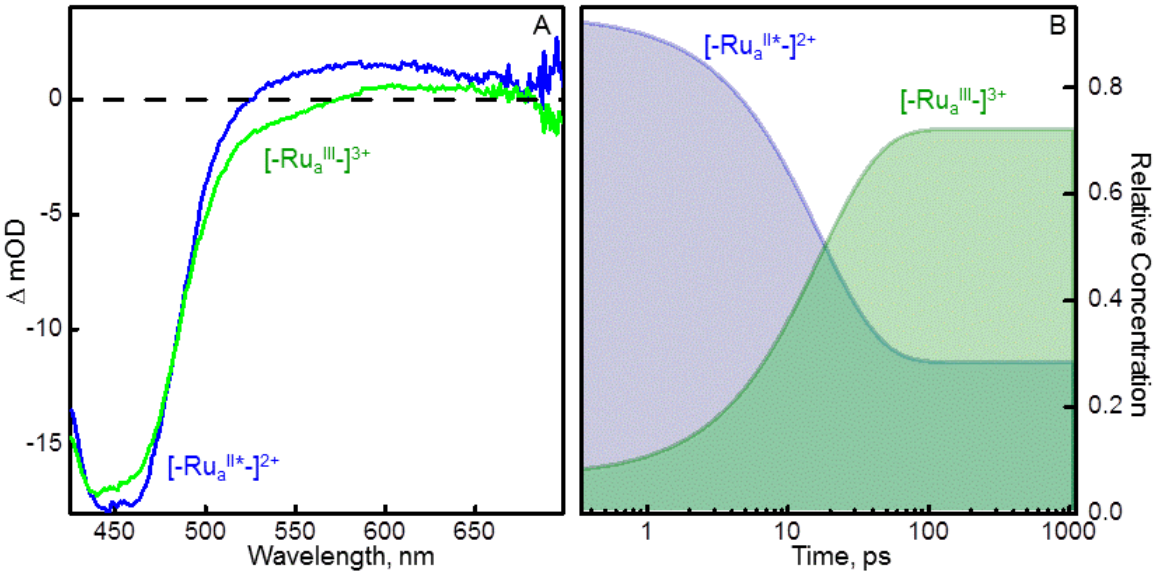

Figure 4.9. Global Analysis of TiO_2-[Ru_a^{II}]$^{2+}$ transient spectra in the 0.5 ps to 1 ns time window. (A) Transient absorption difference spectra for [Ru_a^{II}*]$^{2+}$ (blue) and [Ru_a^{III}]$^{3+}$ (green). (B) Relative concentration of [Ru_a^{II}*]$^{2+}$ (blue) and [Ru_a^{III}]$^{3+}$ (green). The residuals for the fit are shown in Figure 4.10.

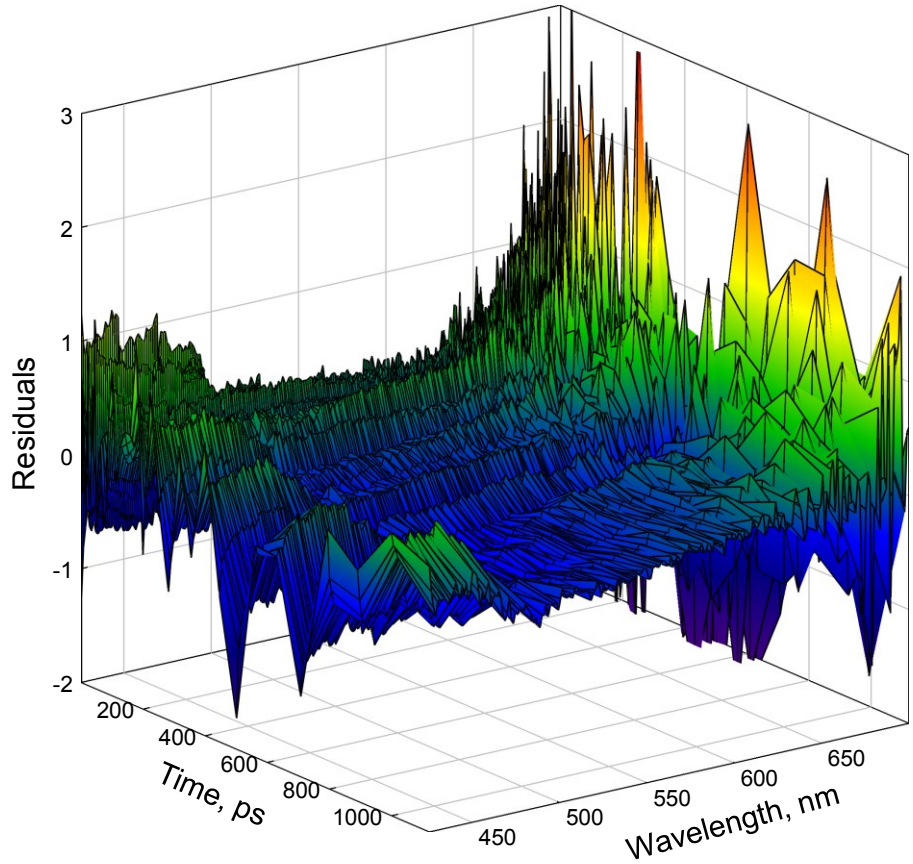

Figure 4.10. Residuals from the global analysis of TiO_2-$[Ru_a^{II}]^{2+}$.

Also fixed were the known spectra for $[Ru_a^{II}*]^{2+}$, $[Ru_a^{III}]^{3+}$, and $[Ru_b^{II}*\text{-}OH_2]^{2+}$ (Table 4.5). The initial concentrations in Table 4.5 account for the relative molar absorptivity of the chromophore and catalyst, and the ultrafast injection yield of the chromophore, which results in the presence of oxidized chromophore ($[Ru_a^{III}]^{3+}$) during the instrument response. The kinetic model also takes into account the overall injection yield (72%), and the fraction of assemblies on the surface whose catalysts are in the photophysically inert, peroxide state (20%). The only adjustable parameters in the global

analysis are the spectrum of the oxidized catalyst $[Ru_b^{III}\text{-}OH_2]^{3+}$ and the rate constant for the transfer of the oxidative equivalent.

The spectra that result from the global analysis of $TiO_2\text{-}[Ru_a^{II}\text{-}Ru_b^{II}\text{-}OH_2]^{4+}$ are shown in Figure 4.11A. The spectrum for $[Ru_b^{III}\text{-}OH_2]^{3+}$ closely resembles the calculated ΔA spectrum for $[Ru_b^{II}\text{-}OH_2]^{2+}/[Ru_b^{III}\text{-}OH_2]^{3+}$ obtained spectroelectrochemically. The concentration profiles for $[Ru_a^{II}]^{2+}$, $[Ru_a^{III}]^{3+}$, $[Ru_b^{II}\text{-}OH_2]^{2+}$ and $[Ru_b^{III}\text{-}OH_2]^{3+}$ are shown in Figure 4.11B. From the global analysis the calculated rate constant for the transfer of the oxidative equivalent to the catalyst is $2.6 \times 10^9\ s^{-1}$ (τ = 380 ps). The analysis indicates an efficiency for transfer of the oxidative equivalent of nearly 100%, based on the relative lifetimes, with overall efficiency for first photoactivation step of 49%. The relatively low efficiency is due to the presence of inactive peroxide assemblies on the surface, as well as the relatively low electron injection efficiency.

Table 4.5. Summary of global analysis constraint and initial/final concentrations.

Chemical Species	Spectral Contribution	Concentration	
		Initial	Final
Chromophore Excited-state, $[Ru_a^{II}*]^{2+}$	Fixed[(a)]	0.79	0.24[(c)]
Oxidized Chromophore, $[Ru_a^{III}]^{3+}$	Fixed[(a)]	0.06	0.12[(d)]
Catalyst Excited-state, $[Ru_b^{II}*]^{2+}$	Fixed[(b)]	0.15	0.00
Oxidized Catalyst, $[Ru_b^{III}]^{3+}$	Adjustable	0.00	0.49
Ground-state	Non absorptive	0.00	0.15
Dynamical Process	Rate Constant		
Electron Injection, Eq. 4	Fixed[(a)]	$(18\ ps)^{-1}$	
Catalyst Excited-state Decay, Eq. 2b	Fixed[(b)]	$(363\ ps)^{-1}$	
Oxidative transfer, Eq. 5	Adjustable	$(380\ ps)^{-1}$	

a.) From SVD analysis of TiO_2-$[Ru_a^{II}]^{2+}$. Spectra shown in Figure 4.9A.

b.) Transient absorption data obtained for the catalyst control, ZrO_2-$[Ru_b^{II}$-$OH_2]^{2+}$, Figure 4.7.

c.) Accounts for $[Ru_a^{II}*]^{2+}$ population that does not inject during first 1 ns, based on injection efficiency measurements.

d.) Final concentration accounts for the fraction of chromophores that are attached to assemblies containing catalysts in the peroxide state.

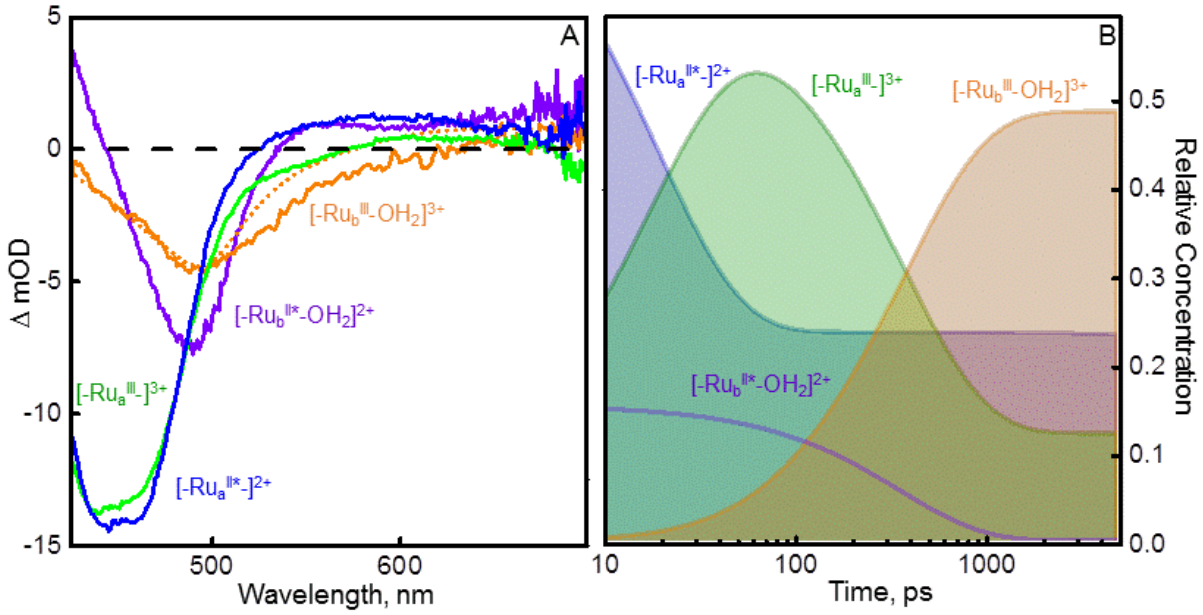

Figure 4.11. Global analysis of TiO_2-$[Ru_a^{II}$-Ru_b^{II}-$OH_2]^{4+}$. (A) The spectra of $[Ru_a^{II}]^{2+}$ (blue), $[Ru_a^{III}]^{3+}$ (green), $[Ru_b^{III}$-$OH_2]^{3+}$ (orange), and $[Ru_b^{II}*$-$OH_2]^{2+}$ (purple). Also shown is the calculated ΔA spectrum for $[Ru_b^{II}$-$OH_2]^{2+}$/$[Ru_b^{III}$-$OH_2]^{3+}$ (dashed orange) (B) Relative concentrations of $[Ru_a^{II}*]^{2+}$ (blue), $[Ru_a^{III}]^{3+}$ (green), $[Ru_b^{III}$-$OH_2]^{3+}$ (orange), and $[Ru_b^{II}*$-$OH_2]^{2+}$ (purple). The residuals for the global fit are shown in Figure 4.12. The concentrations shown at 10 ps are different from the initial concentrations for the fit due to electron injection of the chromophore that occurs between 500 fs and 10 ps.

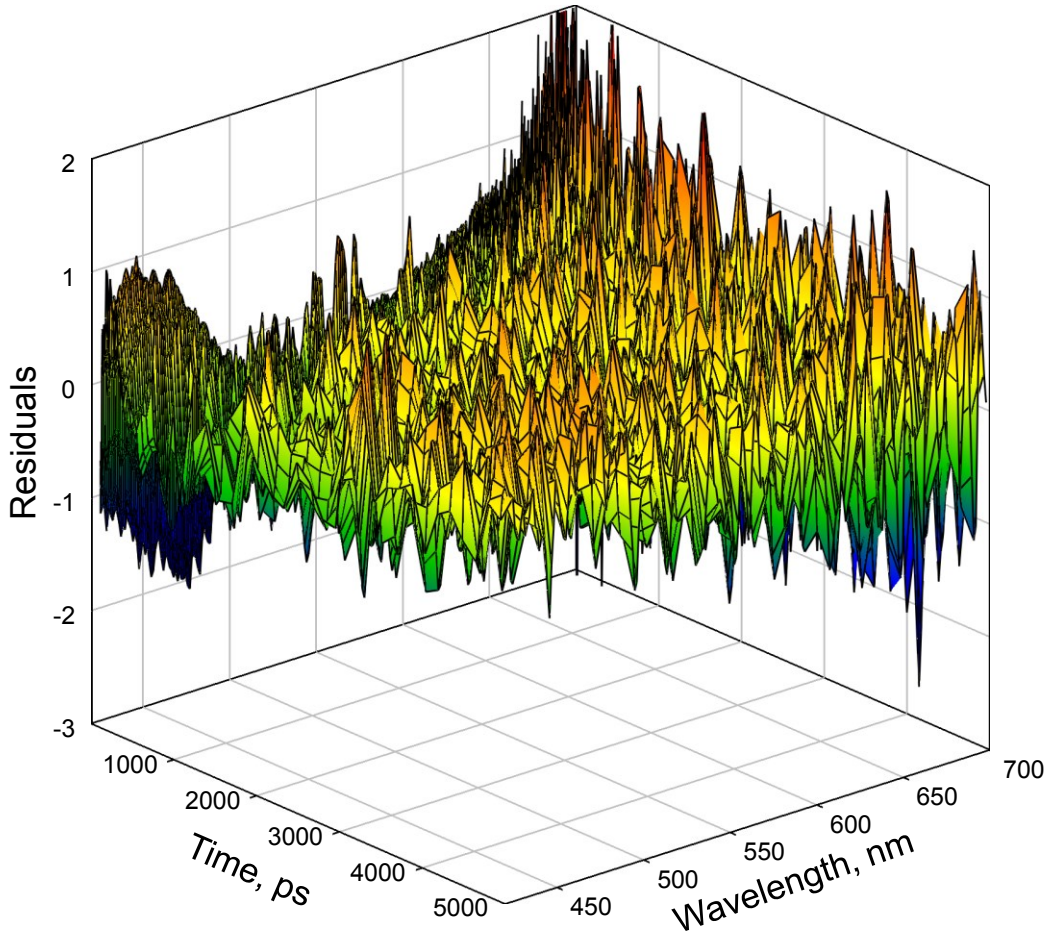

Figure 4.12. Residuals from the global analysis of TiO_2-$[Ru_a^{II}$-Ru_b^{II}-$OH_2]^{4+}$.

4.3.5. Charge Recombination

Recombination of the electron in TiO_2 with the hole on either the chromophore, $[Ru_a^{III}]^{3+}$, or catalyst, $[Ru_b^{III}$-$OH_2]^{3+}$, (Scheme 4.2, Eq. 6) is monitored by following the decay of the ground-state bleach at 490 nm on the microsecond time scale (Figure 4.13). The decay kinetics are qualitatively similar for the assembly and the chromophore control, Figure 14. Both are highly multiexponential with power law behavior observed at long times, as indicated by the linear behavior when the decay is depicted in log (ΔA) vs. log (t) plots. While power law behavior is characteristic of many types of dynamical phenomena, it is a

characteristic feature of trap-to-trap hopping in metal oxide materials.[21-24] This suggests that the decay might be determined more by internal electron dynamics within the TiO_2 than the back electron transfer process itself. This conclusion also accounts for the similarity observed in recombination kinetics for TiO_2-$[Ru_a^{II}]^{2+}$ and TiO_2-$[Ru_a^{II}$-Ru_b^{II}-$OH_2]^{4+}$.

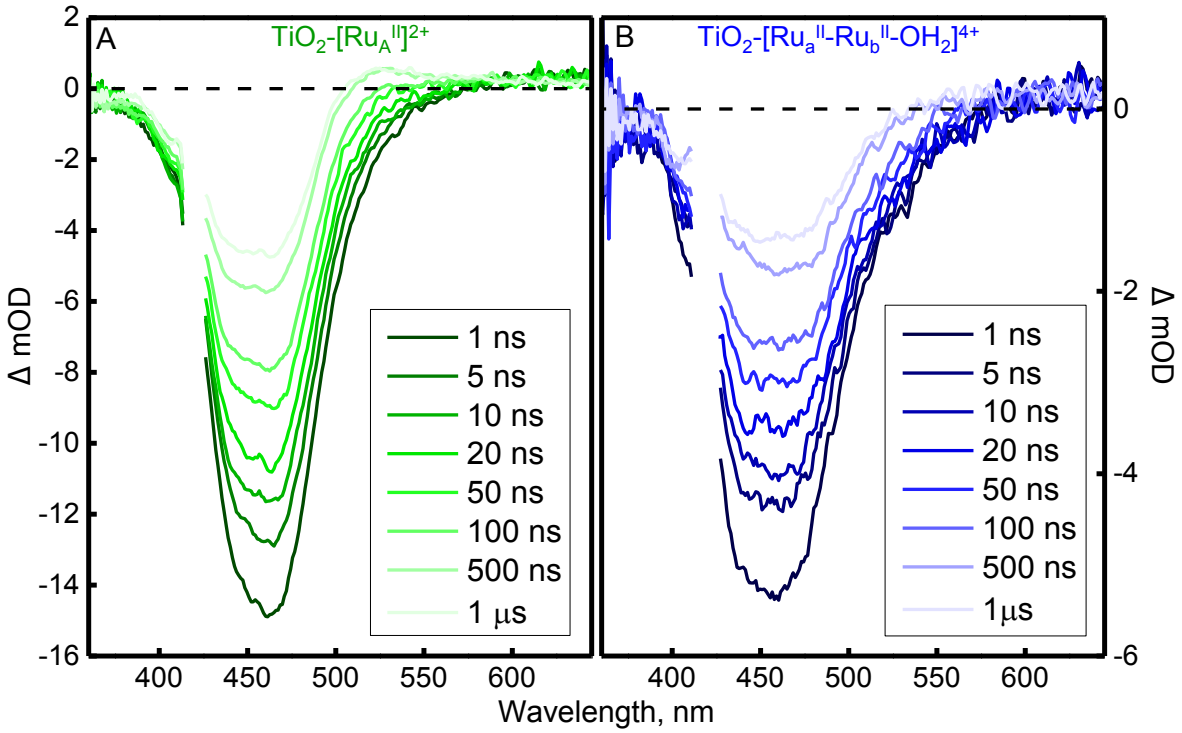

Figure 4.13. Transient absorption spectra of (A) TiO_2-$[Ru_a^{II}]^{2+}$ and (B) TiO_2-$[Ru_a^{II}$-Ru_b^{II}-$OH_2]^{4+}$ from 1 ns to 1 μs after laser excitation. Both samples were on 1 μm thick nanocrystalline TiO_2 in aqueous 0.1 M $HClO_4$ at 25 °C. The excitation wavelength was 420 nm.

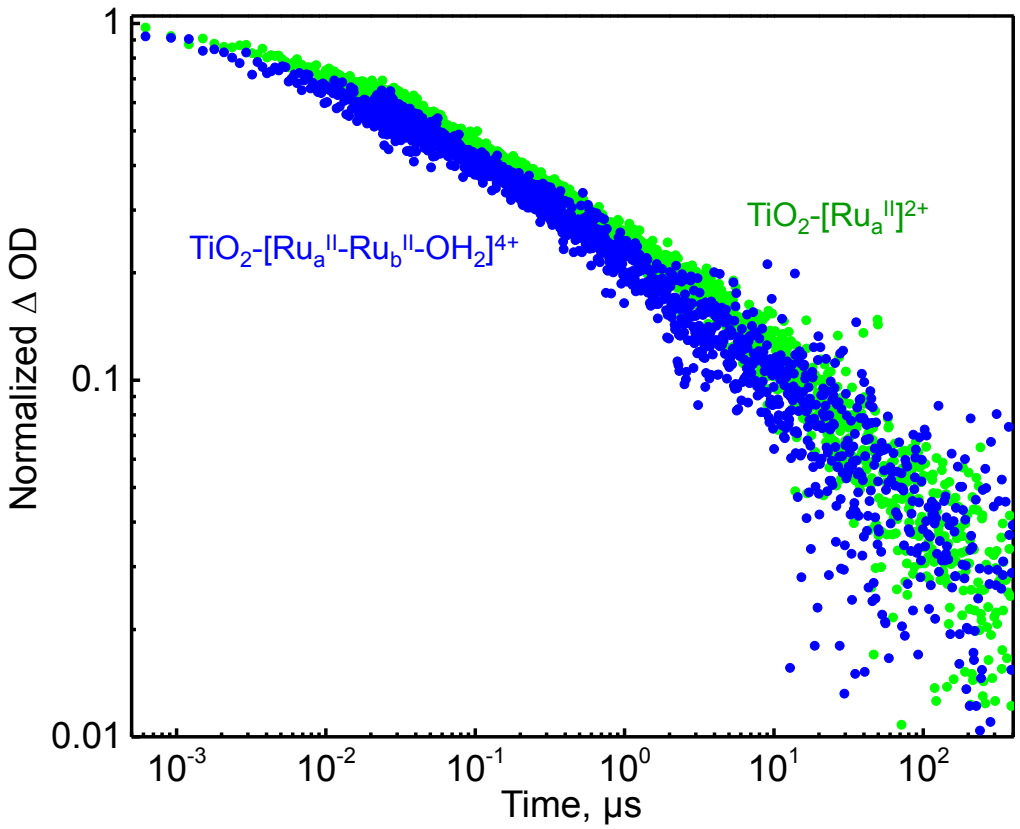

Figure 4.14. Transient absorption kinetics for back electron transfer monitored at 490 nm for TiO_2-[Ru_a^{II}]$^{2+}$ (green) and TiO_2-[Ru_a^{II}-Ru_b^{II}-OH_2]$^{4+}$ (blue). The signal was inverted and normalized. The excitation wavelength was 420 nm. All samples were on 1 μm thick TiO_2 films in aqueous 0.1 M $HClO_4$ solution at 25°C.

4.4. CONCLUSIONS

An oligoproline functionalized with a phosphonated $Ru(bpy)_3^{2+}$ chromophore and a $Ru(bpy)(Mebimpy)(OH_2)^{2+}$ derivatized water oxidation catalyst was loaded onto nanoporous TiO_2 and its interfacial and intra-assembly electron transfer dynamics were analyzed by transient femtosecond absorption spectroscopy. Upon ultrafast electron injection from the chromophore excited-state into the TiO_2 the oxidative equivalent is transferred from the chromophore to the catalyst. With the use of global analysis, the transfer of the oxidative

equivalent to the catalyst occurred with $k = 2.6 \times 10^9\ s^{-1}$ (τ = 380 ps). The assembly resulted in efficiency for transfer of the oxidative equivalent to the catalyst of nearly 100%, based on the relative lifetimes, with an overall efficiency of 49% for the initial DSPEC photoexcitation step. The low overall efficiency is a result of the electron injection efficiency of the chromophore (72%) and the 20% of inactive catalysts in the sample. A redesign of the assembly with a chromophore that has an injection efficiency near unity (by separating the amide functional group from the bipyridine ligand), and 100% active catalysts would increase the overall efficiency to 76%. Future studies will utilize the versatility of the proline scaffold and focus on the influence of spacer distance between the chromophore and catalyst on intra-assembly electron transfer.

REFERENCES

(1) Alstrum-Acevedo, J. H.; Brennaman, M. K.; Meyer, T. J. Inorg. Chem. 2005, 44, 6802-6827.

(2) Lewis, N. S.; Nocera, D. G. Proceedings of the National Academy of Sciences 2006, 103, 15729-15735.

(3) Li, F.; Jiang, Y.; Zhang, B.; Huang, F.; Gao, Y.; Sun, L. Angew. Chem. Int. Ed. 2012, 51, 2417-2420.

(4) Norris, M. R.; Concepcion, J. J.; Harrison, D. P.; Binstead, R. A.; Ashford, D. L.; Fang, Z.; Templeton, J. L.; Meyer, T. J. J. Am. Chem. Soc. 2013, 135, 2080-2083.

(5) Song, W.; Glasson, C. R. K.; Luo, H.; Hanson, K.; Brennaman, M. K.; Concepcion, J. J.; Meyer, T. J. The Journal of Physical Chemistry Letters 2011, 2, 1808-1813.

(6) Ashford, D. L.; Song, W.; Concepcion, J. J.; Glasson, C. R. K.; Brennaman, M. K.; Norris, M. R.; Fang, Z.; Templeton, J. L.; Meyer, T. J. J. Am. Chem. Soc. 2012, 134, 19189-19198.

(7) Huang, Z.; Geletii, Y. V.; Musaev, D. G.; Hill, C. L.; Lian, T. Industrial & Engineering Chemistry Research 2012, 51, 11850-11859.

(8) Concepcion, J. J.; Jurss, J. W.; Templeton, J. L.; Meyer, T. J. J. Am. Chem. Soc. 2008, 130, 16462-16463.

(9) Concepcion, J. J.; Tsai, M.-K.; Muckerman, J. T.; Meyer, T. J. Journal of the American Chemical Society 2010, 132, 1545-1557.

(10) Concepcion, J. J.; Jurss, J. W.; Brennaman, M. K.; Hoertz, P. G.; Patrocinio, A. O. v. T.; Murakami Iha, N. Y.; Templeton, J. L.; Meyer, T. J. Accounts of Chemical Research 2009, 42, 1954-1965.

(11) Ma, D.; Bettis, S. E.; Hanson, K.; Minakova, M.; Alibabaei, L.; Fondrie, W.; Ryan, D. M.; Papoian, G. A.; Meyer, T. J.; Waters, M. L.; Papanikolas, J. M. J. Am. Chem. Soc. 2013, 135, 5250-5253.

(12) Ryan, D. M.; Coggins, M. K.; Concepcion, J. J.; Ashford, D. L.; Fang, Z.; Alibabaei, L.; Ma, D.; Meyer, T. J.; Waters, M. L. To be determined 2013, Na, Na.

(13) Hanson, K.; Brennaman, M. K.; Ito, A.; Luo, H.; Song, W.; Parker, K. A.; Ghosh, R.; Norris, M. R.; Glasson, C. R. K.; Concepcion, J. J.; Lopez, R.; Meyer, T. J. The Journal of Physical Chemistry C 2012, 116, 14837-14847.

(14) Juris, A.; Balzani, V.; Barigelletti, F.; Campagna, S.; Belser, P.; Vonzelewsky, A. Coord. Chem. Rev. 1988, 84, 85-277.

(15) Asbury, J. B.; Ellingson, R. J.; Ghosh, H. N.; Ferrere, S.; Nozik, A. J.; Lian, T. The Journal of Physical Chemistry B 1999, 103, 3110-3119.

(16) Myahkostupov, M.; Piotrowiak, P.; Wang, D.; Galoppini, E. The Journal of Physical Chemistry C 2007, 111, 2827-2829.

(17) Benkö, G.; Kallioinen, J.; Korppi-Tommola, J. E. I.; Yartsev, A. P.; Sundström, V. J. Am. Chem. Soc. 2001, 124, 489-493.

(18) Liu, F.; Meyer, G. J. Inorg. Chem. 2005, 44, 9305-9313.

(19) Benkö, G.; Kallioinen, J.; Myllyperkiö, P.; Trif, F.; Korppi-Tommola, J. E. I.; Yartsev, A. P.; Sundström, V. The Journal of Physical Chemistry B 2004, 108, 2862-2867.

(20) Schoonover, J. R.; Dattelbaum, D. M.; Malko, A.; Klimov, V. I.; Meyer, T. J.; Styers-Barnett, D. J.; Gannon, E. Z.; Granger, J. C.; Aldridge, W. S.; Papanikolas, J. M. J. Phys. Chem. A 2005, 109, 2472-2475.

(21) McNeil, I. J.; Ashford, D. L.; Luo, H.; Fecko, C. J. The Journal of Physical Chemistry C 2012, 116, 15888-15899.

(22) Mora-Seró, I.; Dittrich, T.; Belaidi, A.; Garcia-Belmonte, G.; Bisquert, J. The Journal of Physical Chemistry B 2005, 109, 14932-14938.

(23) Seki, K.; Wojcik, M.; Tachiya, M. The Journal of Chemical Physics 2006, 124, 044702.

(24) Kopidakis, N.; Benkstein, K. D.; van de Lagemaat, J.; Frank, A. J. The Journal of Physical Chemistry B 2003, 107, 11307-11315.

CHAPTER 5. PHOTOPHYSICAL CHARACTERIZATION OF CHROMOPHORE-WATER OXIDATIONCATALYST CONTAINING LAYER-BY-LAYER ASSEMBLY ON NANOCRYSTALLINE TiO_2 USING ULTRAFAST SPECTROSCOPY[4]

[4]This chapter has been submitted for publication as an article in the Journal of Physical Chemistry C.

5.1. INTRODUCTION

A primary strategy for solar fuels production is a dye-sensitized photoelectrosynthesis cell (DSPEC) that can use sunlight to drive water oxidation and reduction of protons to hydrogen or CO_2 to carbon-based fuels.[1-2] Central to a DSPEC device architecture is designing a means for arranging the light-absorbing chromophores and catalysts in close proximity to facilitate electron transfer activation of the catalyst toward water oxidation. There are a limited number of examples of systems that successfully incorporate light-harvesting chromophores and catalysts on nanocrystalline semiconductor surfaces.[3-8] Most approaches are synthetically challenging, often with a lack of versatility. A "layer-by-layer" approach was recently reported by Hanson et. al[9] based on earlier work of Mallouk and Haga.[10-13] This approach does not require the prior synthesis of a covalently-bonded assembly. The chromophore and catalyst are synthesized independently, and then bound to the metal oxide surface in a stepwise, self-assembled fashion, (i.e. chromophore then Zr^{4+} ions and then catalyst).

Solar water oxidation requires the sequential transfer of four electrons and four protons in the net reaction $2H_2O \rightarrow O_2 + 4H^+ + 4e^-$.[1] Significant progress has been made in the development of polypyridyl-based Ru(II)-aqua catalysts for water oxidation with mechanistic details established both in solution, and on oxide surfaces using electrochemical or chemical techniques.[14-16] In a DSPEC, each step in the water oxidation cycle involves the photo-oxidation of the chromophore via electron injection into the metal oxide film, followed by the transfer of the oxidative equivalent to the catalyst. The "layer-by-layer" system includes a chromophore, $[Ru_a^{II}]^{2+}$ ($[Ru(pbpy)_2(bpy)]^{2+}$, bpy = 2,2'-bipyridine and pbpy = 4,4'-$(PO_3H_2)_2$bpy)), and a water oxidation catalyst, $[Ru_b^{II}\text{-}OH_2]^{2+}$ ([Ru(4,4'-

$(CH_2PO_3H_2)_2bpy)(Mebimpy)(H_2O)]^{2+}$, Mebimpy=2,6-bis(1-methylbenzimidazol-2-yl)pyridine)), linked by Zr^{4+} ions that are coordinated to the phosphonate groups on each of the metal complexes (Figure 5.1). This approach results in a self-assembled film consisting of a layer of $[Ru_a^{II}]^{2+}$ chromophores anchored to the TiO_2 through one pbpy ligand and, through a second pbpy ligand, a layer of $[Ru_b^{II}\text{-}OH_2]^{2+}$ catalyst complexes.[9] Here we report the photophysical characterization of the first photoactivation step of the water oxidation catalyst in this assembly, $TiO_2\text{-}[Ru_a^{II}\text{-}Zr\text{-}Ru_b^{II}\text{-}OH_2]^{4+}$, using femtosecond transient absorption.

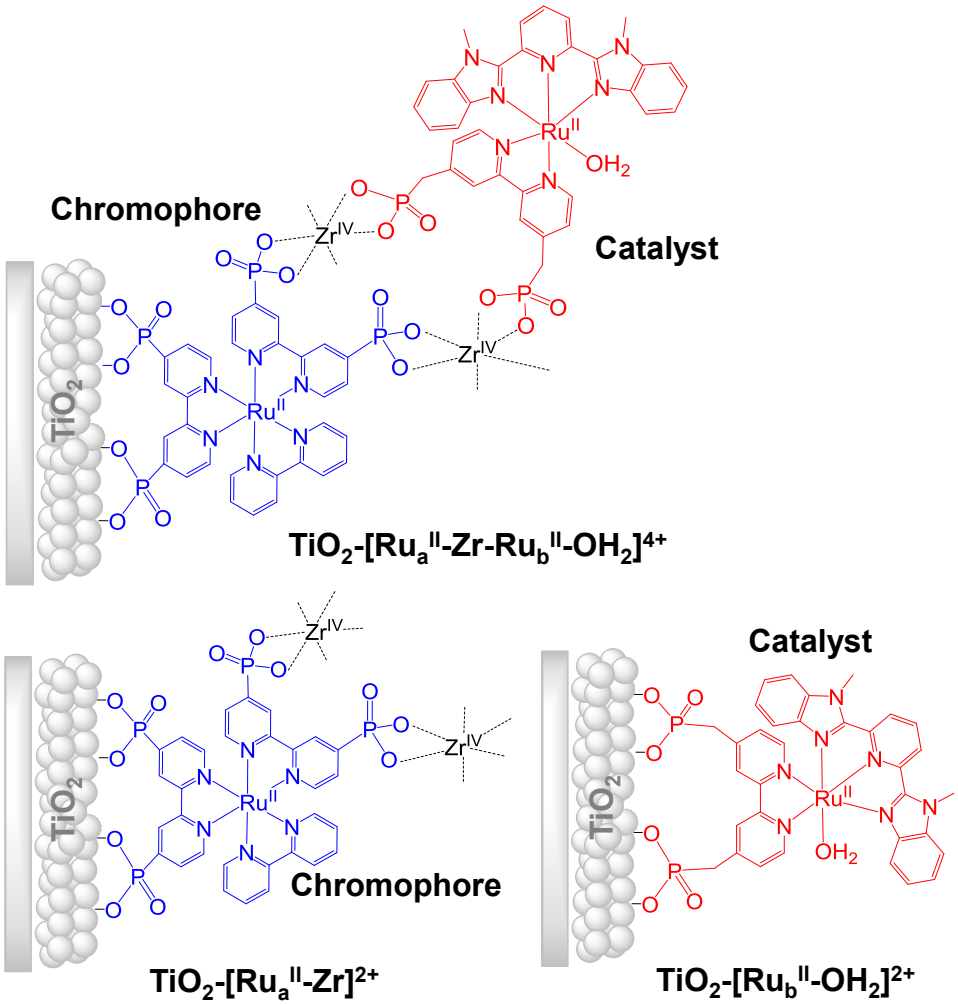

Figure 5.1. Schematic design of the bilayer molecular assembly $[Ru_a^{II}\text{-}Zr\text{-}Ru_b^{II}\text{-}OH_2]^{4+}$, the chromophore $[Ru_a^{II}\text{-}Zr]^{2+}$, and catalyst $[Ru_b^{II}\text{-}OH_2]^{2+}$on nanocrystalline TiO_2 films. The bonding motif of $TiO_2\text{-}[Ru_a^{II}\text{-}Zr\text{-}Ru_b^{II}\text{-}OH_2]^{4+}$ is possible but does not exclude other bonding modes.

The kinetic processes involved in this step are illustrated in Scheme 5.1. Photoexcitation of the assembly $TiO_2\text{-}[Ru_a^{II}\text{-}Zr\text{-}Ru_b^{II}\text{-}OH_2]^{4+}$ results in either excitation of the chromophore (Scheme 5.1, Eq. 1a), or the catalyst (Eq. 1b). Chromophore excitation is followed by electron injection into TiO_2, $TiO_2\text{-}[Ru_a^{II}*\text{-}Zr\text{-}Ru_b^{II}\text{-}OH_2]^{4+} \rightarrow TiO_2(e^-)\text{-}[Ru_a^{III}\text{-}Zr\text{-}Ru_b^{II}\text{-}OH_2]^{5+}$ (Eq. 4), resulting in the formation of oxidized chromophore at the surface. Once

formed, transfer of the oxidative equivalent to the catalyst occurs (i.e. intra-assembly electron transfer), $TiO_2(e^-)$-$[Ru_a^{III}$-Zr-Ru_b^{II}-$OH_2]^{5+}$ → $TiO_2(e^-)$-$[Ru_a^{II}$-Zr-Ru_b^{III}-$OH_2]^{5+}$ (Eq. 5), completing the first photoactivation of the water oxidation catalyst. Experiments reported here indicate that activation of the catalyst occurs with a time constant of 170 ps. Energy transfer from photoexcited chromophore to the catalyst, TiO_2-$[Ru_a^{II}*$-Zr-Ru_b^{II}-$OH_2]^{4+}$ → TiO_2-$[Ru_a^{II}$-Zr-$Ru_b^{II}*$-$OH_2]^{4+}$ (Eq. 3) is also possible, and is a potentially deleterious energy loss pathway. However, the timescale for this process is significantly slower (20 ns) than electron injection, limiting its relevance. A more important deactivation pathway is "recombination" by back electron transfer from the semiconductor to the oxidized catalyst, $TiO_2(e^-)$-$[Ru_a^{II}$-Zr-Ru_b^{III}-$OH_2]^{5+}$ → TiO_2-$[Ru_a^{II}$-Zr-Ru_b^{II}-$OH_2]^{5+}$ (Eq. 6b), which returns the surface assembly to its initial state with the transiently stored oxidative equivalent lost as heat. Successful utilization of these interfacial injection/electron transfer schemes requires long recombination times, which can be achieved either by rapid removal of injected electrons from the semiconductor or by slowing back electron transfer by manipulating the assembly structure.

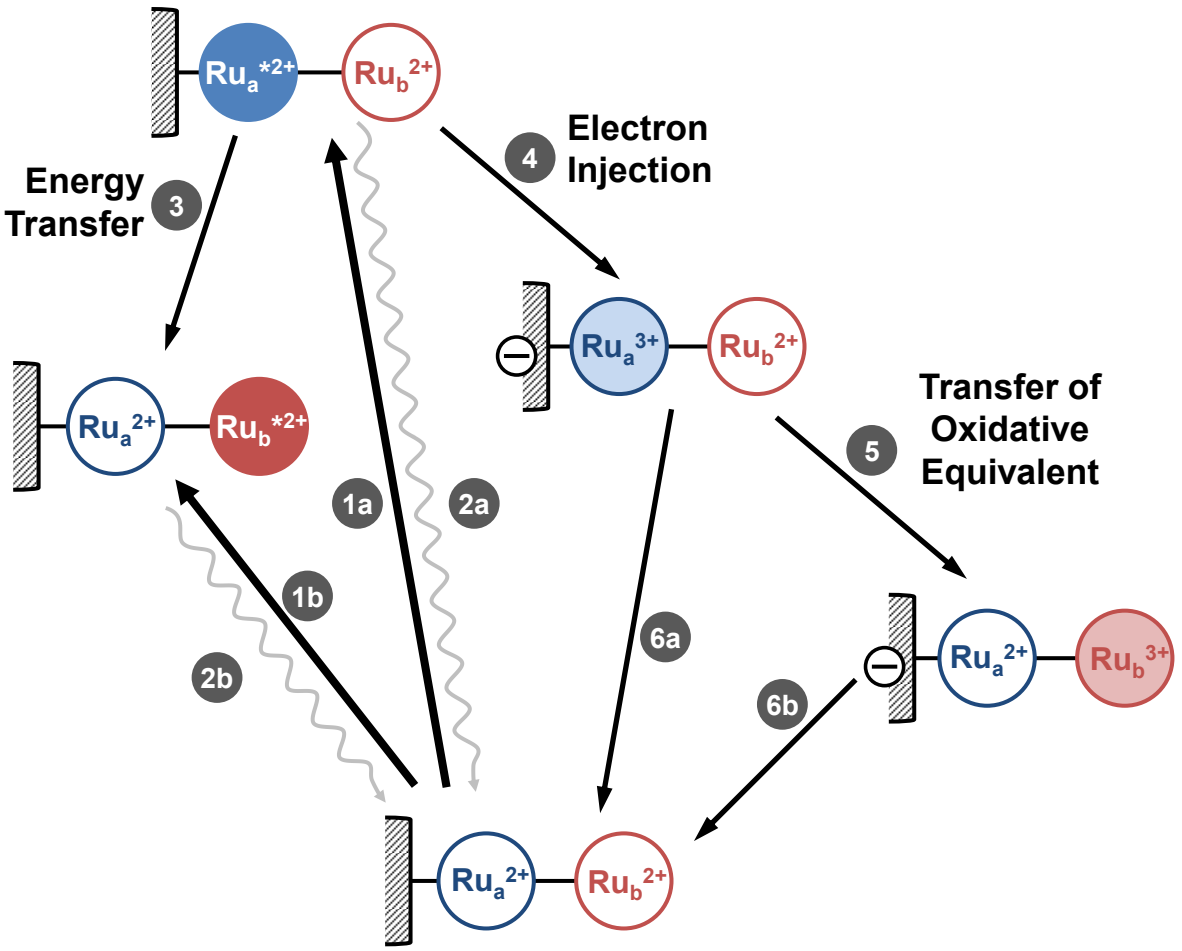

Scheme 5.1. Schematic diagram illustrating the kinetic processes for TiO_2-[Ru_a^{II}-Zr-Ru_b^{II}-OH_2]$^{4+}$ that occur following photoexcitation.

5.2. EXPERIMENTAL

5.2.1. Sample Preparation

The synthesis of [Ru_a^{II}]$^{2+}$ and [Ru_b^{II}-OH_2]$^{2+}$ and the "layer-by-layer" method have been previously published.[9] Briefly the "layer-by-layer" method was carried out by soaking the nanocrystalline film in a sequence of three separate aqueous solutions, each overnight (12 hours). The preparation of sample TiO_2-[Ru_a^{II}-Zr]$^{2+}$ involved soaking the nanocrystalline film in 0.1 M $HClO_4$ solutions of [Ru_a^{2+}]$^{2+}$ (150 μM) followed by $ZrOCl_2$ (0.5mM).[9] Sample TiO_2-[Ru_a^{II}-Zr-Ru_b^{II}-OH_2]$^{4+}$ was prepared in a similar manner by soaking the film in 0.1 M

$HClO_4$ solutions of 1) $[Ru_a^{II}]^{2+}$ (150 μM) and 2) $ZrOCl_2$ (0.5mM), and 3) $[Ru_b^{II}\text{-}OH_2]^{2+}$ (150 μM).[9]

The films were placed in a 1.0 cm cuvette at 45 degree angle from the incident laser beam. All samples were purged in Argon for >45 minutes just prior to data collection. The solvent for each sample was 0.1 M $HClO_4$. The surface coverage on TiO_2 for TiO_2-$[Ru_a^{II}\text{-}Zr]^{2+}$, TiO_2-$[Ru_b^{II}\text{-}OH_2]^{2+}$ and TiO_2-$[Ru_a^{II}\text{-}Zr\text{-}Ru_b^{II}\text{-}OH_2]^{4+}$ were $\Gamma = 2.6 \times 10^{-8}$ mol/cm^2/μm, $\Gamma = 2.0 \times 10^{-8}$ mol/cm^2/μm and $\Gamma = 3.1 \times 10^{-8}$ mol/cm^2/μm, respectively, consistent with closely packed surfaces.[17] Similarly, surface coverage for ZrO_2-$[Ru_a^{II}\text{-}Zr]^{2+}$, ZrO_2-$[Ru_b^{II}\text{-}OH_2]^{2+}$, and ZrO_2-$[Ru_a^{II}\text{-}Zr\text{-}Ru_b^{II}\text{-}OH_2]^{4+}$ were $\Gamma = 3.0 \times 10^{-8}$ mol/cm^2/μm, $\Gamma = 2.4 \times 10^{-8}$ mol/cm^2/μm and $\Gamma = 2.9 \times 10^{-8}$ mol/cm^2/μm, respectively.

5.2.2. Steady-state Techniques

Ground-state absorbance measurements were conducted with a Hewlett Packard 8453 UV-VIS-NIR absorption spectrophotometer. Steady state emission (SSE) data were collected using an Edinburgh Instruments FLS920 equipped with a 450 W Xenon lamp and photomultiplier tube (Hamamatsu 2658P). SSE data were collected using a bandwidth no larger than 4.0 nm and, once collected, were corrected for the emission spectrophotometer's spectral response.

5.2.3. Time-resolved Emission

The FLS920 was also used for time-resolved measurements by the time-correlated single photon counting (TCSPC) technique with an instrument response of 2 ns, using a 444.2 nm diode laser (Edinburgh Instruments EPL- 445, 73 ps FWHM pulsewidth) operated at 200 kHz. A 495 nm long pass color filter was used for emission experiments.

5.2.4. Ultrafast Transient Absorption

The femtosecond transient absorption measurements were done using a pump-probe technique based on a Ti:Sapphire chirped pulse amplification (CPA) laser system (Clark-MXR CPA-2001). The 420 nm pump pulse (100 nJ) was produced by sum frequency generation of 900 nm, the frequency doubled output from an Optical Parametric Amplifier (OPA), and a portion of the 775 nm regenerative amplifier beam. A white light continuum generated in a CaF_2 window was used as the probe pulse. The pump and the probe polarizations were set to magic angle, and the probe beam was focused to a 150 μm spot size. The probe pulse collected and directed into a fiber optic coupled multichannel spectrometer with a CMOS diode array detector. The pump pulse was chopped at 500 Hz with a mechanical chopper synchronized to the laser, and pump-induced changes in the white light continuum were measured on a pulse-pulse basis. The instrument has a sensitivity of 1 mOD, and is capable of measuring transient absorption spectra from 350 nm to 750 nm with a time resolution approximately 250 fs.

5.2.5. Picosecond Transient Absorption

Pump-probe transient absorption measurements on the ps-μs time scale were accomplished using the same pump pulse as the femtosecond instrument, but the probe pulse was generated by continuum generation in a diode-laser pumped photonic crystal fiber and electronically delayed relative to the pump pulse. The time resolution of the instrument is 500 ps primarily dictated by the timing electronics.

5.3. RESULTS AND DISCUSSION

We have used transient absorption spectroscopy to characterize the dynamical processes that occur in the initial photoactivation step in the water oxidation cycle of a

chromophore-catalyst bilayer film on TiO_2. Our results indicate that photoexcitation of the chromophore results in electron injection into the TiO_2 with 81% efficiency on time scales that range from femtoseconds to several hundred picoseconds, to produce an oxidized chromophore. Transfer of the oxidative equivalent (i.e. catalyst to chromophore electron transfer) occurs with a time constant of 170 ps, a process that is substantially faster than the charge recombination that occurs on the microsecond time scale.[17]

5.3.1. Photoexcitation

The ground-state absorption spectra of the chromophore, $[Ru_a^{II}\text{-}Zr]^{2+}$, and the catalyst, $[Ru_b^{II}\text{-}OH_2]^{2+}$, exhibit a singlet metal-to-ligand charge transfer (^{1}MLCT) band centered between 400 – 500 nm (Figure 5.2). The maximum absorption of the catalyst (494 nm) is red shifted compared to the chromophore (473 nm), due to the extended π-orbital conjugation of the Mebimpy ligand. The ground-state absorption spectra of $[Ru_a^{II}\text{-}Zr\text{-}Ru_b^{II}\text{-}OH_2]^{4+}$ on TiO_2 and ZrO_2 is well-described by a superposition of the absorption spectra of $[Ru_a^{II}\text{-}Zr]^{2+}$ and $[Ru_b^{II}\text{-}OH_2]^{2+}$ in the MLCT region, indicative of weak electronic coupling between the chromophore and catalyst (Figure 5.2). The chromophore to catalyst ratio in the $[Ru_a^{II}\text{-}Zr\text{-}Ru_b^{II}\text{-}OH_2]^{4+}$ bilayer films on TiO_2 and ZrO_2 is 1:1.5 and 1:1.3, respectively. An excess of catalyst in the film is not unusual for this system due to the nature of the assembly formation. Based on our analysis of the absorption spectra on TiO_2 at 420 nm, ~53% of the photons are absorbed by the chromophore and 47% by the catalyst.

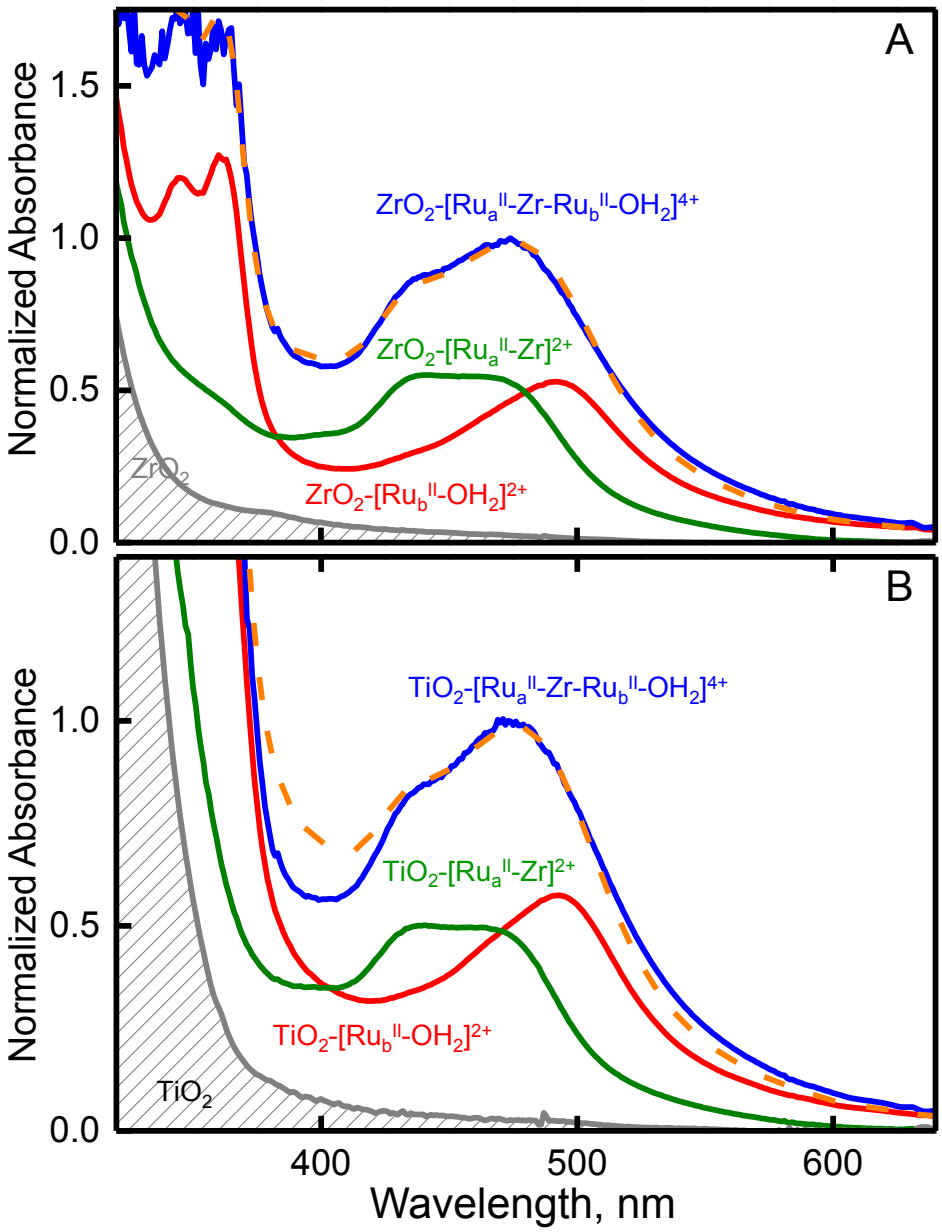

Figure 5.2. (A) Ground state absorption spectra of 3 μm ZrO_2 (grey), ZrO_2-[Ru_a^{II}-Zr]$^{2+}$ (green), ZrO_2-[Ru_b^{II}-OH_2]$^{4+}$ (red), ZrO_2-[Ru_a^{II}-Zr-Ru_b^{II}-OH_2]$^{4+}$ (blue), and the sum of ZrO_2-[Ru_a^{II}-Zr]$^{2+}$ and ZrO_2-[Ru_b^{II}-OH_2]$^{2+}$ (dashed orange). (B) Ground-state absorption spectra for 3 μm TiO_2 film (grey), TiO_2-[Ru_a^{II}-Zr]$^{2+}$ (green), TiO_2-[Ru_b^{II}-OH_2]$^{2+}$ (red), TiO_2-[Ru_a^{II}-Zr-Ru_b^{II}-OH_2]$^{4+}$ (blue), and the sum of TiO_2-[Ru_a^{II}-Zr]$^{2+}$ and TiO_2-[Ru_b^{II}-OH_2]$^{2+}$ (dashed orange). All samples are in aqueous 0.1 M $HClO_4$, 25 °C.

5.3.2. Electron Injection

5.3.2.1. Chromophore Excited-State Injection, TiO_2-$[Ru_a^{II}$-Zr$]^{2+}$

The transient absorption spectrum 1 ps after photoexcitation of TiO_2-$[Ru_a^{II}]^{2+}$ exhibits $\pi \rightarrow \pi^*$ excited-state absorptions at 380 nm and 500 nm, as well as the ^{1}MLCT ground-state beach (400 - 500 nm), Figure 5.3A. The decay of the excited-state absorption occurs with only a slight loss of the ground-state bleach. While the decay of the bleach is indicative of replenishment of the ground-state population on the picosecond time scale, presumably through rapid back electron transfer, this process is much slower and occurs to a lesser extent compared to loss of the excited-state absorption, indicating that the spectral evolution is due primarily to electron injection from $[Ru_a^{II}*]^{2+}$ into TiO_2. The rate for electron injection into TiO_2, which is given by the decay of this absorption band (Figure 5.3B), is multiexponential, with both fast (13 ps) and slow (130 ps) components. In addition to the slow decay components, there is also an ultrafast component to the injection (<100 fs) that occurs within our instrument response, and as a result is not observed; however, it has been reported by other groups for similar systems.[18] The distribution of injection times is due to the range of processes that occur upon photoexcitation. Rapid electron injection occurs from the initially formed ^{1}MLCT, or vibrationally "hot" ^{3}MLCT states, while the slower components correspond to injection from the thermally equilibrated ^{3}MLCT excited-state.[19-20]

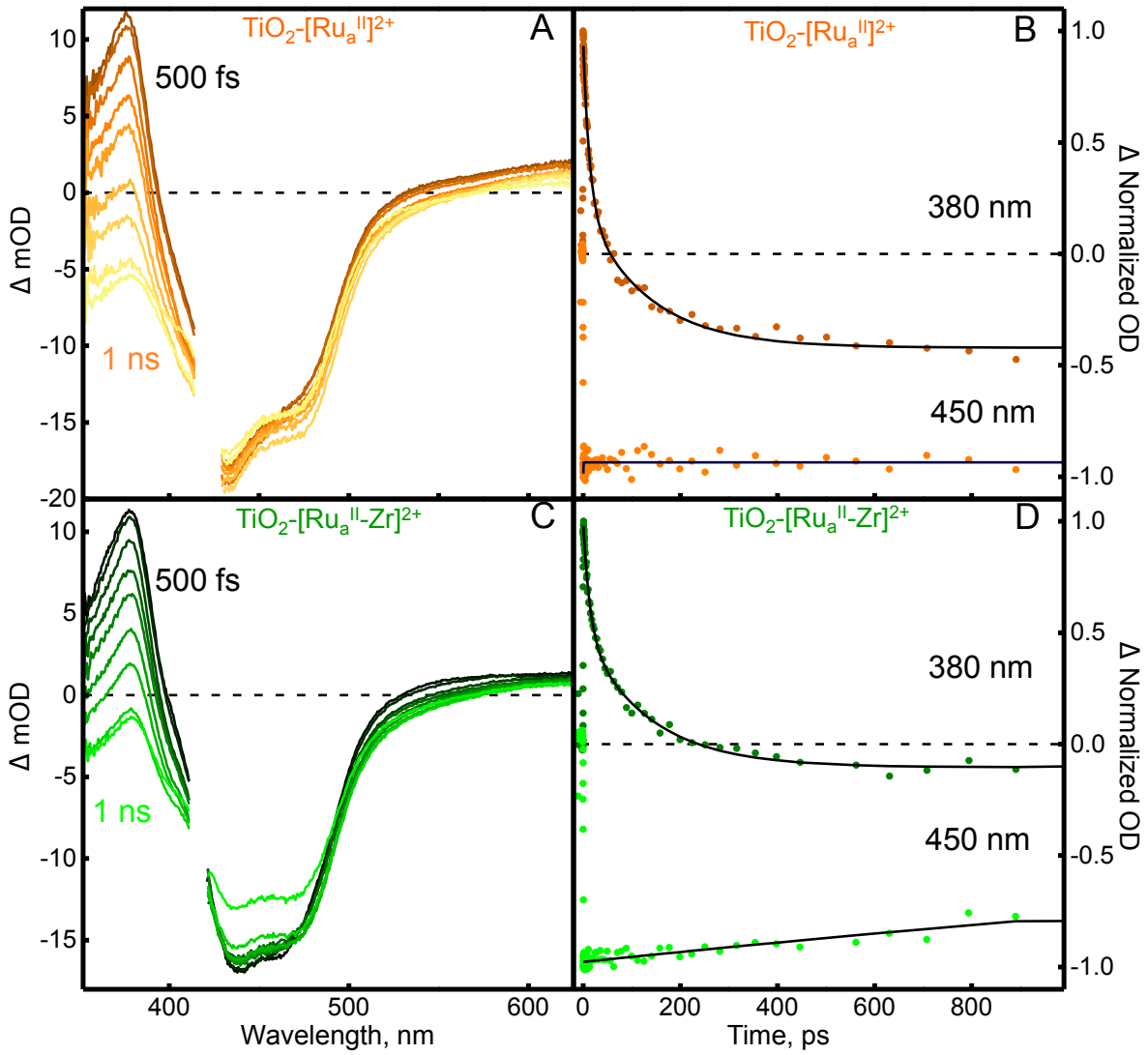

Figure 5.3. Transient absorption spectra of (A) TiO_2-$[Ru_a^{II}]^{2+}$ at 500 fs (dark line), 1 ps, 5 ps, 10 ps, 20 ps, 50 ps, 100 ps, 500 ps, and 1 ns (light line) after laser excitation. (B) Transient absorption kinetics for TiO_2-$[Ru_a^{II}]^{2+}$ at 380 nm (dark) and 450 nm (light). (C) Transient absorption spectra of TiO_2-$[Ru_a^{II}$-$Zr]^{2+}$ at 500 fs (dark line) 1 ps, 5 ps, 10 ps, 20 ps, 50 ps, 100 ps, 500 ps, and 1 ns (light line) after laser excitation. (D) Transient absorption kinetics for TiO_2-$[Ru_a^{II}$-$Zr]^{2+}$ at 380 nm (dark) and 450 nm (light). The fits are shown in black and are summarized in Table 5.1. All samples were in aqueous 0.1 M $HClO_4$ at 25 °C. The excitation wavelength was 420 nm.

Table 5.1. Summary of the multiexponential fits of TiO_2-$[Ru_a^{II}]^{2+}$ and TiO_2-$[Ru_a^{II}$-$Zr]^{2+}$.

		A_1	k_1, x10^9 s^{-1} (τ_1, ps)	A_2	k_1, x10^9 s^{-1} (τ_1, ps)	Offset
TiO_2-$[Ru_a^{II}]^{2+}$	380 nm	0.77 ± 0.04	75.93 ± 6.00 (13.17 ± 1.04)	0.66 ± 0.04	7.70 ± .79 (129.85 ± 13.39)	-0.45 ± 0.01
	460 nm	-1.00 ± 0.01	0.0132 ± 0.0172 (76000 ± 99000)	--	--	--
TiO_2-$[Ru_a^{II}$-$Zr]^{2+}$	380 nm	0.50 ± 0.03	70.17 ± 5.48 (14.25 ± 1.11)	0.61 ± 0.02	7.35 ± 0.57 (136.15 ± 10.62)	-0.11 ± 0.01
	460 nm	1.00 ± 0.01	0.2319 ± 0.015 (4312 ± 282)	--	--	--

Addition of the Zr^{4+} ions, which coordinate to the unbound phosphonate groups, alters the decay of the 380 nm band (Figure 5.3D). Fits of the decay to a biexponential function show the primary difference is in the relative amplitudes of the two components, as opposed to their time constants (τ_1 = 14 ps and τ_2 = 130 ps), which are similar to those observed for TiO_2-$[Ru_a^{II}]^{2+}$ (Table 5.1). While it is difficult to quantify the injection rate given the multiexponential nature of the decay, our observations show, at least qualitatively, that the average rate for electron injection is decreased upon coordination of Zr^{4+} to the remote phosphonate groups.

The origin of this affect may stem from the heteroleptic nature of the chromophore. Upon photoexcitation, the excited-state is distributed amongst the three ligands, whose energies differ due to different chemical substituents. For example, the electron withdrawing phosphonate groups on the pbpy ligand stabilize its energy by about 200 mV relative to bpy. This results in a driving force for transfer of MLCT excited-states located on the bpy ligand

to pbpy ligands attached to the metal oxide surface. The slower injection observed in the presence of the Zr^{4+} ions may stem from a stabilization of the pbpy ligand energy upon coordination with Zr^{4+}. If the energy order is reversed (i.e. ancillary ligand is lower in energy than the surface bound ligand), then MLCT states that become trapped on the outer pbpy ligands must either inject remotely[21-22] or first undergo interligand excitation transfer,[23] slowing down the injection process.

5.3.2.2. Injection Efficiency

Injection efficiencies are estimated by comparing amplitudes of the 380 nm $bpy^{\bullet-}$ absorption relative to the ground state bleach. The former provides a measure of the TiO_2-$[Ru_a^{II}*\text{-}Zr]^{2+}$ population as a function of time, while the latter reflects the total number of photoexcitation events giving either TiO_2-$[Ru_a^{II}*\text{-}Zr]^{2+}$ or $TiO_2(e^-)$-$[Ru_a^{III}\text{-}Zr]^{3+}$. The maximum amplitude of the excited state absorption (relative to the bleach) is observed when Φ_{inj} = 0%. This is determined from the transient absorption spectrum on ZrO_2 (i.e. ZrO_2-$[Ru_a^{II}\text{-}Zr]^{2+}$), where injection is not favorable due to the relatively high conduction band of ZrO_2 (Figure 5.4). As injection proceeds, the amplitude of this band decreases, reaching a minimum when Φ_{inj} = 100%, at which point the transient spectrum corresponds to $TiO_2(e^-)$-$[Ru_a^{III}\text{-}Zr]^{3+}$. Since the oxidized chromophore is nearly colorless, its primary contribution to the transient spectrum will be the ground state bleach, which we have approximated as the inverse of the ground state absorption.[9]

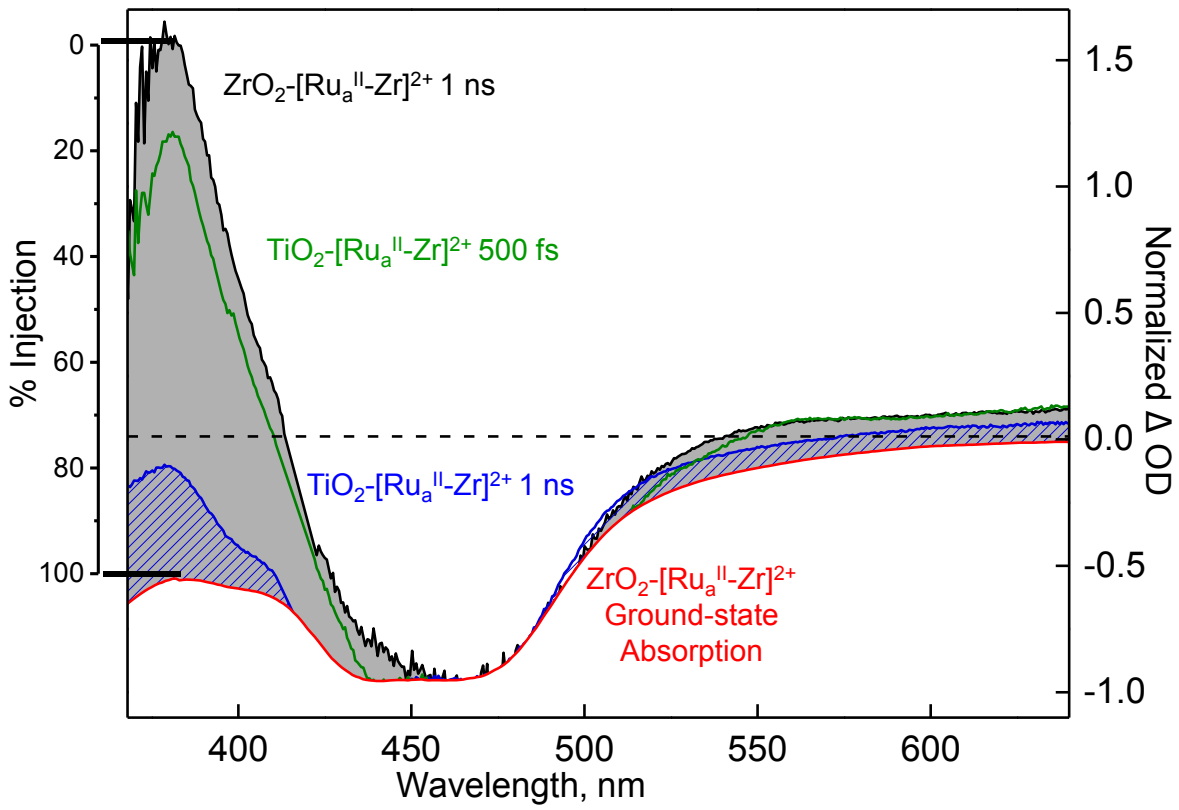

Figure 5.4. Electron injection efficiency for TiO_2-[Ru_a^{II}-Zr]$^{2+}$ is calculated from the ratio of the difference between the transient absorption amplitudes at 380 nm of [Ru_a^{II}-Zr]$^{2+}$ on TiO_2 (blue) and ZrO_2 (black) at 1 ns and the difference between amplitudes of ZrO_2 at 1 ns (black) and the inverse of the ground state absorption on ZrO_2 (red) at 380 nm. The electron injection efficiency for TiO_2-[Ru_a^{II}-Zr]$^{2+}$ is 81%. The amount of ultrafast injection is 17% from the ratio of ZrO_2-[Ru_a^{II}-Zr]$^{2+}$ (black) and TiO_2-[Ru_a^{II}-Zr]$^{2+}$ at 500 fs (green).

The transient absorption spectrum for surface-bound TiO_2-[Ru_a^{II}-Zr]$^{2+}$ at long delay times lies between the spectra for TiO_2-[Ru_a^{II}*-Zr]$^{2+}$ and TiO_2-[Ru_a^{III}-Zr]$^{2+}$ with its relative position reflecting the overall injection efficiency. The electron injection efficiency for TiO_2-[Ru_a^{II}-Zr]$^{2+}$ is estimated in this manner to be 81% at 1 ns. Also depicted in the figure is the transient spectrum observed at 500 fs, whose amplitude of the excited state absorption suggests that 17% of the injection events occur within the first 500 fs. Similar measurements

made in the absence of the Zr^{4+} ions (i.e. for TiO_2-$[Ru_a^{II}]^{2+}$) yield higher injection efficiencies (95% overall, and 20% ultrafast). These results indicate that the coordination of the Zr^{4+} ions to the phosphonate groups result not only in slower injection times, but also lower injection yields.

Calculating injection efficiencies in this manner is based on two assumptions. The first is that oxidized chromophore, $TiO_2(e^-)$-$[Ru_a^{III}$-$Zr]^{3+}$, does not contribute to the signal at 380 nm. This is a reasonable assumption given that $[Ru^{III}(bpy)_3]^{3+}$ is only weakly absorbing throughout the visible and near UV. Nevertheless, an excited-state absorption contribution to the transient signal at 380 nm from $TiO_2(e^-)$-$[Ru_a^{III}$-$Zr]^{3+}$ would make the efficiency appear smaller relative to its actual value. Second, it is assumed that the amplitude of the bleach signal at 450 nm is a good measure of the population of photoexcited chromophores. This requires that the excited state absorption of the chromophore does not contribute to the bleach signal at 450 nm. If the excited state were contributing at 450 nm, then there should be an increase in the bleach amplitude coinciding with electron injection. This is not observed in either system, suggesting that both assumptions hold.

5.3.2.3. Catalyst Injection

The transient absorption spectra of the assembly, TiO_2-$[Ru_a^{II}$-Zr-Ru_b^{II}-$OH_2]^{4+}$ also show a decay of the 380 nm excited state absorption on the picosecond time scale (Figure 5.5). Because of the structure of the bilayer, it is possible that upon photoexcitation, the catalyst either injects remotely, or some fraction is bound to the TiO_2 and undergoes direct injection.

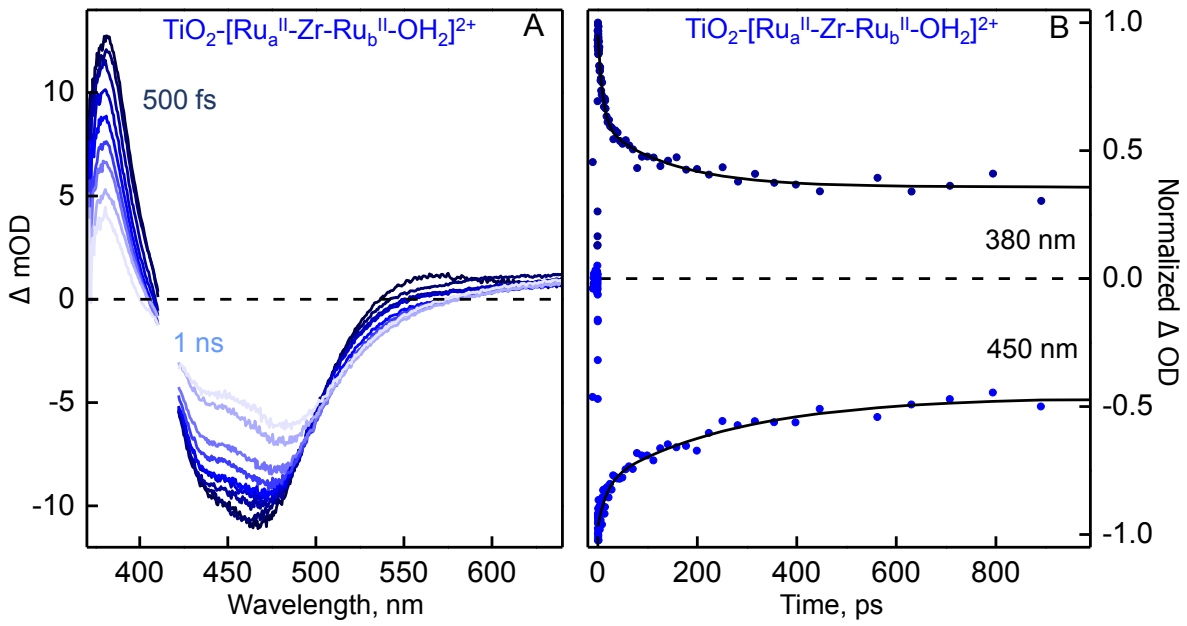

Figure 5.5. Transient absorption spectra of (A) TiO_2-[Ru_a^{II}-Zr-Ru_b^{II}-OH_2]$^{4+}$ at 500 fs (dark line), 1 ps, 5 ps, 10 ps, 20 ps, 50 ps, 100 ps, 500 ps, and 1 ns (light line) after laser excitation. (B) Transient absorption kinetics for [Ru_a^{II}-Zr-Ru_b^{II}-OH_2]$^{4+}$ on TiO_2 at 380 nm (dark) and 450 nm (light). The fits are shown in black and are summarized in Table 5.2. All samples were in aqueous 0.1 M $HClO_4$ at 25 °C. The excitation wavelength was 420 nm.

Table 5.2. Summary of the multiexponential fits of TiO_2-[Ru_a^{II}-Zr-Ru_b^{II}-OH_2]$^{4+}$.

	A_1	k_1, x10^9 s^{-1} (τ_1, ps)	A_2	k_2, x10^9 s^{-1} (τ_2, ps)	Offset
380 nm	0.38 ± 0.02	101.4 ± 12.76 (9.86 ± 1.24)	0.26 ± 0.02	7.00 ± 1.52 (142.76 ± 31.04)	0.37 ± 0.01
460 nm	0.18 ± 0.03	55.91 ± 18.03 (17.89 ± 5.77)	0.35 ± 0.03	3.67 ± 1.04 (272.33 ± 77.06)	0.47 ± 0.03

The transient absorption spectrum of the assembly at 1 ps after excitation, TiO_2-[Ru_a^{II}-Zr-Ru_b^{II}-OH_2]$^{4+}$ can be described as the sum of TiO_2-[Ru_a^{II}-Zr]$^{2+}$ and ZrO_2-[Ru_b^{II}-OH_2]$^{2+}$ spectra, (Figure 5.6). Because the catalyst cannot inject into ZrO_2, the

ZrO_2-[Ru_b^{II}-OH_2]$^{2+}$ transient spectrum reflects solely the catalyst excited-state. The fact that the catalyst contribution to the transient spectra of TiO_2-[Ru_a^{II}-Zr-Ru_b^{II}-OH_2]$^{4+}$ can be accounted for entirely by using the spectrum of ZrO_2-[Ru_b^{II}-OH_2]$^{2+}$ is consistent with electron injection into TiO_2 only from the excited-state of the chromophore [Ru_a^{II}]$^{2+}$, with little or no contribution from photoexcited catalysts.

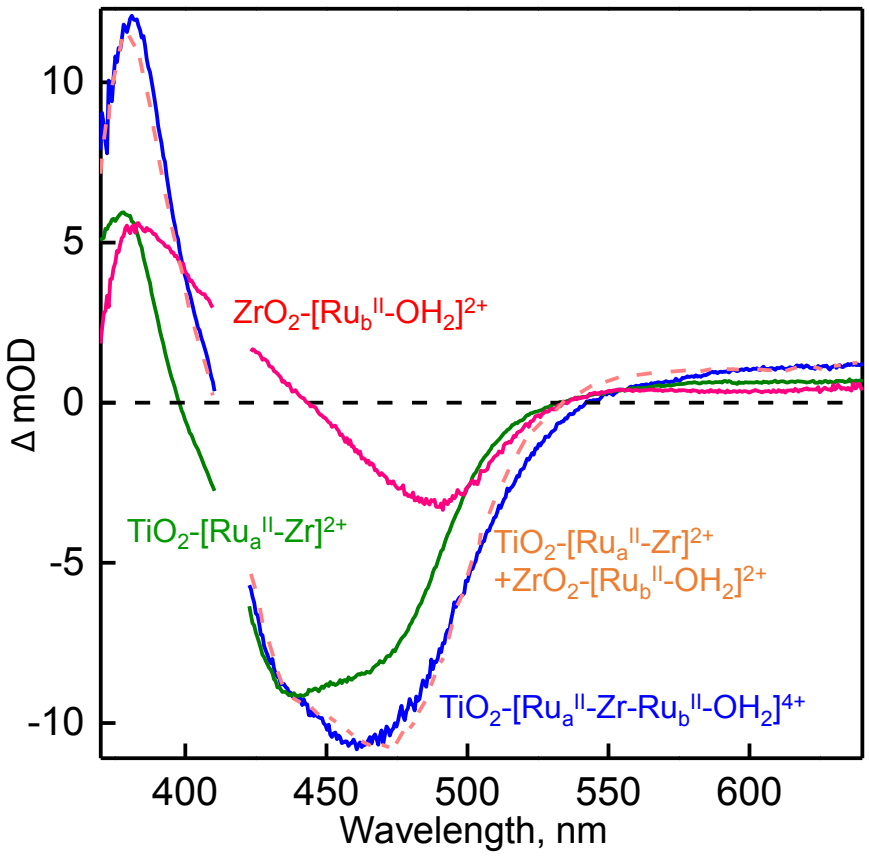

Figure 5.6. Transient absorption spectra 1 ps after photoexcitation of TiO_2-[Ru_a^{II}-Zr]$^{2+}$ (green), TiO_2-[Ru_a^{II}-Zr-Ru_b^{II}-OH_2]$^{4+}$ (blue), TiO_2-[Ru_b^{II}-OH_2]$^{2+}$ (red) and the sum of TiO_2-[Ru_a^{II}-Zr]$^{2+}$ and TiO_2-[Ru_b^{II}-OH_2]$^{2+}$ (dashed orange). All samples were on 3 μm thick nanocrystalline TiO_2 films in aqueous 0.1 M $HClO_4$ at 25 °C. The excitation wavelength was 420 nm.

5.3.3. Catalyst Excited-State Decay

The catalyst $[Ru_b^{II}\text{-}OH_2]^{2+}$ excited-state is best seen on ZrO_2 film where electron injection is unfavorable. The transient absorption spectra of $ZrO_2\text{-}[Ru_b^{II}\text{-}OH_2]^{2+}$ has the expected ground-state bleach centered at 490 nm and excited-state absorptions at 380 nm and 550 nm similar to $TiO_2\text{-}[Ru_a^{II}]^{2+}$ (Figure 5.7A). The major difference in the excited-state spectra of the catalyst $[Ru_b^{II}\text{-}OH_2]^{2+}$, when compared to the chromophore $[Ru_a^{II}]^{2+}$, is the rate for excited-state decay. The decay of the excited-state for $ZrO_2\text{-}[Ru_b^{II}\text{-}OH_2]^{2+}$ (Figure 5.7B) is multiexponential with a fast component of 18 ps and slow component of 364 ps. The fast component is attributed to an excited-state relaxation process (e.g. vibrational relaxation or inter-ligand excitation transfer), and the long component to the catalyst excited-state lifetime.[24] The short lifetime of the catalyst indicates that excited-state decay of the catalyst is partially responsible for the decay observed in the 380 nm absorption feature in $TiO_2\text{-}[Ru_a^{II}\text{-}Zr\text{-}Ru_b^{II}\text{-}OH_2]^{4+}$.

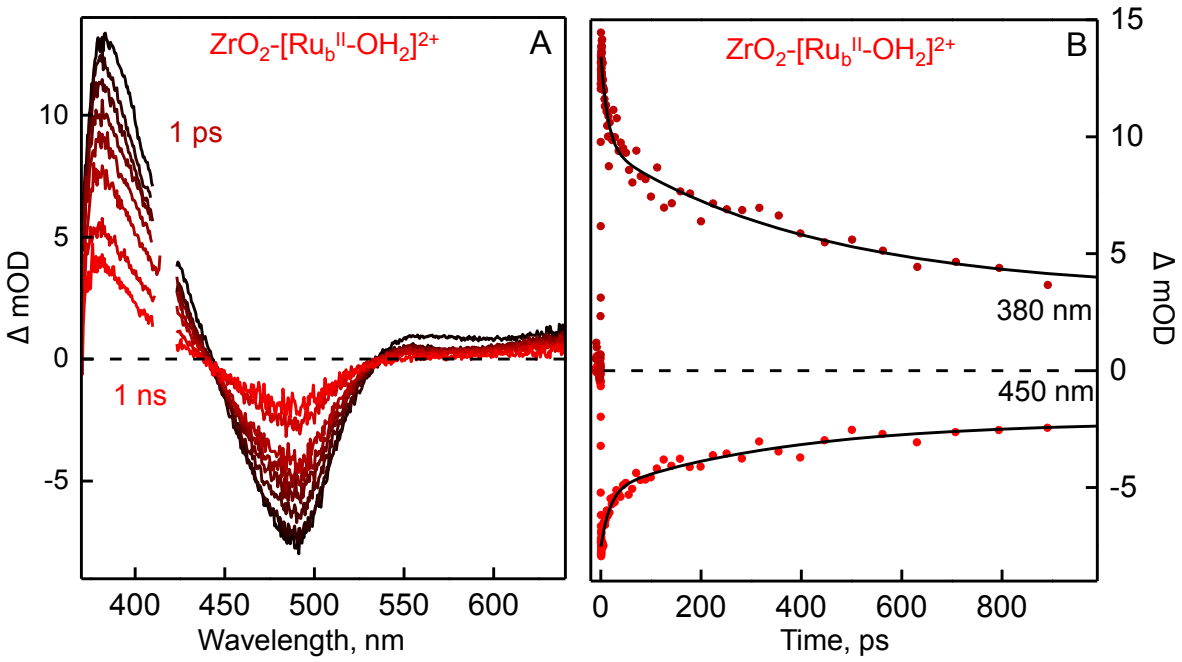

Figure 5.7. Transient absorption spectra of ZrO_2-[Ru_b^{II}-OH_2]$^{2+}$ at 1 ps (dark line), 5 ps, 10 ps, 20 ps, 50 ps, 100 ps, 500 ps, and 1 ns (light line) after laser excitation. (B) Transient absorption kinetics of ZrO_2-[Ru_b^{II}-OH_2]$^{2+}$ at 380 nm (dark) and 490 nm (light). The fit is shown with black line and summarized in Table 5.3. The sample was on 3 μm thick nanocrystalline ZrO_2 film in aqueous 0.1 M $HClO_4$ at 25 °C. The excitation wavelength was 420 nm.

Table 5.3. Summary of the multiexponential fit to the transient absorption signal for ZrO_2-[Ru_b^{II}-OH_2]$^{4+}$.

	A_1	k_1, x10^9 s^{-1} (τ_1,ps)	A_2	k_1, x10^9 s^{-1} (τ_2, ns)	Offset
380 nm	3.96 ± 0.35	71.7 ± 0.01 (13.9 ± 2.79)	6.18 ± 0.64	2.33 ± 0.71 (429.7 ± 30.71)	3.37 ± 0.79
490 nm	-2.43 ± 0.23	54.5 ± 9.64 (18.3 ± 3.25)	-2.95 ± 0.25	2.75 ± 0.82 (363.6 ± 108.6)	-2.18 ± 0.32

5.3.4. Energy Transfer

The photoexcited chromophore can undergo energy transfer to the catalyst (Scheme 5.1, Eq. 3) and is best seen on nanocrystalline ZrO_2. Figure 5.8A shows steady-state emission spectra for ZrO_2-$[Ru_a^{II}$-$Zr]^{2+}$ (centered at 650 nm), ZrO_2- $[Ru_b^{II}$-$OH_2]^{2+}$ (centered at 700 nm), and ZrO_2-$[Ru_a^{II}$-Zr-Ru_b^{II}-$OH_2]^{4+}$ (centered at 660 nm), each normalized to its emission maximum. The emission spectrum of the assembly is considerably weaker and broadened on the lower energy side relative to the chromophore (ZrO_2-$[Ru_a^{II}$-$Zr]^{2+}$). Time-resolved emission measurements show the lifetime of the assembly to be 20 ns, Figure 5.8B. This is considerably shorter than that of the chromophore (450 ns), indicating the presence of an added mechanism for excited-state quenching. Given the broadening of the emission band to the red, we attribute the quenching to energy transfer from the chromophore $[Ru_a^{II}*]^{2+}$ to the catalyst $[Ru_b^{II}$-$OH_2]^{2+}$ (Scheme 5.1, Eq. 3). The slow rate of this process compared to electron injection into TiO_2 (200 ps) indicates it is not a competitive excited-state deactivation pathway for the assembly on TiO_2.

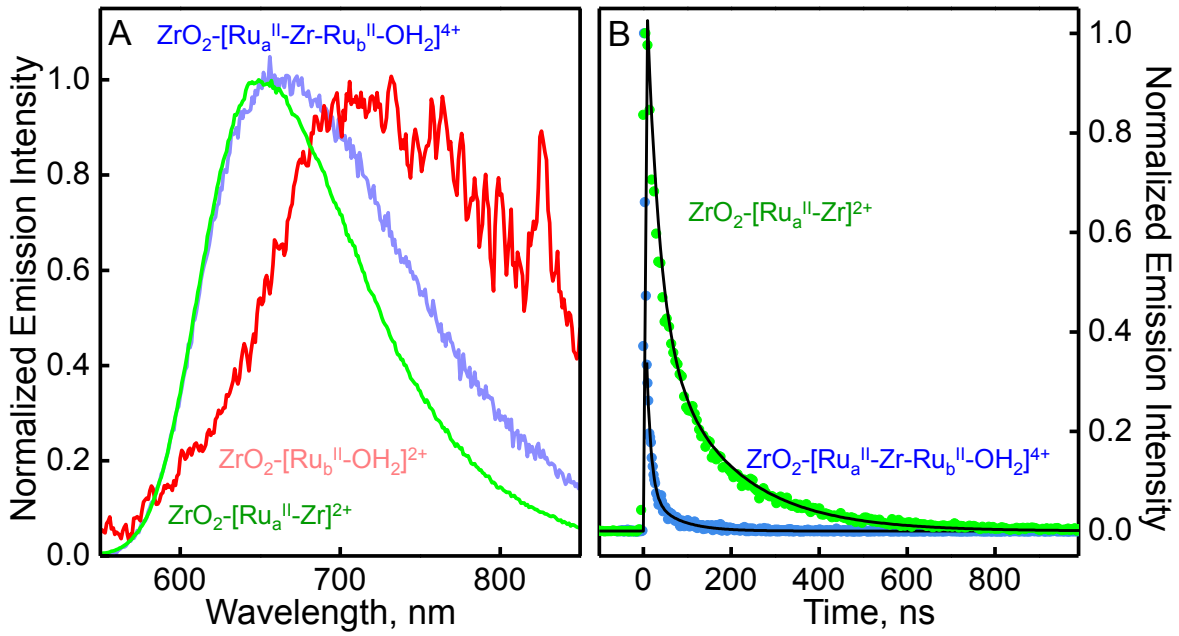

Figure 5.8. (A) Normalized steady-state emission spectra of ZrO_2-[Ru_a^{II}-Zr]$^{2+}$ (green), ZrO_2-[Ru_a^{II}-Zr-Ru_b^{II}-OH_2]$^{4+}$ (blue), and ZrO_2-[Ru_b^{II}-OH_2]$^{4+}$ (red). (B) Time-resolved emission of ZrO_2-[Ru_a^{II}-Zr]$^{2+}$ (green) and ZrO_2-[Ru_a^{II}-Zr-Ru_b^{II}-OH_2]$^{4+}$ (blue) collected at 640 nm. The fits (black lines) are summarized in Table 5.4. The samples were in quartz cuvettes containing aqueous 0.1 M $HClO_4$, 25 °C. The excitation wavelength was 450 nm.

Table 5.4. Summary of the multiexponential fits of time-resolved emission for ZrO_2-[Ru_a^{II}]$^{2+}$ and ZrO_2-[Ru_a^{II}-Zr-Ru_b^{II}-OH_2]$^{4+}$.

	A_1	k_1, x10^6 s^{-1} (τ_1,ns)	A_2	k_1, x10^6 s^{-1} (τ_2, ns)	Average k_1, x10^6 s^{-1} (<τ>, ns)
ZrO_2-[Ru_a^{II}]$^{2+}$	0.66 ± 0.01	34.5 ± 0.5 (29.0 ± 0.4)	0.34 ± 0.01	6.10 ± 0.06 (163.9 ± 1.6)	13.3 ± 0.1 (74.9 ± 0.8)
ZrO_2-[Ru_a^{II}-Zr-Ru_b^{II}-OH_2]$^{4+}$	0.87 ± 0.01	96.8 ± 1.7 (10.3 ± 0.2)	0.13 ± 0.01	16.4 ± 0.5 (61.1 ± 1.7)	59.2 ± 1.4 (16.9 ± 0.4)

5.3.5. Transfer of the Oxidative Equivalent to the Catalyst

The transient absorption spectra for TiO_2-[Ru_a^{II}-Zr-Ru_b^{II}-OH_2]$^{4+}$ differ from those of TiO_2-[Ru_a^{II}-Zr]$^{2+}$. The most notable difference is a decrease in the ground-state bleach intensity that occurs during the first nanosecond after photoexcitation (Figure 5.5). The loss of the ground-state is most likely due to the decay of the catalyst excited-state whose lifetime is 363 ps. A second clear difference is seen in the normalized transient absorption spectra of TiO_2-[Ru_a^{II}-Zr-Ru_b^{II}-OH_2]$^{4+}$ (Figure 5.9A). In this representation, there is a clear shift and broadening of the ground-state bleach to the red that begins at 10 ps and continues over the first nanosecond (Figure 5.9C). Although the chromophore bleach also broadens, it occurs to a much lesser extent (Figure 5.9B). The magnitude of the broadening is quantified in Figure 5.9C, which shows the shift in the wavelength of the red edge of the bleach (measured at the 50% point) as a function of pump-probe delay. The assembly TiO_2-[Ru_a^{II}-Zr-Ru_b^{II}-OH_2]$^{4+}$ has a shift of 20 nm in the red edge of the bleach, whereas the chromophore, TiO_2-[Ru_a^{II}-Zr]$^{2+}$, only shifts by 5 nm (Figure 5.9C). This broadening occurs with both a fast component (18 ps), also seen in the shift of the chromophore, and slow component (135 ps). The slow component is attributed to the transfer of the oxidative equivalent to the catalyst.

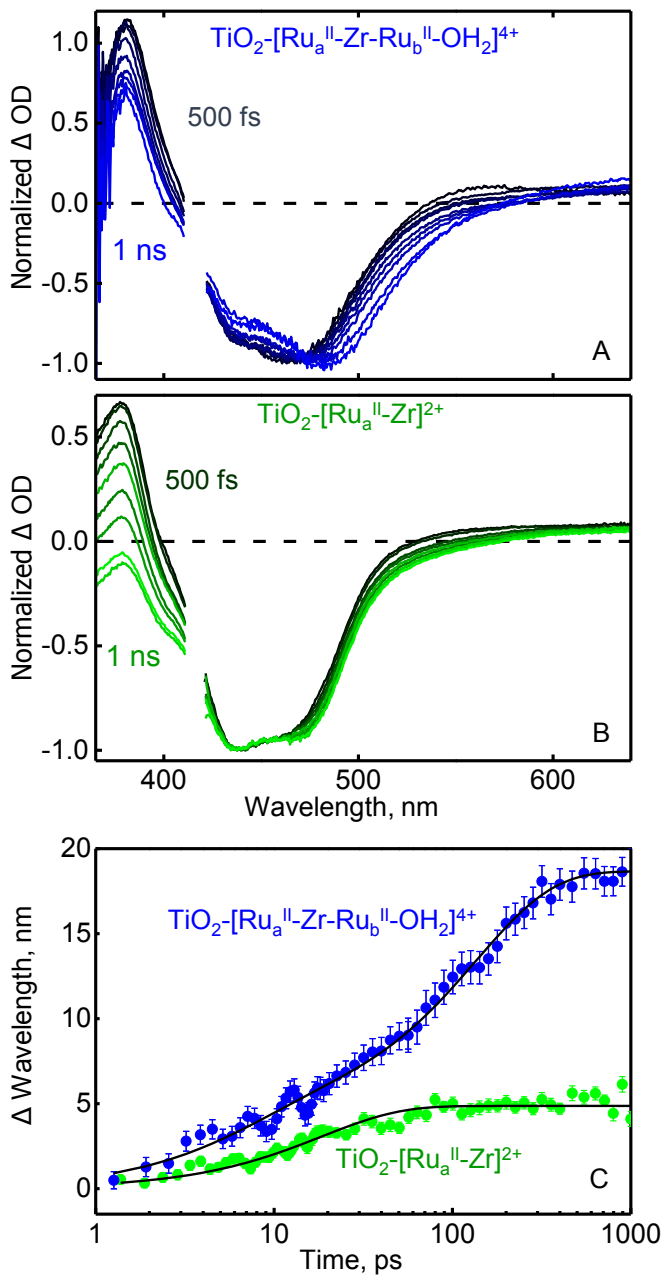

Figure 5.9. Normalized transient absorption spectra of (A) TiO_2-[Ru_a^{II}-Zr-Ru_b^{II}-OH_2]$^{4+}$ and (B) TiO_2-[Ru_a^{II}-Zr]$^{2+}$ at 500 fs (dark line), 1 ps, 5 ps, 10 ps, 20 ps, 50 ps, 100 ps, 500 ps, and 1 ns (light line) after laser excitation. (C) Change in red wavelength of the ground-state bleach (at the 50% point) verses time for TiO_2-[Ru_a^{II}-Zr]$^{2+}$ (green) and TiO_2-[Ru_a^{II}-Zr-Ru_b^{II}-OH_2]$^{4+}$ (blue). The fits are shown with black line and summarized in Table 5.5. All samples were in aqueous 0.1 M $HClO_4$ at 25 °C. The excitation wavelength was 420 nm.

Table 5.5. Summary of the fit for the change in red wavelength of the ground-state bleach (at the 50% point) verses time to the function $y = A_1\left(1 - e^{-\frac{t}{\tau_1}}\right) + A_2\left(1 - e^{-\frac{t}{\tau_2}}\right)$.

	A_1	τ_1 (ps)	A_2	τ_2 (ps)
TiO_2-$[Ru_a^{II}$-$Zr_2]^{2+}$	4.86 ± 0.08	18.57 ± .97	--	--
TiO_2-$[Ru_a^{II}$-Zr-Ru_b^{II}-$OH_2]^{4+}$	4.39 ± 0.31	6.52 ± 1.0	14.27 ± 0.31	135.80 ± 2.95

The overlapping spectral bands of $[-Ru_a^{II}-]^{2+}$, $[-Ru_a^{III}-]^{3+}$, $[-Ru_b^{II}-OH_2]^{2+}$ and $[-Ru_b^{III}-OH_2]^{3+}$ make it difficult to extract a rate constant for the transfer of the oxidative equivalent simply by monitoring the transient absorption signal at a single wavelength. Disentangling the contributions from each species is accomplished with a global analysis based a singular value decomposition (SVD) algorithm.

The global analysis of TiO_2-$[Ru_a^{II}$-Zr-Ru_b^{II}-$OH_2]^{4+}$ fit the transient absorption spectra from 10 ps to 5 ns to a pre-defined kinetic model. The model includes (i) electron injection into TiO_2 (Scheme 5.1, Eq. 4), (ii) transfer of the oxidative equivalent to the catalyst (Scheme 5.1, Eq. 5), and (iii) excited-state decay of the catalyst (Scheme 5.1, Eq. 2b). The other processes in Scheme 5.1 occur on timescales longer than 5 ns. Specifically the excited-state of $[Ru_a^{II}]^{2+}$ (Scheme 5.1, Eq. 2a) has a lifetime of 450 ns, the energy transfer (Scheme 5.1, Eq. 3) occurs with a lifetime of 20 ns, and the back electron transfer (Scheme 5.1, Eq. 6) occurs on the microsecond timescale.

The number of adjustable parameters in the global fit of TiO_2-$[Ru_a^{II}$-Zr-Ru_b^{II}-$OH_2]^{4+}$ were reduced by incorporating several key constraints to the spectra and rate constants, summarized in Table 5.6. The rate for electron injection (Scheme 5.1 Eq. 4), transient spectra for the chromophore excited-state ($[-Ru_a^{II}*-]^{2+}$) and oxidized chromophore ($[-Ru_a^{III}-]^{3+}$) were

obtained separately by performing a similar analysis on the chromophore control, TiO_2-[Ru_a^{II}-Zr]$^{2+}$ (Figure 5.10).

In the analysis of the chromophore control, the spectrum of [-Ru_a^{II}*-]$^{2+}$ was fixed to the spectrum of TiO_2-[Ru_a^{II}-Zr]$^{2+}$ at 500 fs. The initial concentrations of [-Ru_a^{II}*-]$^{2+}$ and [-Ru_a^{III}-]$^{3+}$ are based on the injection efficiency described above. Specifically, the initial concentrations of [-Ru_a^{II}*-]$^{2+}$ and [-Ru_a^{III}-]$^{3+}$ were set to 0.67 and 0.14 to account for the loss of 17% of the injecting chromophores during the instrument response. The model also accounted for the 19% of chromophores that do not inject during the first nanosecond. The fit results in an electron injection rate of $k = 1.1 \times 10^{11}$ s^{-1} (9 ps), and spectra shown in Figure 5.10A. It is important to note that the calculated [-Ru_a^{III}-]$^{3+}$ spectrum is in reasonable agreement with the ΔA ([Ru^{II}]$^{2+}$/[Ru^{III}]$^{3+}$) spectrum measured spectroelectrochemicaly (Figure 5.10A), with a broadening of the ground-state bleach to red. The global analysis is limited to describing the injection with a single average rate constant, and thus cannot reproduce the kinetic complexity observed in the transient data. Nevertheless, it represents a reasonable description of the injection kinetics and was used for the injection rate in the analysis of the assembly.

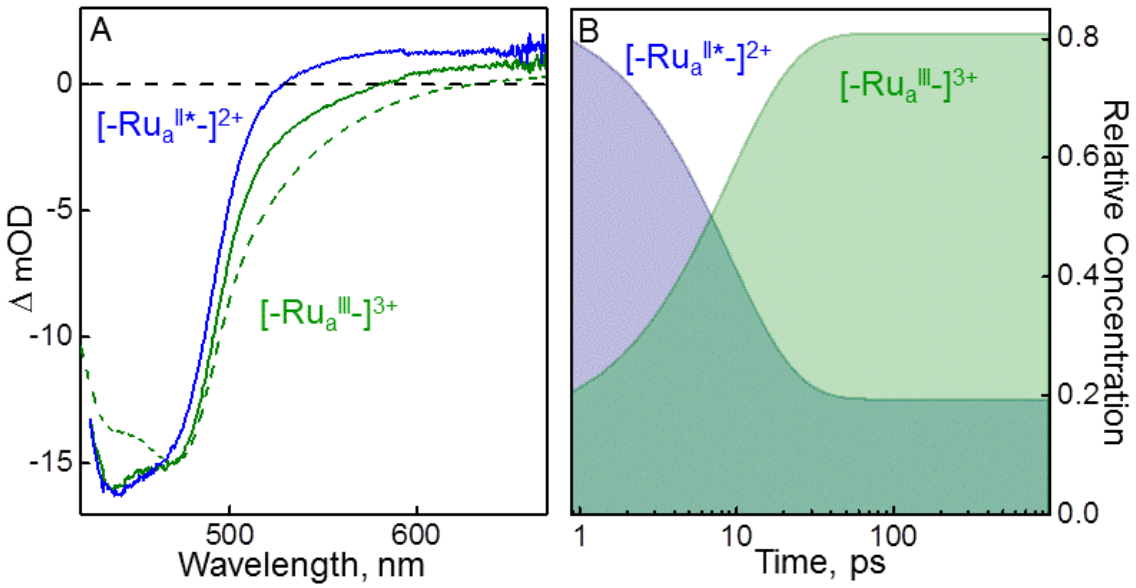

Figure 5.10. Global Analysis following excitation of TiO_2-[Ru_a^{II}-Zr]$^{2+}$. (A) The spectra of [-Ru_a^{II}*-]$^{2+}$ (blue), [-Ru_a^{III}-]$^{3+}$ (green), and measured ΔA ([Ru^{II}]$^{2+}$/[Ru^{III}]$^{3+}$) (green dashed). (B) Relative concentration of [-Ru_a^{II}*-]$^{2+}$ (blue) and [-Ru_a^{III}-]$^{3+}$ (green) verse time. The residuals are shown in Figure 5.11.

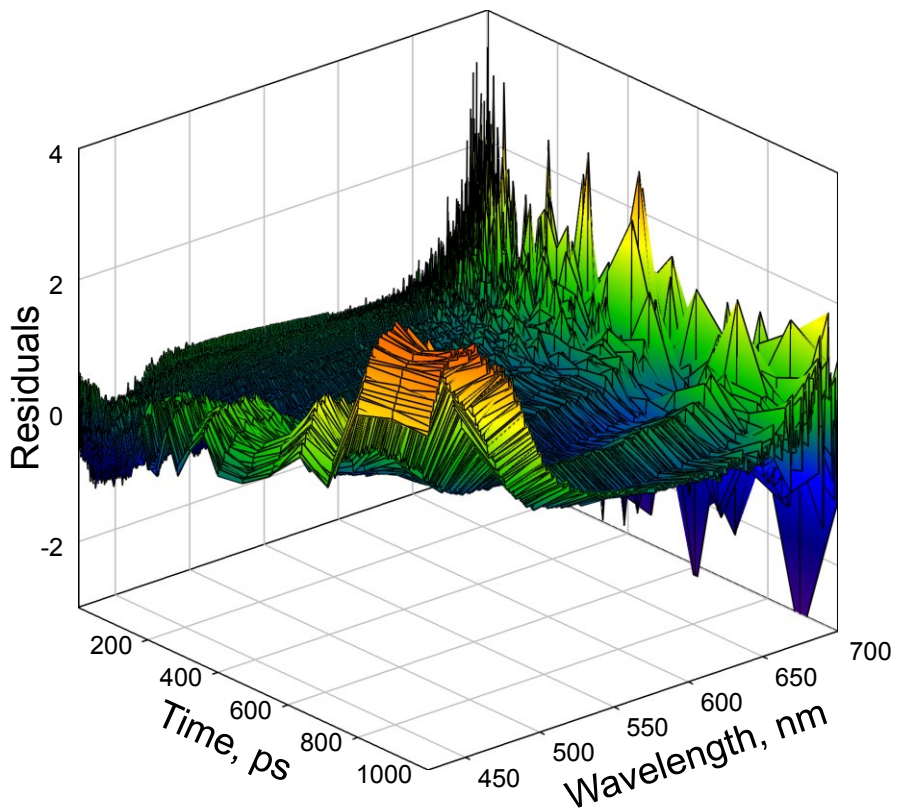

Figure 5.11. Residuals from the global analysis of TiO_2-$[Ru_a^{II}$-Zr$]^{2+}$.

The initial conditions for the global analysis also fixed the spectra for $[-Ru_a^{II}*-]^{2+}$, $[-Ru_a^{III}-]^{3+}$, and $[-Ru_b^{II}*-OH_2]^{2+}$ (Table 5.6). The initial concentrations in Table 5.6 account for the chromophore to catalyst ratio of 1:1.5 (discussed above) and their relative molar absorptivities (0.68 and 0.32). The fit also takes into account the ultrafast injection yield of the chromophore, which results in the presence of oxidized chromophore ($[Ru_a^{III}]^{3+}$) in the instrument response, as well as the overall injection yield (81 %). The only adjustable parameters in the global analysis are the spectra of $[-Ru_b^{II}*-OH_2]^{2+}*$ and $[-Ru_b^{III}-OH_2]^{3+}$, and the rate for transfer of the oxidative equivalent to the catalyst (Scheme 5.1, Eq. 5).

The spectra that result from the global analysis are shown in Figure 5.12A. The spectrum of $[-Ru_a^{III}-]^{3+}$ and $[-Ru_b^{III}-OH_2]^{3+}$ closely resemble the calculated ΔA spectra for

($[Ru_a^{II}]^{2+}/[Ru_a^{III}]^{3+}$) and ($[Ru_b^{II}\text{-}OH_2]^{2+}/[Ru_b^{III}\text{-}OH_2]^{3+}$). The relative concentration profiles of each species are shown in Figure 5.12B. The fit resulted in a calculated rate constant for the transfer of the oxidative equivalent to the catalyst of $k = 5.9 \times 10^9\ s^{-1}$ (170 ps). The efficiency for the transfer of the oxidative equivalent is nearly 100% (based on relative lifetimes), but the overall efficiency of the assembly is 43% due to non-productive photoexcitation of the catalyst and incomplete electron injection from the chromophore.

Table 5.6. Summary of global analysis constraint and initial/final concentration.

Chemical Species	Spectral Contribution	Initial	Final
Chromophore Excited-state, $[\text{-}Ru_a^{II}*\text{-}]^{2+}$	Fixed[(a)]	0.46	0.10[(c)]
Oxidized Chromophore, $[\text{-}Ru_a^{III}\text{-}]^{3+}$	Fixed[(a)]	0.07	0.00
Catalyst Excited-state, $[\text{-}Ru_b^{II}*\text{-}OH_2]^{2+}$	Fixed[(b)]	0.47	0.00
Oxidized Catalyst, $[\text{-}Ru_b^{III}\text{-}OH_2]^{3+}$	Adjustable	0.00	0.43
Ground-state	Non absorptive	0.00	0.47[(d)]
Dynamical Process	Rate Constant		
Electron Injection, Eq. 4	Fixed[(a)]	$(9\ ps)^{-1}$	
Oxidative transfer, Eq. 5	Adjustable	$(170\ ps)^{-1}$	
Catalyst Excited-state Decay, Eq 2B	Fixed[(b)]	$(363\ ps)^{-1}$	

(a) From SVD analysis of $TiO_2\text{-}[Ru_a^{II}\text{-}Zr]^{2+}$.

(b) Transient absorption spectra at 500 fs of $ZrO_2\text{-}[Ru_b^{II}\text{-}OH_2]^{2+}$, Figure 5.7A.

(c) Accounts for $[\text{-}Ru_a^{II}*\text{-}]^{2+}$ population that does not inject during first 1 ns, based on injection efficiency measurements.

(d) Final concentration represents fraction of directly excited catalysts.

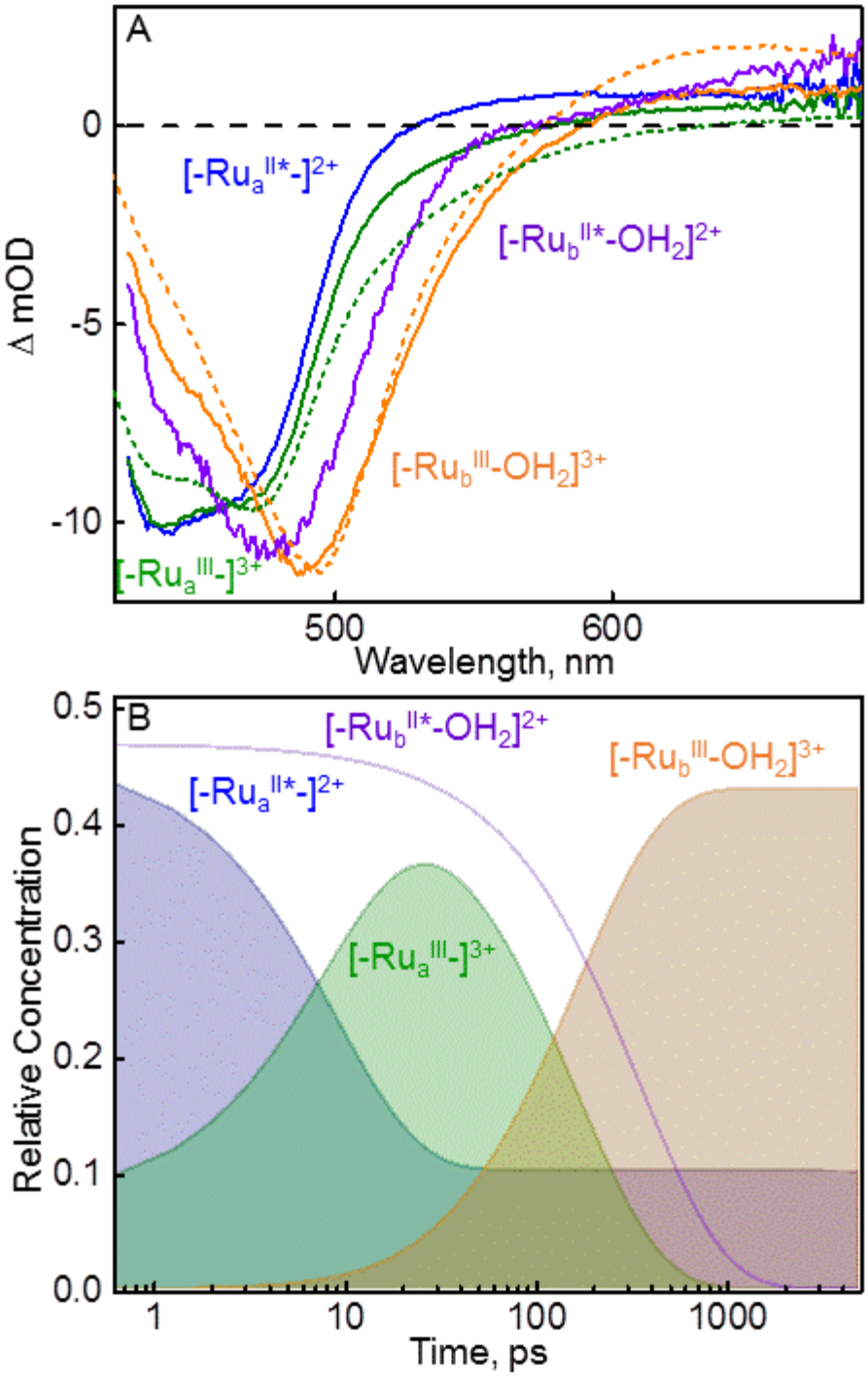

Figure 5.12. Global analysis following excitation of TiO_2-[Ru$_a^{II}$-Zr-Ru$_b^{II}$-OH$_2$]$^{4+}$. (A) The spectra of [-Ru$_a^{II}$*-]$^{2+}$ (blue), [-Ru$_a^{III}$-]$^{3+}$ (green), [-Ru$_b^{II}$*-OH$_2$]$^{2+}$ (purple), [-Ru$_b^{III}$-OH$_2$]$^{3+}$ (orange) and measured ΔA for [Ru$_a^{II}$]$^{2+}$/[Ru$_a^{III}$]$^{3+}$ (dashed green) and [Ru$_b^{II}$-OH$_2$]$^{2+}$/[Ru$_b^{III}$-OH$_2$]$^{3+}$ (dashed orange). (B) Relative concentration of [-Ru$_a^{II}$*-]$^{2+}$

(blue), $[-Ru_a^{III}-]^{3+}$ (green), $[-Ru_b^{II}*-OH_2]^{2+}$ (purple) and $[-Ru_b^{III}-OH_2]^{3+}$ (orange) verses time. The residuals are shown in Figure 5.13.

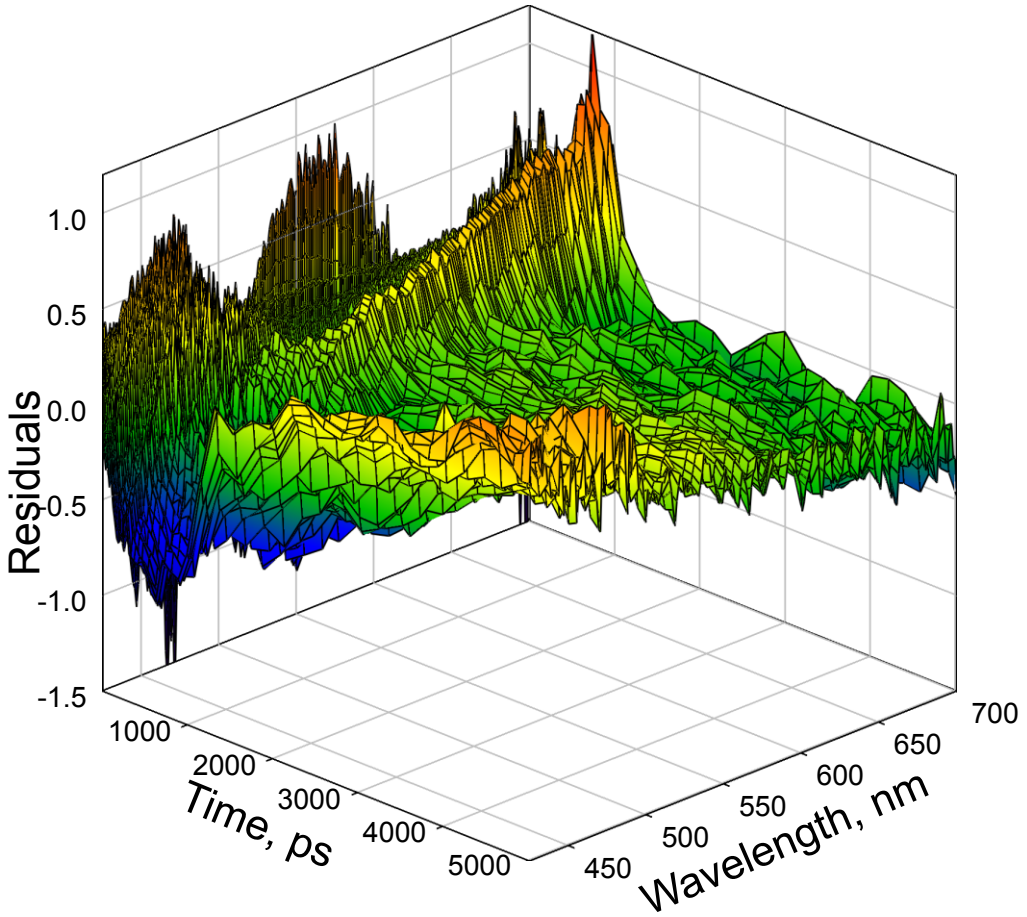

Figure 5.13. Residuals from the global analysis of TiO_2-$[Ru_a^{II}$-Zr-Ru_b^{II}-$OH_2]^{4+}$.

5.4. CONCLUSIONS

A "layer-by-layer" scaffold containing a phosphonated $[Ru(bpy)_3]^{2+}$ chromophore and a $[Ru(bpy)(Mebimpy)(OH_2)]^{2+}$ water oxidation catalyst was loaded onto nanoporous TiO_2 and the first photoactivation step in the DSPEC was analyzed using femtosecond transient absorption spectroscopy. Upon photoexcitation the chromophore undergoes picosecond electron injection into TiO_2 followed by transfer of the oxidative equivalent to the catalyst. A global analysis of the transient absorption spectra reveals a rate for the transfer of

the oxidative equivalent to the catalyst of $k = 5.9 \times 10^9\ s^{-1}$ (170 ps). The efficiency for the transfer of the oxidative equivalent to the catalyst was found to be nearly 100% with an overall efficiency for the assembly of 43%. This "layer-by-layer" architecture is an effective scaffold for DSPECs with its ability to position the chromophore and catalyst on a nanocrystalline TiO_2 surface in close proximity.

REFERENCES

(1) Alstrum-Acevedo, J. H.; Brennaman, M. K.; Meyer, T. J. Inorg. Chem. 2005, 44, 6802-6827.

(2) Lewis, N. S.; Nocera, D. G. Proceedings of the National Academy of Sciences 2006, 103, 15729-15735.

(3) Ashford, D. L.; Song, W.; Concepcion, J. J.; Glasson, C. R. K.; Brennaman, M. K.; Norris, M. R.; Fang, Z.; Templeton, J. L.; Meyer, T. J. J. Am. Chem. Soc. 2012, 134, 19189-19198.

(4) Li, F.; Jiang, Y.; Zhang, B.; Huang, F.; Gao, Y.; Sun, L. Angew. Chem. Int. Ed. 2012, 51, 2417-2420.

(5) Ma, D.; Bettis, S. E.; Hanson, K.; Minakova, M.; Alibabaei, L.; Fondrie, W.; Ryan, D. M.; Papoian, G. A.; Meyer, T. J.; Waters, M. L.; Papanikolas, J. M. J. Am. Chem. Soc. 2013, 135, 5250-5253.

(6) Norris, M. R.; Concepcion, J. J.; Harrison, D. P.; Binstead, R. A.; Ashford, D. L.; Fang, Z.; Templeton, J. L.; Meyer, T. J. J. Am. Chem. Soc. 2013, 135, 2080-2083.

(7) Song, W.; Glasson, C. R. K.; Luo, H.; Hanson, K.; Brennaman, M. K.; Concepcion, J. J.; Meyer, T. J. The Journal of Physical Chemistry Letters 2011, 2, 1808-1813.

(8) Wang, L.; Ashford, D. L.; Thompson, D. M.; Meyer, T. J.; Papanikolas, J. M. J. Phys. Chem. C. ASAP.

(9) Hanson, K.; Torelli, D. A.; Vannucci, A. K.; Brennaman, M. K.; Luo, H.; Alibabaei, L.; Song, W.; Ashford, D. L.; Norris, M. R.; Glasson, C. R. K.; Concepcion, J. J.; Meyer, T. J. Angew. Chem. Int. Ed. 2012, 51, 12782-12785.

(10) Lee, H.; Kepley, L. J.; Hong, H. G.; Akhter, S.; Mallouk, T. E. J. Phys. Chem. 1988, 92, 2597-2601.

(11) Lee, H.; Kepley, L. J.; Hong, H. G.; Mallouk, T. E. J. Am. Chem. Soc. 1988, 110, 618-620.

(12) Ishida, T.; Terada, K.; Hasegawa, K.; Kuwahata, H.; Kusama, K.; Sato, R.; Nakano, M.; Naitoh, Y.; Haga, M. Appl. Surf. Sci. 2009, 255, 8824-8830.

(13) Terada, K.; Kobayashi, K.; Hikita, J.; Haga, M. Chem. Lett. 2009, 38, 416-417.

(14) Concepcion, J. J.; Jurss, J. W.; Brennaman, M. K.; Hoertz, P. G.; Patrocinio, A. O. v. T.; Murakami Iha, N. Y.; Templeton, J. L.; Meyer, T. J. Acc. Chem. Res. 2009, 42, 1954-1965.

(15) Concepcion, J. J.; Jurss, J. W.; Templeton, J. L.; Meyer, T. J. J. Am. Chem. Soc. 2008, 130, 16462-16463.

(16) Concepcion, J. J.; Tsai, M.-K.; Muckerman, J. T.; Meyer, T. J. J. Am. Chem. Soc. 2010, 132, 1545-1557.

(17) Hanson, K.; Brennaman, M. K.; Ito, A.; Luo, H.; Song, W.; Parker, K. A.; Ghosh, R.; Norris, M. R.; Glasson, C. R. K.; Concepcion, J. J.; Lopez, R.; Meyer, T. J. The Journal of Physical Chemistry C 2012, 116, 14837-14847.

(18) Asbury, J. B.; Ellingson, R. J.; Ghosh, H. N.; Ferrere, S.; Nozik, A. J.; Lian, T. The Journal of Physical Chemistry B 1999, 103, 3110-3119.

(19) Benkö, G.; Kallioinen, J.; Korppi-Tommola, J. E. I.; Yartsev, A. P.; Sundström, V. J. Am. Chem. Soc. 2001, 124, 489-493.

(20) Myahkostupov, M.; Piotrowiak, P.; Wang, D.; Galoppini, E. The Journal of Physical Chemistry C 2007, 111, 2827-2829.

(21) Benkö, G.; Kallioinen, J.; Myllyperkiö, P.; Trif, F.; Korppi-Tommola, J. E. I.; Yartsev, A. P.; Sundström, V. The Journal of Physical Chemistry B 2004, 108, 2862-2867.

(22) Liu, F.; Meyer, G. J. Inorg. Chem. 2005, 44, 9305-9313.

(23) Schoonover, J. R.; Dattelbaum, D. M.; Malko, A.; Klimov, V. I.; Meyer, T. J.; Styers-Barnett, D. J.; Gannon, E. Z.; Granger, J. C.; Aldridge, W. S.; Papanikolas, J. M. J. Phys. Chem. A 2005, 109, 2472-2475.

(24) Medlycott, E. A.; Hanan, G. S. Chem. Soc. Rev. 2005, 34, 133-142.